NTNU

Norwegian University of
Science and Technology

Numerical Modelling to Evaluate the Impact of Paleo-Bathymetry and Basin-Fill Processes on Source Rock Distribution in the Hammerfest Basin, Barents Sea

Anindito Satrio Baskoro

Petroleum Geosciences
Submission date: June 2017
Supervisor: Stephen John Lippard, IGP
Co-supervisor: Benjamin Udo Emmel, SINTEF Petroleum Research
Gerben de Jager, SINTEF Petroleum Research
Ane Elisabet Lothe, SINTEF Petroleum Research

Norwegian University of Science and Technology
Department of Geoscience and Petroleum

Preface

This master thesis report is submitted for the course TGB4915-Petroleum Geoscience Master Thesis as part of my study in international master degree program of Petroleum Geosciences with specialization of Petroleum Geology during Spring semester of 2017 at the Department of Geoscience and Petroleum, Norwegian University of Science and Technology (NTNU). The aim of this master thesis study is numerical modelling to evaluate the impact of paleo-bathymetry and basin-fill processes on source rock distribution in the Hammerfest Basin, Barents Sea.

.

Trondheim, 11 June 2017

_____

Anindito Satrio Baskoro

Acknowledgement

I would like to thank the Department of Geoscience and Petroleum, NTNU for not only giving me the opportunity to pursue my master degree study here but also gave me valuable teaching assistant experiences. Furthermore, I would like to express my gratitude to my thesis supervisor Professor Stephen John Lippard of the Department of Geoscience and Petroleum at NTNU for the useful comments, remarks, and engagement through the learning process during the study and master thesis writing.

I am also thankful to SINTEF Petroleum Research as this master thesis was accomplished from January to June 2017 there. Thousand gratitude are expressed to my supervisor Benjamin Udo Emmel of the Basin Modelling Research Group at SINTEF Petroleum Research. He consistently allowed this study to be my own work but guided me in the right direction whenever I needed it with his like the rock of Gibraltar supervision and constant discussions. Thousand gratitude are also expressed to my supervisor Gerben de Jager of the Basin Modelling Research Group at SINTEF Petroleum Research. The door to Gerben office was always open whenever I wanted to have a discussion about the modelling or thesis writing. I am also grateful to the leader of the Basin Modelling Research Group at SINTEF Petroleum Research, Ane Elisabet Lothe, for giving me precious chance to work on my master thesis there. Also, thanks to the Department of Exploration and Reservoir Technology, especially the Basin Modelling research group for the enjoyable working environment. I would also acknowledge Statoil for the research dataset given for this master thesis modelling.

Special acknowledgment to Indonesia Endowment Fund for Education (LPDP) for granting me full-scholarship during my master study in NTNU, Norway.

Finally, I would like to express my very profound gratefulness to my parents, my fiancée, my friends, and the Indonesian Student Association in Trondheim for providing me with unfailing supports and encouragement throughout my years of study.

Anindito Satrio Baskoro

Abstract

In basin and petroleum system modelling, the paleo-bathymetry and distribution of organic matter within the source rock are important properties yet they are uncertain and are often be considered as constant or homogeneous. In this study, high resolution 3D models are produced with their heterogeneities of paleo-bathymetries, basin-fill processes and source rock distributions, employing numerical modelling for the three most important source rock intervals; the Early-Mid Triassic, the Late Jurassic, and the Early Cretaceous, in the Hammerfest Basin. More importantly, the study attempts to further analyse the factors controlling the source rock distribution by linking the paleo-bathymetry and basin-fill processes. The models are validated by sand fraction (SF), total organic carbon (TOC) and hydrogen index (HI) data. The three source rock intervals show distribution models with diverse values for each parameter. The paleo-water depths vary from 2200 m to 50 m, while the sedimentation rates are between 1 and 48 cm/ka with siliciclastic dominated deposition, and thus reflect different basin-fill processes and tectonic development through time. As a result, the source rocks are composed by various organic matter source types, from marine organic matter to terrigenous and residual organic matter. The source rocks have a range of quantity (TOC from 0.1 to 14 wt%) and quality (HI from 24 to 344 mgHC/gTOC) with poor to very good source rock potential. In general, the Late Jurassic Interval is the best source rock in the study area with good to very good source rock potential. The main reason identified is very high primary productivity with favourable basin-fill process and depositional environment for source bed deposition. With these selected examples, it is demonstrated how the paleo-bathymetry and basin-fill processes control the distribution of the source rock properties. To summarize, the interaction between paleo-bathymetry and basin-fill processes affects the distribution of the source rock especially in terms of organic matter quantity and their dispersal as well as preservation condition.

Contents

List of figures

List of tables

Abbreviations

(1/2/3)D	(one/two/three) dimensional
ca.	circa (around)
CF	carbon flux
C_{res}	residual organic carbon
C_{terr}	terrigeneous organic carbon
DBD	dry bulk density
e.g.	exempli gratia (for example)
Fm(s)	Formation(s)
GR	Gamma-ray (log)
HB	Hammerfest Basin
HI	hydrogen index
ka	thousand years (ago)
Ma	million years ago
MOM	marine organic matter
N-S-E-W	north-south-east-west
NPD	Norwegian Petroleum Directorate
OF-Mod	Organic Facies Modelling (SINTEF's in-house software)
OI	oxygen index
PP	primary productivity
PWD	paleo-water depth
RLFC	Ringvassøy-Loppa Fault Complex
SF	sand fraction
SR	sedimentation rate
TOC	total organic carbon
UTM	Universal Transverse Mercator (coordinate system)
V_{sh}	shale volume

Chapter 1
Introduction

The sedimentary character of basins reflects the dynamic balance between the long-term accommodation space and sediment input (Allen and Allen, 2013; Catuneanu, 2006; Gawthorpe et al., 2000; Schlager, 1993; Steel, 1998). However, the present-day stratigraphic thickness of the basin-fill does not represent the original thickness of paleo-deposition, instead the thickness has been reduced by the progressive effects of compaction and erosion over time (Allen and Allen, 2013; Reynolds et al., 1991; Sadler, 1981). The present-day stratigraphic column therefore cannot be directly translated as past sediment accumulations.

Accommodation space generation is controlled by tectonic subsidence and uplift, eustasy, and compaction, thereby changing the paleo-bathymetry (Allen and Allen, 2013; Paton et al., 2008; Schlager, 1993). Paleo-bathymetry is the paleo-water depth (at the time of deposition), which determines the position of sea bottom relative to a datum (Immenhauser, 2009); whereas, sediment supply depends on the erosion rate and size of the source area (Steel, 1998; Walling, 1983). Volume balance variation between these parameters results in a characteristic basin-fill pattern (Allen and Allen, 2013; Catuneanu, 2006; Helland-Hansen et al., 2016; Steel, 1998).

Paleo-water depth (PWD) reconstruction is an important process in order to understand the routing of sediments in a basin (Emmel et al., 2015). The bathymetry of a basin controls the sediment dynamics and the deposition of sediments in various water-depths (Immenhauser, 2009). Therefore, reconstructed paleo-bathymetries for certain time slices are important to simulate the sediment deposition in a basin, including source rocks. Source rocks, which are the fundamental of a petroleum system, are sediments rich in organic matter derived from photosynthesizing marine or lacustrine algae and land plants that contain chemical compounds known as lipids, preserved in sediments under favourable preservation conditions and source bed depositional settings (Espitalie et al., 1977; Klemme and Ulmishek, 1991; Passey et al., 2010).

In basin and petroleum system modelling, the PWD and distribution of organic matter within the source rock are important parameters in determining the initial condition of a basin-scale petroleum system. However, the paleo-water depth and the distribution of organic matter within the source rock, both in terms of quantity (total organic carbon (TOC)) and quality (hydrogen index (HI)), are uncertain and which are often wrongly considered as constant or homogeneous in basin and petroleum system modelling (de Jager et al., 2016; Kjennerud and

Sylta, 2001). Prediction of source rocks requires an understanding of the structural and stratigraphic evolution of the basin-fill (Klemme and Ulmishek, 1991; Ulmishek and Klemme, 1983), obtained through basin analysis. Identification and interpretation of the controls of the basin formation, including tectonic and thermal processes, and the geometry and sedimentary facies contained in the basin-fill are necessary in order to predict the source rock distribution. This is the most important step towards building geological models as the basis of petroleum play assessment (Allen and Allen, 2013). Therefore, basin analysis is a critical technique to assess undiscovered petroleum potential in the exploration stage. An understanding of the distribution and development of basin-fill and facies allows verified and realistic source rock prediction as the basis of a petroleum system analysis to better rank a relatively immature exploration basin (Allen and Allen, 2013).

By linking the paleo-bathymetry and the basin-fill processes using a basin analysis approach, source rock distribution in a basin can be further analyzed to see how these two main parameters affect the heterogeneity of the source rock quantity and quality both in lateral and vertical trends. Additionally, this may also support the understanding of tectonic development and evolution through geological periods in a basin. Furthermore, the reconstructed paleo-bathymetry and source rock distribution models can be a better input for the advancement of basin and petroleum system modelling in the hydrocarbon exploration stage.

The study area is located in the southwestern Barents Sea (UTM Easting: 255000-320000; UTM Northing: 7915000-7965000) and consists of part of the western Hammerfest Basin (HB) and part of the eastern Ringvassøy-Loppa Fault Complex (RLFC) (**Figure 1**). The Early-Mid Triassic, the Late Jurassic, and the Early Cretaceous Intervals are the primary targets of the study as these are three important source rock intervals in the HB and the Barents Sea generally (Ohm et al., 2008a; Rodrigues Duran et al., 2013a; Rodrigues Duran et al., 2013b; Ronnevik et al., 1982). These three source rocks are deposited in different tectonic development stages in the Barents Sea and as such interesting for further study. The study area has been actively explored, therefore it is a suitable area to validate modelling results with the available well-data (**Table 2**) and published models from various literature (e.g. Brekke et al., 2001; Georgiev et al., 2017; Glørstad-Clark et al., 2010). Additionally, the HB has undergone several rifting stages as a part of the intracratonic Barents Sea (Faleide et al., 2008; Gudlaugsson et al., 1998; Larsen et al., 1993; Roberts, 2003; Roberts and Gee, 1985) which makes it suitable to evaluate the impact of different rift-drift stages on the source rock distribution. However, the Early-Mid Triassic Interval is lacking in well-data as most of the drilled wells do not penetrate this

formation (**Table 2**). One of the challenges during the study is to model the source rock distribution with limited well-control, similar to one of the main tasks of a petroleum geologist in an early exploration stage.

Chapter 2
Geological setting of the study area

2.1 Regional geology of the Barents Sea

Physiographically, the Norwegian continental margin consists of a continental shelf and slope with marked variations in width and steepness. One of the adjacent shallow seas, the Barents Sea, is part of large epicontinental sea located between the continental masses of Fennoscandia, Svalbard and Russia (Novaya Zemlya) (Faleide et al., 2008). The large epicontinental basin of the Barents Sea area is bounded to the west and north by the Norwegian-Greenland Sea and Arctic Ocean, which are young passive continental margins (**Figure 1a**). The Barents Sea has an intracratonic setting and has been affected by several tectonic phases since the Caledonian orogenic movements from the Ordovician to the Early Devonian (Faleide et al., 2008; Gudlaugsson et al., 1998; Larsen et al., 1993; Roberts, 2003; Roberts and Gee, 1985). The Barents Sea continental shelf is dominated by ENE-WSW to NE-SW and NNE-SSW to NNW-SSE structural trends with local influence of WNW-ESE striking structures (Gabrielsen, 1990). The tectonic activity has produced the geology of the Barents Sea, from collisional orogeny, to progressive rifting, and finally to continental breakup along a transform margin (Clark et al., 2013; Faleide et al., 2008; Faleide et al., 1993; Gudlaugsson et al., 1998).

In the western Barents Sea, Late Paleozoic rift basins formed between Norway and Greenland following the NE-SW striking Caledonian structural trend (Faleide et al., 2008; Gabrielsen et al., 1990). The first Late Paleozoic-Early Mesozoic rifting episode can be subdivided into the mid-Carboniferous, Carboniferous-Permian and Permian-Early Triassic rift phases (Doré, 1991; Faleide et al., 2008) (**Figure 1a**). During Mid Carboniferous rifting started in the Barents Sea basins, followed by Late Carboniferous-Early Permian renewed block faulting especially in the Loppa High and Stappen High areas (Brekke and Riis, 1987; Gabrielsen et al., 1990) and regional subsidence with deposition of clastic sediments (**Figure 2**). Afterwards the sedimentary regime changed and mainly carbonates and evaporates were deposited on a stable continental shelf until Mid Permian (Faleide et al., 2008). In general, the Permian was marked by regional extent of carbonate platform with deposition of dolostones and limestones (**Figure 2**) (Ohm et al., 2008b) and renewed block faulting (Gabrielsen et al., 1990) .

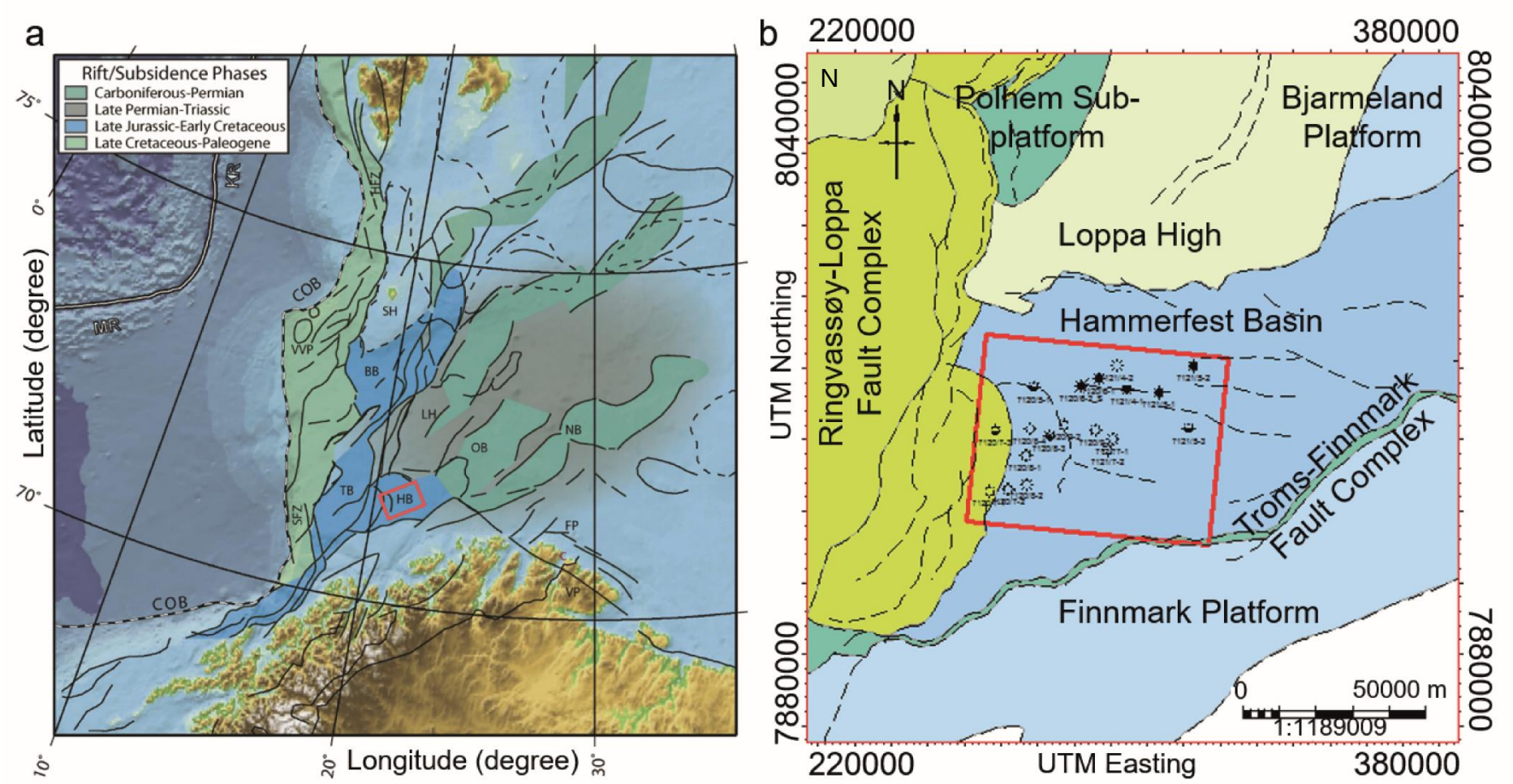

Figure 1. Structural map showing main structural elements in different scale. (a) The western Barents Sea (modified after Clark et al., 2013). (b) The Hammerfest Basin. Red square depicts the study area. BB: Bjørnova Basin, COB: continent-ocean boundary, FP: Finnmark Platform, HB: Hammerfest Basin, HFZ: Hornsund Fault Zone, KR: Knipovich Ridge, LH: Loppa High, MR: Møre Basin, NB: Nordkapp Basin, OB: Ottar Basin, SFZ: Senja Fracture Zone, SH: Stappen High, TB: Tromsø Basin, VP: Varanger Peninsula, VVP: Vestbakken Volcanic Province.

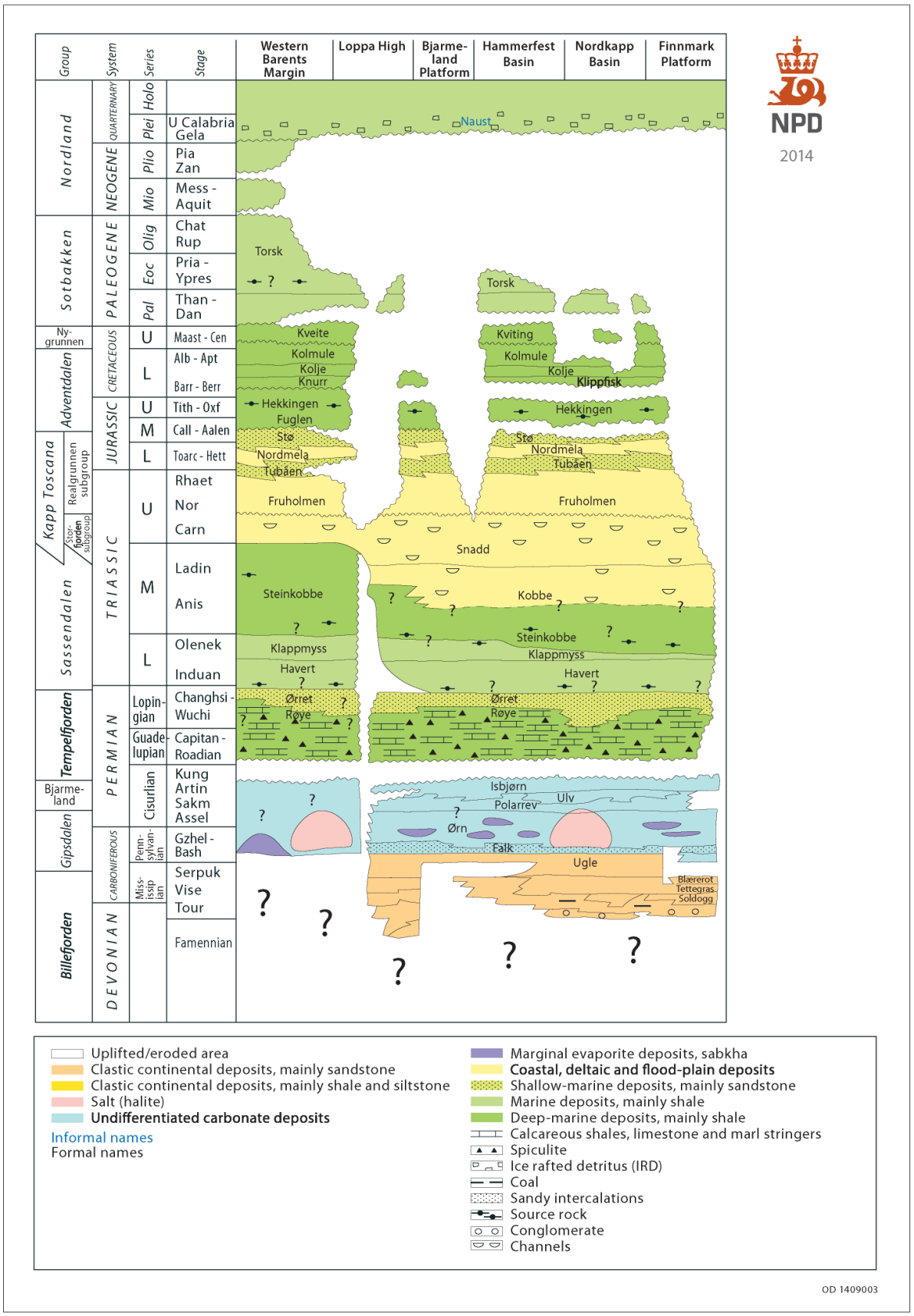

Figure 2. Lithostratigraphy chart of the Barents Sea (from Norwegian Petroleum Directorate (NPD)).

Rifting and fault activity during Permian-Early Triassic are recorded in the onshore East-Greenland with mid-Permian normal faulting and Early Triassic block-faulting (Faleide et al., 2008; Surlyk, 1990). In the Barents Sea, regional subsidence (Faleide et al., 2008) and deposition of transgressive-regressive thick marine-alluvial shales and sandstones (**Figure 2**) (Ohm et al., 2008b) represented the Triassic evolution (Faleide et al., 2008). Anell et al. (2013) observed deep-rooted faults and syn-sedimentary fault growth with sediment thickness variations that terminated within the Triassic sequence. This extensional faulting may possibly be driven by far-field stresses linked to the Uralide orogeny. However, this observation contradicts the general assumption of tectonic quiescence (Gabrielsen et al., 1990; Glørstad-Clark et al., 2011; Høy and Lundschien, 2011; Riis et al., 2008; Worsley, 2008) and inferred extensional events with no typical rift-related faulting during the Triassic (Doré, 1991; Johansen et al., 1994; Johansen et al., 1992; O'leary et al., 2004; Wood et al., 1989; Ziegler, 1988). The Stappen and Loppa highs experienced tilting while eastern areas encountered subsidence during Early Triassic (Gabrielsen et al., 1990). From the Ladinian to Callovian, the Loppa High was a part of regional basin together with the Hammerfest Basin and Bjarmeland Platform (**Figure 1a**) (Gabrielsen et al., 1990). During the Triassic the depositional environment was shallow marine with gradual infill of prograding sediments sourced from the east and the southeast (Anell et al., 2013; Gabrielsen et al., 1990; Glørstad-Clark et al., 2010; Høy and Lundschien, 2011). Sediment packages associated with Late-Permian - Triassic rifting periods are poorly preserved as they are overprinted by younger tectonic events and buried under thick younger stratigraphic units (Faleide et al., 2008; Gudlaugsson et al., 1998). Shallow marine deposition dominated by sandstones (coarser siliciclastics) took place throughout Early-Mid Jurassic (**Figure 2**) (Faleide et al., 2008; Ohm et al., 2008b).

During Mid Jurassic to Early Cretaceous, the extensional stress field vector shifted to NW-SE caused by the propagating NE Atlantic-Arctic rifting (Faleide et al., 2008; Faleide et al., 1993). This period marks the second major phase of block-faulting along NE-SW trending and west-dipping trend of normal faults (Clark et al., 2013) and marine half-graben infill (Ohm et al., 2008b) associated with active rifting (Faleide et al., 2008; Faleide et al., 1993). The present-day major basins and highs in the western Barents Sea formed during this episode (Gabrielsen et al., 1990). Furthermore, this led to the eventual development of narrow and deep Cretaceous basins in the SW Barents Sea, including the Bjørnøya and Tromsø Basin (**Figure 1a**) with a characteristic of rapid subsidence and segmentation into sub-basins and highs (Faleide et al., 2008).

During the Early Cretaceous, the Tromsø Basin and the western part of Bjørnøya Basin subsided rapidly and locally inversion of the faults along the Ringvassoy-Loppa Fault Complex and at its junction with the Asterias Fault Complex (Gabrielsen et al., 1990). The Aptian-Albian is characterized by eustatic sea-level rise and regional tectonism, increasing the sediment accommodation space in the western Barents Sea (Faleide et al., 2008; Gradstein et al., 1999). Regional uplift in the North Atlantic realm provided southward sediment progradation in the Barents Sea (Faleide et al., 2008). Towards the Late Cretaceous, reverse faulting, folding and extensional faulting occured in some areas in the Barents Sea (Gabrielsen et al., 1990).

The final tectonic phase began in the Late Cretaceous preceding the transform breakup during Early Eocene with the onset of seafloor spreading in the North Atlantic to the south and the Arctic to the north (Clark et al., 2013; Faleide et al., 2008; Faleide et al., 1993; Hallam, 1971; Sclater and Christie, 1980; Ziegler, 1988). The breakup related tectonism and magmatism happened at the onset of this rifting as the crust between NW Europe and Greenland had been extensively weakened by previous rift episodes (Faleide et al., 2008).

During the Cenozoic three main episodes of uplift and erosion occured in the Barents Sea, specifically during Paleocene, Oligocene-Miocene, and Pliocene-Pleistocene (Clark et al., 2013; Dimakis et al., 1998; Faleide et al., 1996; Gabrielsen et al., 1990; Hjelstuen et al., 2007; Ohm et al., 2008b; Rise et al., 2005; Vorren et al., 1991).

In general, some significant tectonic differences are seen between the western and eastern parts of the western Barents Sea, bordered by the N-S to NNE-SSW trending major structural elements the Ringvassøy-Loppa and Bjørnøyrenna Fault Complexes. The western area was tectonically active during Late Mesozoic-Cenozoic with deposition of thick Cretaceous, Paleogene and Neogene sediments. In contrast, the southeastern part of the western Barents Sea is dominated by thick Upper Paleozoic and Mesozoic sediments (Halland et al., 2013b).

2.2 Evolution of the Hammerfest Basin

The Hammerfest Basin (HB) (**Figure 1**) is controlled by dominant E-W to ENE-WSW trending faults, bounded by the Ringvassøy-Loppa Fault Complex to the west (Tromsø Basin), the Troms-Finnmark Fault Complex to the south (Finnmark Platform), the Asterias Fault Complex to the north (Loppa High) and the Bjarmeland Platform to the northeast (Gabrielsen et al., 1990). High angle faults separate the basin margins whereas listric normal faults occur above the Permian sequence in the central part of the basin.

The HB is classified as a "failed" rift in a triple junction and as a remnant of an older rift system overlain by a younger one. Gabrielsen et al. (1990) suggested that the formation of the

HB relates to transfer-faulting and rotation of regional fault blocks. The basin is characterised by an E-W striking fault bounded central dome running parallel to the basin axis (**Figure 1**). This structure mainly formed during the Mid Jurassic (Gabrielsen, 1984; Gabrielsen et al., 1990) and it was reactivated during the Late Jurassic to Early Cretaceous (Berglund et al., 1986; Gabrielsen and Faerseth, 1989; Sund et al., 1986). The structures in the western part of the HB generally dip to the west towards the Tromsø Basin (**Figure 1**).

Late Paleozoic to Early Mesozoic rifting

Rifting in the HB was probably initiated during Early-Mid Carboniferous (Halland et al., 2013b) as indicated by the Late Carboniferous to Early Permian age of the oldest sediment sequence composed of rift-fill alluvial fan and floodplain clastic sediments mixed with carbonates and evaporites (**Figure 2**) (Rodrigues Duran et al., 2013a). Basin subsidence continued until the Late Permian, followed by cyclic infill of shales and sandstones (Ørret Fm) over the carbonate platform (**Figure 2**). Subsequently during the Early-Mid Triassic times, the three progradational units (Havert, Klapmyss, and Kobbe Fms) were deposited (**Figure 2**). Local development of anoxia favored source rock deposition (Rodrigues Duran et al., 2013a). The Late Triassic was characterized by regional subsidence and the deposition of potential source rocks of the Snadd, and Fruholmen Fms (**Figure 2**). The younger sediment sequences of the Tubåen, Nordmela and Stø Fms were deposited as deltaic sediments during the Early and Mid Jurassic (**Figure 2**) (Rodrigues Duran et al., 2013a).

Mesozoic transgression and regression

A Mid to Late Jurassic global sea-level rise caused the deposition of marine shales of the Fuglen Fm and the organic-rich shales of the Hekkingen Fm (**Figure 2**). During the Late Jurassic to Early Cretaceous the renewed rifting formed the main structure defining the basin (Faleide et al., 2008; Faleide et al., 1993). Since then, uplift, flexuring and faulting has dominated the structural development of the HB (Berglund et al., 1986). During the Early Cretaceous, the marine shales of the Knurr and Kolje Fms were deposited, followed by a renewed transgression and deposition of the Kolmule Fm (Rodrigues Duran et al., 2013a) (**Figure 2**). The Late Cretaceous was marked by the development of a condensed sequence of the Kveite Fm as a result of marine transgression (**Figure 2**) (Nøttvedt et al., 1993).

Cenozoic uplift and erosion

At ca. 55-54 Ma the North Atlantic-Arctic rifting started with a final break-up at the Paleocene-Eocene transition (Faleide et al., 2008). During this time the Torsk Fm covered a

wide part of the basin followed by Mid-Oligocene passive margin development in the western Barents Shelf (**Figure 2**). Meanwhile, tectonic uplift caused deep erosion of the eastern part (Berglund et al., 1986; Rodrigues Duran et al., 2013a).

The Northern Hemisphere Glaciation started at ca. 2.6 Ma and caused some erosions in the HB (Faleide et al., 1996; Faleide et al., 2008; Laberg and Vorren, 1996; Rise et al., 2005; Rodrigues Duran et al., 2013a; Vorren et al., 1991). The Erosion and loading effects due to large ice-caps, followed by unloading and uplift during deglaciation, mark the late stage evolution of the HB and the Barents Sea (Reemst et al., 1994; Rodrigues Duran et al., 2013a).

2.3 Source rock intervals in the Hammerfest Basin

Multiple potential source rocks has been encountered in the Barents Sea, resulting in mixtures of charged petroleum in the reservoirs. Cenozoic exhumation is believed to be one of the trigger factors to this hydrocarbon mixture (Lerch et al., 2016). Some oil accumulations in the HB contain a mixture of hydrocarbons. Mixture of hydrocarbon was derived mainly from the Jurassic, Triassic, and Paleozoic source rocks (**Figure 2**) (Murillo et al., 2016).

2.3.1 Early-Mid Triassic

The Early-Mid Triassic organic-rich source rocks have good hydrocarbon generation potential (Gac et al., 2014; Lerch et al., 2016) deposited under anoxic condition due to ancient paleo-Loppa High and limited circulation of the basin (Bugge and Fanavoll, 1995; Leith et al., 1992; Mørk and Elvebakk, 1999; Van Veen et al., 1993). In this interval, the Havert Fm, Klappmyss Fm, Steinkobbe Fm and Kobbe Fm were deposited in the HB (**Figure 2**). A marine environment with the coastline to the south and southeast of the HB and progressive onlap of the submerged Loppa High to the north was encountered in the lower parts. The upper parts reveal northwestward outbuilding of deltaic sequences in an extensive, low relief depositional basin (Glørstad-Clark et al., 2010; Hadler-Jacobsen et al., 2005; Halland et al., 2013b; Jacobsen and van Veen, 1984; Johansen et al., 1992; Riis et al., 2008; Skjold et al., 1998; Van Veen et al., 1993).

The Havert Fm (Induan) (**Figure 2**) in the HB consists of monotonous silty shale sequence with very weak coarsening upward trend, fining from the southern margins of the HB toward the north (Dalland et al., 1988) and thinning from north to south and east to west (Glørstad-Clark et al., 2010). The lower part represents sediment being sourced from the south (the Fennoscandian Shield), marking initial progradation, from south to north and from east to west, in the HB (Berglund et al., 1986; Bullimore et al., 2004; Glørstad-Clark et al., 2011; Glørstad-

Clark et al., 2010; Hadler-Jacobsen et al., 2005; Skjold et al., 1998; Van Veen et al., 1993). The deposition took place in a marginal to open marine setting with coastal environment to the south and southeast (Dalland et al., 1988; Glørstad-Clark et al., 2010).

The Klappmyss Fm (Olenekian) (**Figure 2**) contains medium to dark grey shale passing upwards into siltstones and sandstones, thickening and fining northwards from the southern margins of the HB (Dalland et al., 1988; Glørstad-Clark et al., 2011; Glørstad-Clark et al., 2010). The sediments were mainly sourced from the south and southeast of the HB (Berglund et al., 1986; Bullimore et al., 2004; Dalland et al., 1988; Glørstad-Clark et al., 2011; Glørstad-Clark et al., 2010; Hadler-Jacobsen et al., 2005; Skjold et al., 1998; Van Veen et al., 1993). The depositional environment in the Olenekian was marginal to open marine with renewed north-northwestward/basinward coastal progradation (Dalland et al., 1988; Glørstad-Clark et al., 2010; Riis et al., 2008).

The Steinkobbe Fm (Anisian) (**Figure 2**) consists of phosphatic, organic-rich mudstone (TOC 1.5-9%) and siltstone beds (Dallmann, 1999). The Steinkobbe Fm is equivalent of the Botneheia Fm in the Svalbard which represents deep, mostly restricted, open shelf environment (Bugge and Fanavoll, 1995; Dallmann, 1999; Mørk and Elvebakk, 1999).

The Kobbe Fm (Anisian-Early Ladinian) (**Figure 2**) consists of thick shale unit passes up into interbedded shale, siltstone and carbonate cemented sandstone with coarser proximal facies along the southern margin of the HB, fining toward the basin axis. The thicknesses of the Kobbe Fm is more varying from platform to basin axis than in the underlying units (Dalland et al., 1988). It is thinning from south to north and onlapping onto eastern part of the paleo-Loppa High in the HB. The main source of sediment deposits were southeast and south of the Basin with sediment transport further westward and northwestward into the basin (Berglund et al., 1986; Bullimore et al., 2004; Dalland et al., 1988; Glørstad-Clark et al., 2011; Glørstad-Clark et al., 2010; Hadler-Jacobsen et al., 2005; Riis et al., 2008; Skjold et al., 1998; Van Veen et al., 1993). During the deposition, sediment supply was higher than the rise of sea-level. Uplift of the paleo-Loppa High occurred during deposition and acted as local sediment source area (Glørstad-Clark et al., 2010). The Kobbe Fm was deposited in the transgressive pulse followed by renewed build-out of clastic marginal marine regimes from southern coastal areas (Dalland et al., 1988; Glørstad-Clark et al., 2010; Riis et al., 2008) and in the period of maximum basinward progradation of the system (Glørstad-Clark et al., 2010; Riis et al., 2008).

2.3.2 Late Jurassic

The Late Jurassic Interval (the Hekkingen Fm) is considered as an important oil prone source rock as well as a cap rock in the HB (**Figure 2**). The lithology of the Hekkingen Fm is shale and mudstone with rare thin interbeds of limestone, dolomite, siltstone and sandstone, deposited in a deep marine shelf/basin with anoxic conditions as a results of restricted water circulation formed by tectonic barriers during subsidence (Dalland et al., 1988; Georgiev et al., 2017). The sandy deposits of the Hekkingen Fm are constrained in the southern and northern margin of the HB (Dalland et al., 1988). The Hekkingen Fm is subdivided into lower Alge Member and upper Krill Member (Dalland et al., 1988; Faleide et al., 2008; Georgiev et al., 2017).

The Alge Member (Late Oxfordian-Kimmeridgian) is characterized by its high gamma intensity in the lower part of Hekkingen Fm which consists of black paper shales rich in organic material (high TOC), deposited in restricted shelf environments (Dalland et al., 1988; Dallmann, 1999; Georgiev et al., 2017).

The Krill Member (Kimmeridgian-Volgian) is brownish-grey to very dark grey shale and claystone with rare thin interbeds of limestone, dolomite, siltstone and sandstone, deposited in open to restricted shelf environments (Dalland et al., 1988). It is characterized by lower TOC contents and lower gamma-ray readings compared to the underlying units (Dalland et al., 1988; Georgiev et al., 2017).

2.3.3 Early Cretaceous

The Early Cretaceous interval included lower Klippfisk Fm and upper Kolje Fm (**Figure 2**). The Klippfisk Fm (Smelror et al., 1998) (**Figure 2**) is the carbonate platform, equivalent to the Knurr Fm in the HB which consists of limestones and marls, and is often glauconitic. The Klippfisk Fm was deposited in the platform areas (Dallmann, 1999).

The Kolje Fm (**Figure 2**) is dominated by dark brown to dark grey shale and claystone, with minor interbeds of limestone and dolomite and thin interbeds of silstone and sandstone in the upper part. This Kolje Fm is thinning toward the central part of the HB and was deposited in the distal open marine conditions, with good water circulation and periodic restricted environments (Dalland et al., 1988).

Chapter 3
Methods

The bathymetry of a basin controls the sediment exchange dynamics and the deposition of sediments in various water-depths (Ganti et al., 2014). Therefore, reconstructed paleo-bathymetries for certain time slices are important to simulate the source rock deposition in a basin.

This study aims to reconstruct the three most important source rock intervals in the Hammerfest Basin (HB) which are the Early Cretaceous Interval (the Kolje and Klippfisk Fms), the Late Jurassic Interval (the Hekkingen Fm), and the Early-Mid Triassic Interval (the Havert-Klappmyss, Steinkobbe and Kobbe Fms). Paleo-water depth (PWD) reconstruction was performed using SINTEF's Matlab PWD-toolbox while source rock distribution was modelled with SINTEF's in-house software OF-Mod.

The general workflow is summarized in four steps (**Table 1**). (1) 3D PWD maps for each layer. Paleo-bathymetry reconstruction, a numerical simulation to calculate the fill formations of the basin and do decompaction and backstripping was used. (2) Validation using the grain size variation and calculation of the misfit are performed to get the best-fit model of water-depth changes for the target formations. These are then used to correct the PWD map using Petrel. These results, together with other input data, are then utilized to model both (3) inorganic and (4) organic facies to produce sand fraction (SF) and source rock distribution models in OF-Mod (1D and 3D).

Table 1. General workflow of the study with the involved software for each process.

	Process	Software
(1)	PWD reconstruction (backstripping)	SINTEF's Matlab PWD-toolbox
(2)	Water-depth change and PWD map reconstruction	SINTEF's Matlab PWD-toolbox and Petrel 2015
(3)	Inorganic facies and sand fraction distribution modelling	SINTEF's in-house OF-Mod 3D
(4)	Organic facies and source rock distribution modelling	SINTEF's in-house OF-Mod 1D/3D

3.1 Input data

The main input are the surface maps for 12 formation tops in the HB, data from 18 wells, including gamma-ray log, ages, and geochemical data (**Figure 3**). Surface maps for 12 formation tops from Top Permian to Seabed and the well and geochemical data were provided by Statoil. The three other formation tops surface maps were however reconstructed during the study (**Figure 3b**). Top Cisurian and Missisipian Intervals were reconstructed by shifting with thickness amount information in the Norwegian Petroleum Directorate (NPD) from the Top Permian surface map (**Figure 3**). Top basement was reconstructed by digitizing regional-basement structure map in the Barents Sea based on Marello et al. (2013). NPD litho-stratigraphy description, including the litho-stratigraphy chart, helped determining the age for each top formation or interval and general SF which is essentially required in this study (**Figure 3**). General SF data is needed for the main input in the backstripping process during paleo-bathymetry reconstruction before calibration. In this study, not all of the well data contain measured geochemical data **Table 2**. Moreover, there is only one well (7120/9-2) penetrating the Kobbe Fm in the study area. Due to the lack of data in the Kobbe Fm interval, the paleo-bathymetry reconstruction of top Kobbe Fm neglected the best-fit water-depth calibration (**Figure 3**). Instead, both inorganic and organic facies modelling for the Lower-Middle Triassic Interval used the backstripped PWD maps. For some wells, measurement of the geochemical data has poor quality as shown by the less measurement points that may affect the reliability of the modelling and calibration results. Other important data, such as PWD maps for inorganic facies modelling as well as inorganic facies for organic facies modelling, were acquired during the simulation.

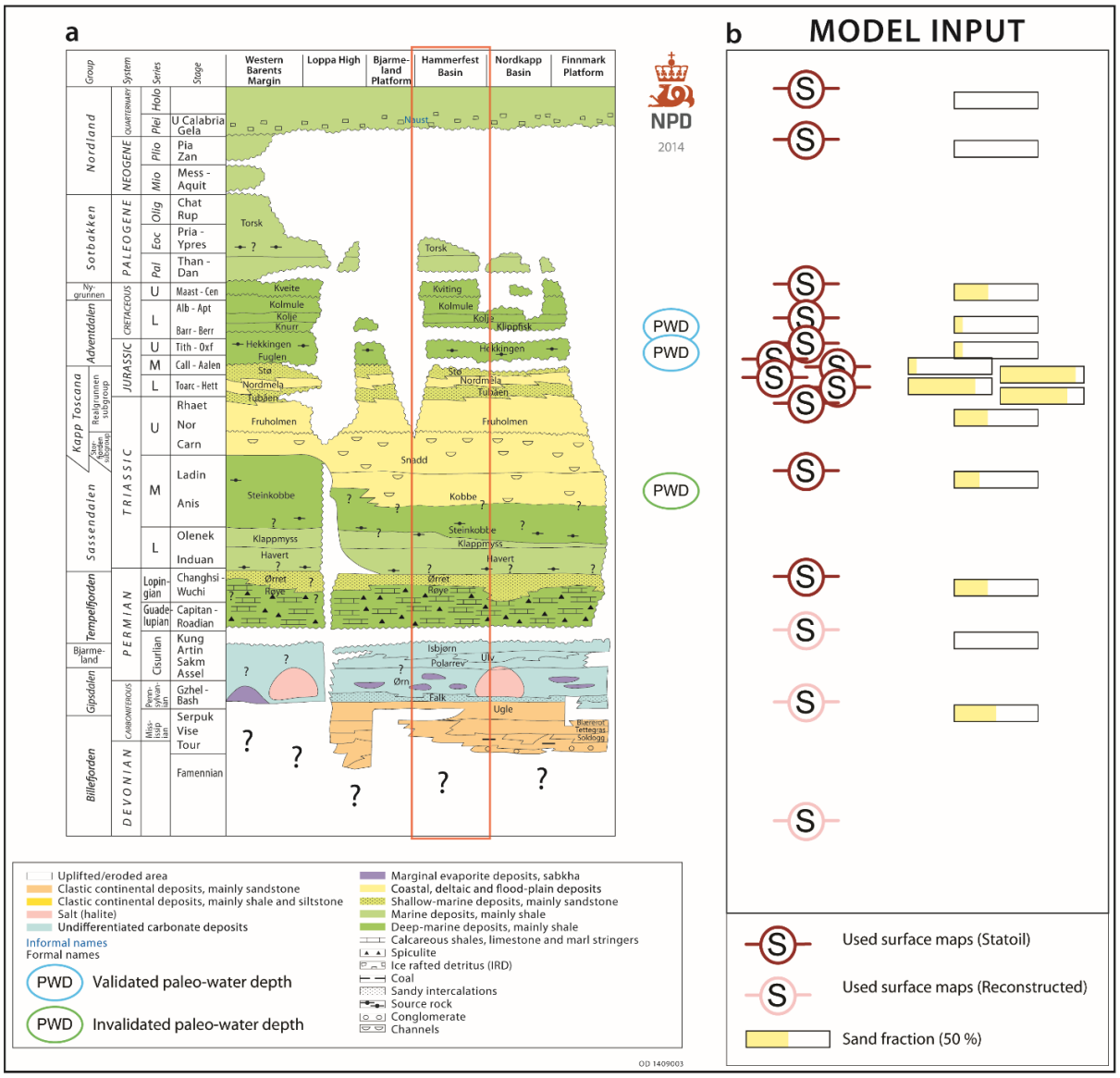

Figure 3. The main input data. (a) Lithostratigraphic chart of Norwegian Barents Sea. Red column depicts the lithostratigraphy of the Hammerfest Basin as one of the main references in determining the age and sand fraction of the intervals. (b) Model input; including Statoil surface maps, reconstructed surface maps (top Lower Permian, top Lower Carboniferous, and top Basement (Marello et al., 2013)), and general sand fraction input for each stratigraphic unit in the study area.

Table 2. Well-data availability in the study area. GR: gamma ray log. Geochemical data consist of total organic carbon (TOC) and hydrogen index (HI). Age data indicate that the formation tops are present in the well. V: data is available; -: data is not available.

wellbore name	Early Cretaceous Interval			Late Jurassic Interval			Early-Mid Triassic Interval		
	GR log	Geochemical data	Age data	GR log	Geochemical data	Age data	GR log	Geochemical data	Age data
7120/5-1	V	V	V	V	V	V	-	-	-
7120/6-1	V	V	V	V	V	V	-	-	-
7120/6-2S	V	-	V	V	-	V	-	-	-
7120/7-1	V	V	V	V	V	V	-	-	-
7120/7-2	V	V	V	V	-	V	-	-	-
7120/7-3	V	V	V	V	V	V	-	-	-
7120/8-1	V	V	V	V	V	V	-	-	-
7120/8-2	V	V	V	V	-	V	-	-	-
7120/8-3	V	-	V	V	-	V	-	-	-
7120/8-4	V	-	V	V	-	V	-	-	-
7120/9-1	V	V	V	-	V	-	-	-	-
7120/9-2	V	V	V	V	V	V	V	V	V
7121/4-1	V	-	V	V	V	V	-	-	-
7121/4-2	V	V	V	V	-	V	-	-	-
7121/5-1	V	V	V	V	V	V	-	-	-
7121/5-2	V	V	V	V	-	V	-	-	-
7121/5-3	V	-	V	-	-	-	-	-	-
7121/7-1	V	V	V	V	V	V	-	-	-

3.2 Methodology

3.2.1 Sand volume calculation

The stratigraphy of the sedimentary basin is the result of the interplay between sediment supply and the generation of accommodation space (Allen and Allen, 2013; Catuneanu, 2006; Gawthorpe et al., 2000; Schlager, 1993; Steel, 1998). Further, the physical rock record of a stratigraphic unit, especially clastic sediments, may provide an alternative method to calibrate the reconstructed accommodation space (paleo-bathymetry) (Immenhauser, 2009) and the basin-fill sediment. In this study, gamma-ray log data is employed to estimate the sand volume in the sediment to help reconstructing the basin-fill stratigraphy as well as the paleo-bathymetry during the deposition.

Gamma-ray (GR) log data measures the natural gamma radiation in the formation, which in turn can be interpreted as the basic lithologic information of the formation. Furthermore, the shale volume (V_{sh}) can be estimated using an empirical equations and factor analysis to determine the SF (Szabó and Dobróka, 2013). Sand fraction is one of the main lithology inputs in this study. Simplified linear shale volume (V_{sh}) estimation (**Eq. (1)**) by using GR reading and cut-off for pure shale and pure sand GR value, GR_{log}, GR_{min}, and GR_{max} respectively, from Schlumberger (1972), was used as a preliminary shalyness indicator to obtain the shalyness index I_{GR}:

$$V_{sh} = I_{GR} = \frac{GR_{\log} - GR_{\min}}{GR_{\max} - GR_{\min}} \tag{1}$$

However, since linear shalyness index estimation often yields an over-estimation of shale volume, an empirical formula from (Clavier et al., 1971) is chosen for correcting the estimated shale volume (**Eq. (2)**) as the function of shaliness index. Even though most of the non-linear empirical formula trend-lines match the factor analysis result from the work of (Szabó and Dobróka, 2013), the empirical formula from (Clavier et al., 1971) suggests neither pessimistic nor optimistic shale volume estimation compared to the other methods (**Figure 4**). In the following **Eq. (2)** the ruling equation to correct the estimated I_{GR} from (Clavier et al., 1971) is introduced in detail:

$$V_{sh} = 1.7 - \sqrt{\left(3.38 - \left(I_{GR} + 0.7\right)^2\right)} \tag{2}$$

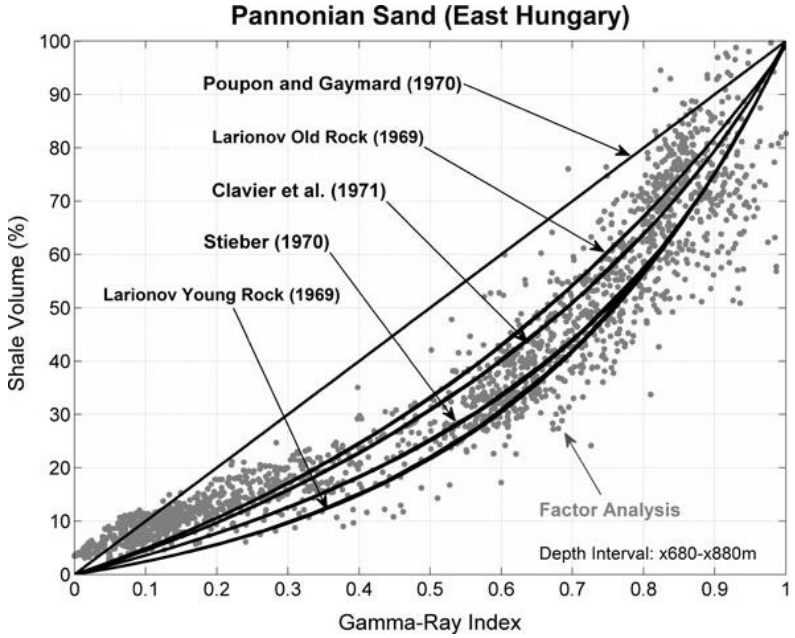

Figure 4. Natural gamma-ray index relationship to shale volume from different empirical formulas (black lines) and factor analysis estimation (grey dots) (Szabó and Dobróka, 2013).

3.2.2 Paleo-bathymetry reconstruction

The fundamental processes needed in order to reconstruct paleo-bathymetry of the present day stratigraphic column are removing the burial effects in present-day stratigraphic unit to get an initial thickness as well as the accommodation space generated after the deposition. Here, the paleo-bathymetry reconstruction is divided into a numerical iteration process and a validation part, where each part produces different results necessary required to make a reconstructed PWD-map (**Figure 5**). Present-day thickness of each formation is determined based on present-day depth, which comes from each top-base of present day surface maps (**Figure 3**). Incorporating the present-day bathymetry with all the main input needed in decompaction and backstripping, a numerical iteration process is executed in a high-resolution simulation.

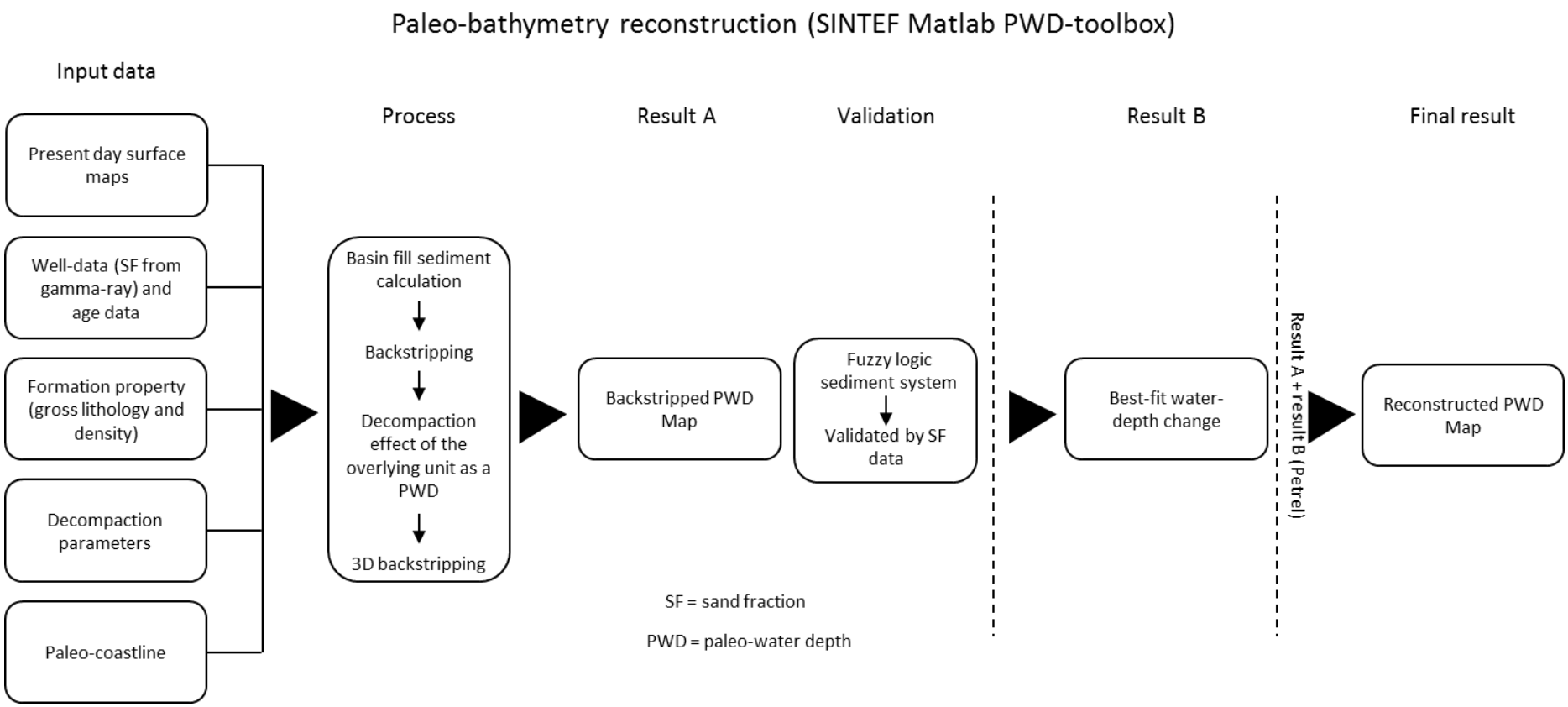

Figure 5. The general workflow of paleo-bathymetry reconstruction using SINTEF Matlab PWD-toolbox and Petrel. In the reconstruction of the PWD map (final result) from the backstripped PWD map (result A), the best-fit water-depth model (result B) can be separated into different compartments according to basin geometry (for example foot-wall and hanging wall areas as they may experience various water-depth change (Allen and Allen, 2013)) and tectonic setting.

Decompaction is a process of removing progressive effects of compaction and layer thickness-average porosities reduction during basin subsidence. Decompaction allows restoration of the thicknesses relating to a certain geologic time in the burial history using porosity-depth relationships for each lithology (Allen and Allen, 2013; Baldwin, 1971; Paul and Barras, 1998). The decompaction process uses exponential porosity-depth relationships proposed by Sclater and Christie (1980) in which calculation (**Eq. (3)**) is based on initial porosity at the surface (ϕ_0) and porosity-depth coefficient (c) with units of km^{-1} to define the porosity at any depth of y ($\phi(y)$):

$$\phi(y) = \phi_0 \exp(-cy) \tag{3}$$

In general, the decompaction iteration process is summarized in 6 steps (**Figure 6**). (a) Present-day (T_0) stratigraphic units (A, B, and C) where C is bounded by the top (y_1) and bottom (y_2). (b) Unit C (lowest) is restored to the initial time of deposition (T_2) as a decompacted unit (C_d) by removing units A and B, neglecting the loading effect. (c) Unit C_d is restored to its initial condition with new top (y'_1) and bottom (y'_2), taking into account the isostatic response from the loading effect by applying Airy isostasy. (d) At time T_1, the unit B is restored as decompacted unit (B_d) above the unit C_d, causing unit C_d to be partially-compacted (C_{dc}) due to loading effect from unit B. (e) The unit A is restored back to the present day, causing all underlying sequences to be compacted (B_c and C_c). (f) Accommodation space (ASP) or PWD is calculated by substracting the thickness of the decompacted unit, i.e. C_d, with the compacted unit, i.e. C_c. During the decompaction, initial porosity (ϕ_0) is exponentially decreasing from the initial deposition to the present-day, estimated from the porosity-depth relationship (**Eq. (3)**) (Sclater and Christie, 1980).

The decompaction process is then repeated using a numerical iteration process of the decompaction equation (**Eq. (4)**):

$$y'_2 - y'_1 = y_2 - y_1 - \frac{\phi_0}{c}\left\{e^{-cy_1} - e^{-cy_2}\right\} + \frac{\phi_0}{c}\left\{e^{-cy'_1} - e^{-cy'_2}\right\} \tag{4}$$

The decompacted depths (S) are then corrected as S^* (**Eq. (5)**) with the incoporation of paleobathymetry, represented by water-depth (W_d), eustasy (sea-level change (Δ_{SL})) and density (mantle (ρ_m) and water (ρ_w)):

$$S^* = S - \Delta_{SL}\left(\frac{\rho_w}{\rho_m - \rho_w}\right) + (W_d - \Delta_{SL}) \tag{5}$$

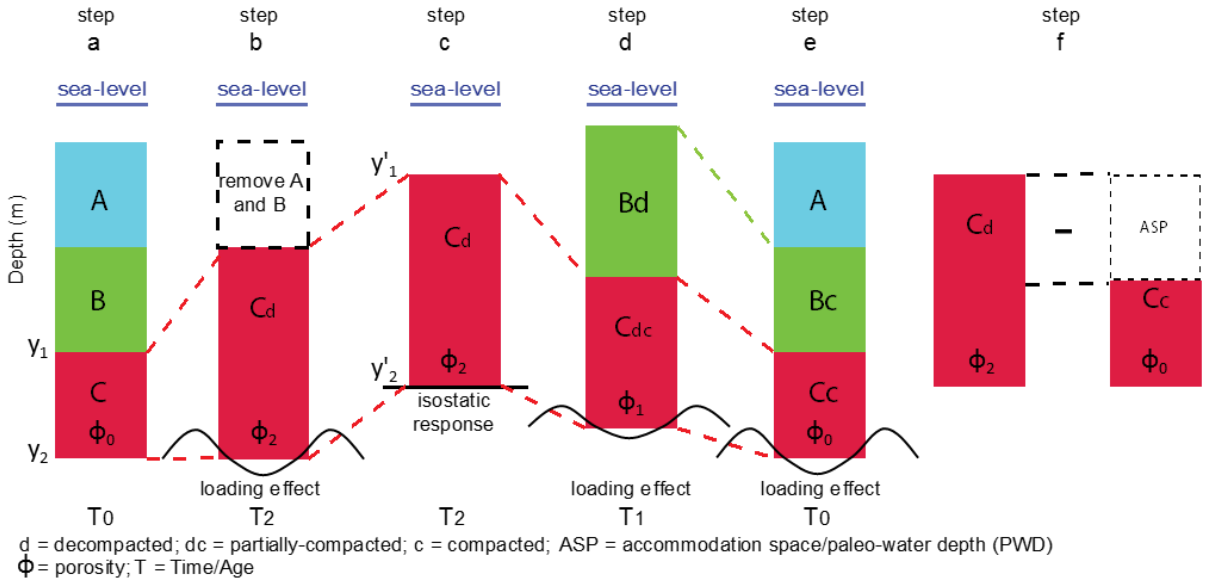

Figure 6. General steps of decompaction iteration process, modified after Emmel et al. (2015). 0,1,2: depositional sequence (0 is younger than 2); T0: present-day and T2: initial deposition. $\phi_0 < \phi_1 < \phi_2$, calculated using porosity-depth relationships from Sclater and Christie (1980).

Backstripping is a process of removing the effect of sediment-loading to reveal the driving force for the tectonic subsidence in the water-filled basin. The sediment-load can be estimated using Airy isostasy. In order to do so, calculation of bulk density of both an individual layer *i* (ρ_b) (**Eq. (6)**) and sediment-column ($\bar{\rho}_b$) (**Eq. (7)**) with grain density (ρ_b) need to be performed first (Allen and Allen, 2013):

$$\rho_b = \phi\rho_w + (1-\phi)\rho_{gi} \tag{6}$$

$$\bar{\rho}_b = \sum_i \left\{ \frac{\bar{\phi}_i \rho_w + (1-\bar{\phi}_i)\rho_{gi}}{S} \right\} (y'_2 - y'_1) \tag{7}$$

The porosity of each stratigraphic unit ($\bar{\phi}$) (**Eq. (8)**) is estimated from the equation:

$$\bar{\phi} = \frac{\phi_0}{c} \cdot \frac{\exp(-cy'_1) - \exp(-cy'_2)}{y'_2 - y'_1} \tag{8}$$

Finally, the tectonic driving subsidence (*Y*) (**Eq. (9)**), with the decompacted subsidence corrected for paleo-bathymetry and eustasy (S^*) as the result of backstripping is given by:

$$Y = S^* \left(\frac{\rho_m - \bar{\rho}_b}{\rho_m - \rho_w} \right) \tag{9}$$

The effects of incorporating water-depth (**Figure 7a**) as well as sea-level change (**Figure 7b**) are also described by Allen and Allen (2013). Following all the numerical processes in the

decompaction and backstripping procedure, the burial-history curve is produced together with backstripped PWD maps for all of the sequences available (**Figure 8**).

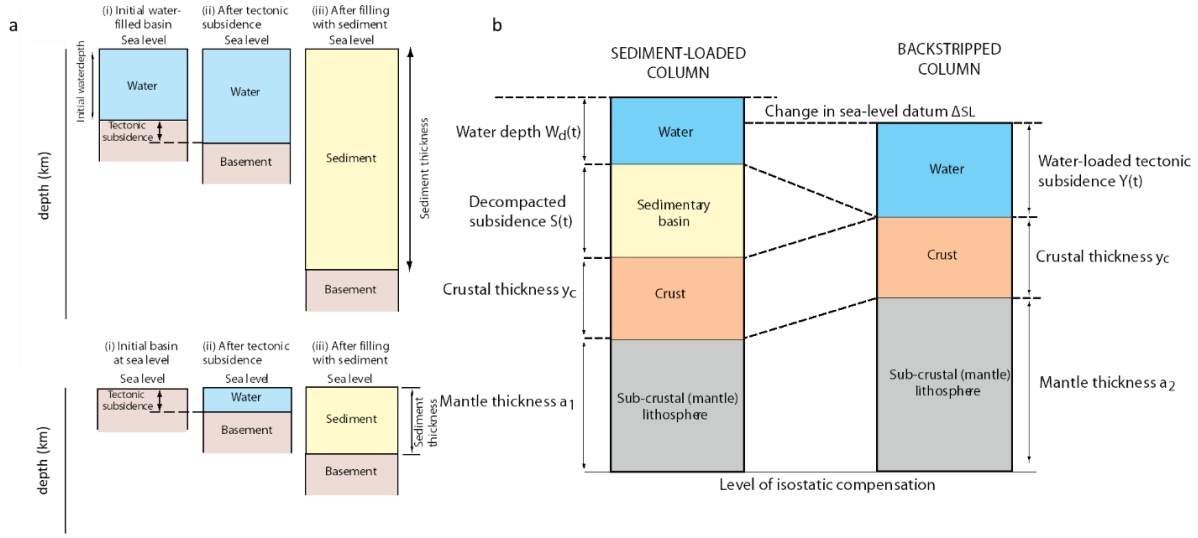

Figure 7. (a) The effects of initial water-depth on sediment thickness. (b) The effect of sea-level and isostatic balance during the backstripping process. Modified after Allen and Allen (2013).

The backstripped PWD maps are then validated using a fuzzy logic sedimentary model approach (Felix et al., 2012). This model incorporates the SF data, age data and other input data including present day depths, formation property, and paleo-coastline. The approach of fuzzy logic sedimentary modelling uses various variables including water-depth, distance to shore, and degree of slope as an input to determine the sedimentary facies model. A SF value is then assigned to each sedimentary facies. In the fuzzy logic sedimentary model, intuitive definition is used to produce a strict sedimentary facies distribution, but a 'fuzzy' SF distribution (de Jager, 2016). The fuzzy logic sedimentary model is illustrated in **Figure 9**. This fuzzy logic approach is also used in the source rock distribution modelling with OF-Mod 3D.

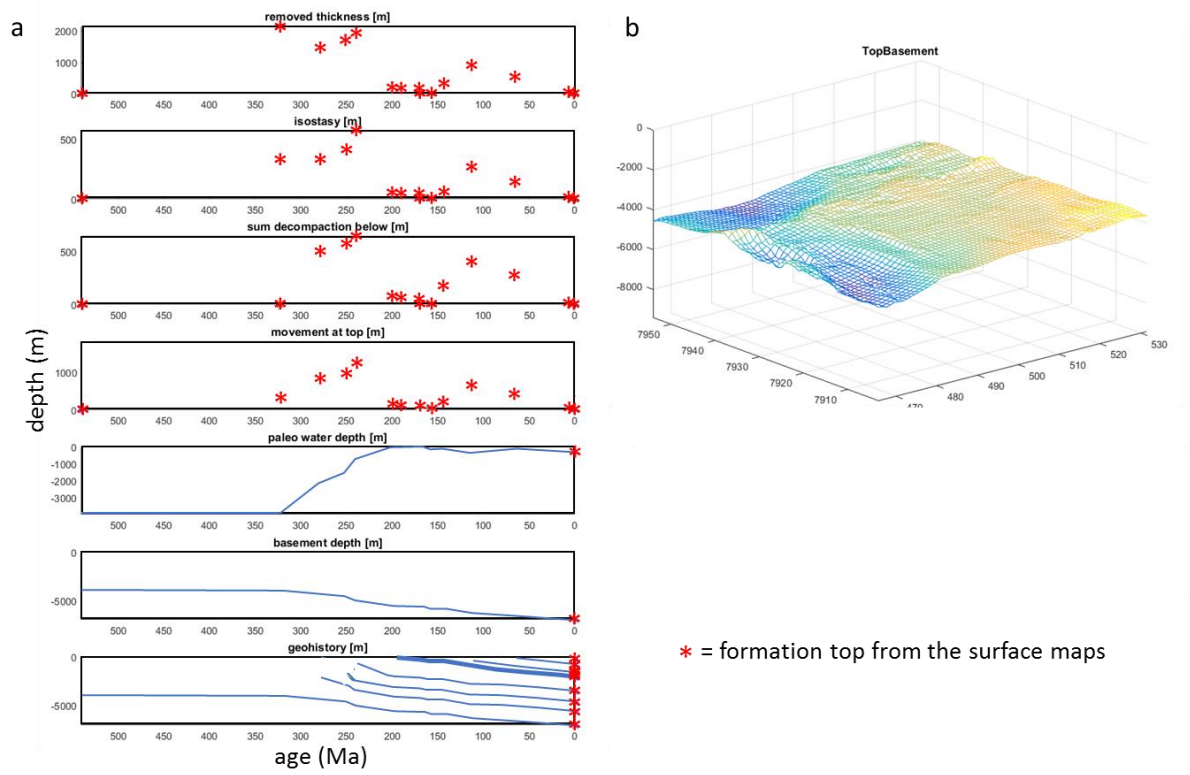

Figure 8. The results of decompaction and backstripping simulation using SINTEF Matlab PWD-toolbox. (a) Detailed outputs for each stage of the simulation. (b) An example of result A (**Figure 5**): 3D backstripped map of the top Basement.

The validation process results are shown in plots regarding the fuzzy logic sedimentary facies, calibrated trend-line (modelled vs measured SF), and best-fit water-depth change. Validation of fuzzy logic sedimentary facies was taken into account to see the lateral distribution of the SF, distance to shore, slope, as well as sedimentary facies to determine whether the fuzzy logic was geologically acceptable or not in the HB (**Figure 10**).

In the validation process, the measured V_{sh} and modeled V'_{sh} for changes of different water-depth (n) were compared of each available well (**Figure 11**). Root Mean Square Error ($RMSE_w$) was then calculated for each well and averaged for each formation PWD model as cumulative mean error (E_m) (Emmel et al., 2015), as shown in the **Eq. (10)** and **Eq. (11)** respectively:

$$RMSE_w = \sqrt{\frac{\sum \left(V_{shale} - V'_{shale}\right)^2}{n}} \tag{10}$$

$$E_m = \frac{\sum RMSE_w}{n_w} \tag{11}$$

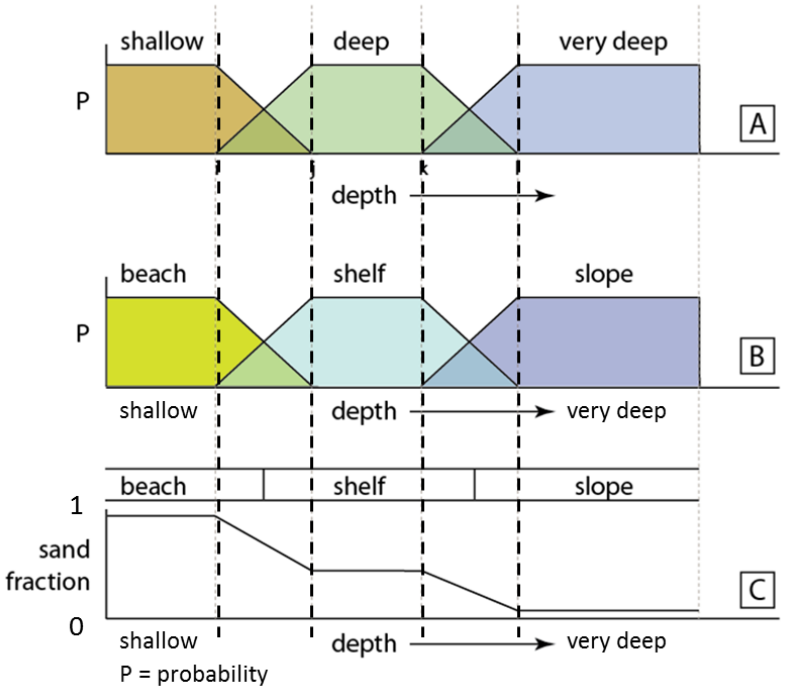

Figure 9. Fuzzy logic sedimentary model. In the example, if water-depth (A) is shallow, facies (B) is beach assigned by high sand fraction value (C). Modified after de Jager et al. (2016). P: probability.

In this study, change of water-depth was simulated to vary in the range of ± 200 m with 20 m increment and was evaluated in terms of error for every increment to get the best-fit water-depth model in comparison to the reference model (**Figure 12**). The water-depth with the lowest E_m value was chosen as the best-fit model for the corresponding formation considering the $RMSE_w$ from each well likewise (**Figure 12**). In general, the simulation shows that shallowing water-depth by more than 200 m will cause a considerable error to the PWD model.

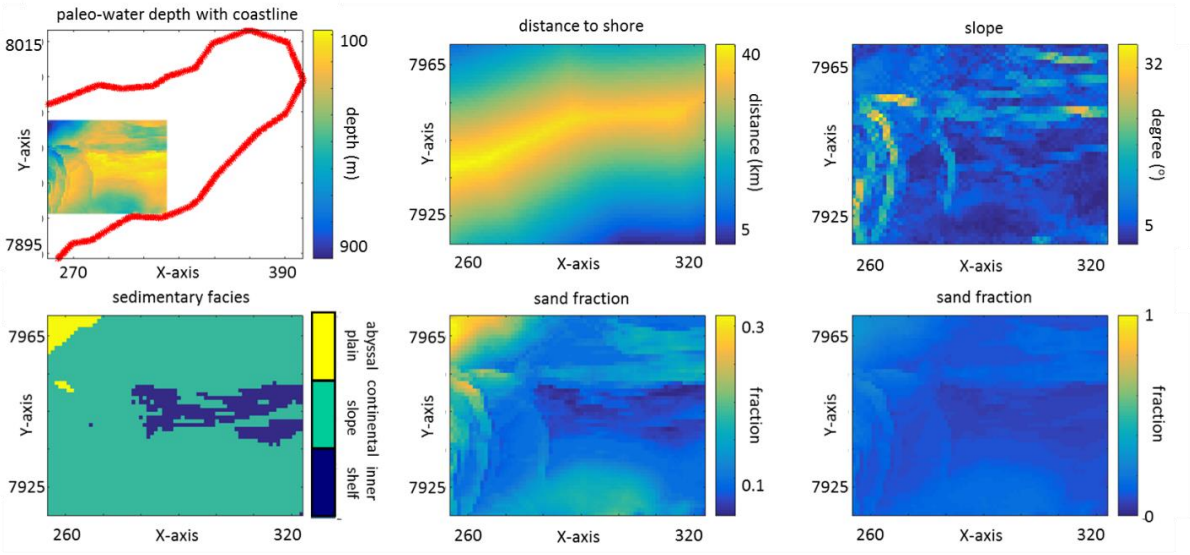

Figure 10. Lateral distribution of the fuzzy logic sedimentary model parameters in the Hammerfest Basin (the Late Jurassic Interval).

The best-fit water-depth change for each formation is taken into account in reconstructing the PWD maps. This was done in Petrel by shifting the backstripped PWD maps from decompaction and backstripping simulation with an amount of water-depth change according to the best-fit water-depth model from the validation process in the SINTEF Matlab PWD-toolbox. These reconstructed PWD maps are used as one of the main inputs in source rock distribution modelling in the OF-Mod 3D. Due to the lack of SF-data, this study was performed for the top The Early Cretaceous Interval and top The Late Jurassic Interval, but not for the Middle Triassic Kobbe Fm. Therefore, Kobbe Fm source rock distribution modelling used only backstripped PWD maps but was not validated.

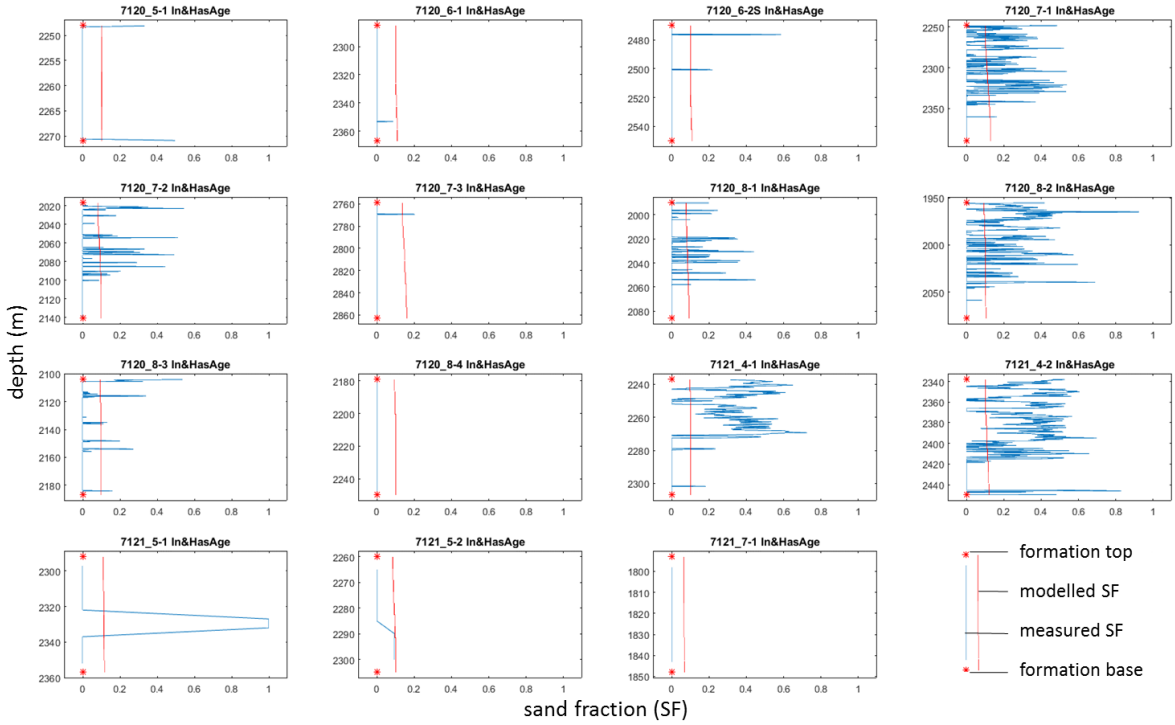

Figure 11. Modelled and measured sand fraction (SF), bounded by formation top and base, for each well in the study area.

3.2.3 Source rock distribution modelling

The source-rock distribution modelling of the three important source rock intervals in the HB used SINTEF in-house OF-Mod software. OF-Mod or organic facies modelling software is a process-based sedimentological tool used to model the deposition of marine siliciclastic sediments containing high amounts of organic matter in order to evaluate the source rock potential distribution both in terms of quantity and quality (de Jager et al., 2015). From inorganic facies modelling to organic facies modelling, OF-Mod is linking the basin fill/process stratigraphy with organic-matter source type and preservation conditions during deposition and burial (**Figure 13**). The main output of the modelling is source rock distribution in both space (lateral) and time (vertical) dimension (Mann and Zweigel, 2009). The workflow of source rock distribution modelling is summarized in **Figure 14**. In general, the modelling is divided into two stages, inorganic facies modelling and organic facies modelling. Inorganic facies is modelled separately from organic facies modelling to develop the organic model without re-running the inorganic model. This makes the organic facies modelling faster as it needs some testing on organic parameters and multiple scenario runs.

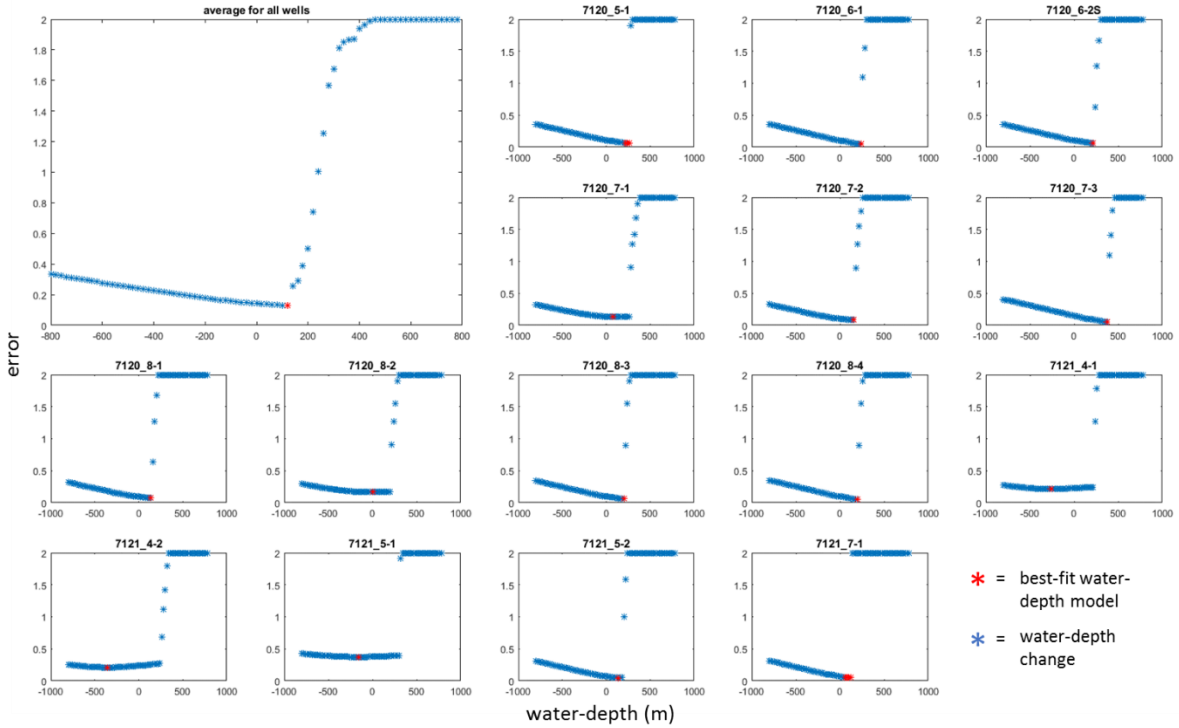

Figure 12. Water-depth change simulation to obtain best-fit water-depth model for the corresponding formation/interval (in example The Late Jurassic Interval). The large figure shows the cumulative mean error (E_m) while the rest show root mean square error ($RMSE_w$) from each well. A change of water-depth by >200 m causes a considerable error to the model.

Inorganic facies modelling

Inorganic facies modelling uses present-day bathymetry and paleo-bathymetry maps, sea-level curves, paleo-coastline to model the 3D distribution of SF, PWD, sedimentation rate, and sediment dry bulk density (DBD) of the source rock interval interest which are essential for organic facies modelling. The SF model was validated using calculated V_{sh} in each available well in the basin. In the inorganic facies modelling, a forward modelling approach is used to give a better understanding of process stratigraphy and other processes such as isostatic adjustment through decompaction processes, sea-level change, and paleo-coastline trajectory (Mann and Zweigel, 2009), that may give better prediction for exploration areas with limited well-control.

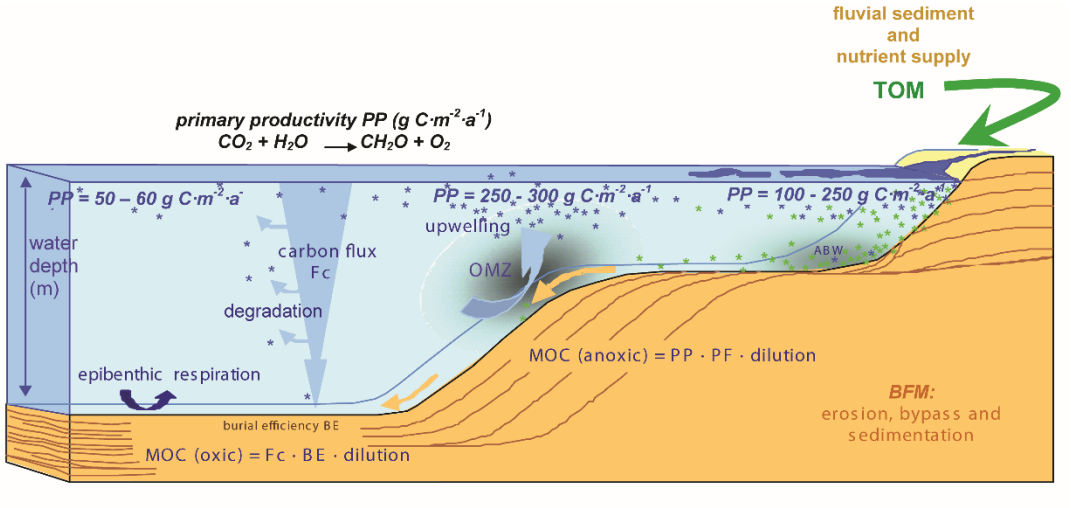

Figure 13. Conceptual model of OF-Mod: linking the basin-fill process with organic-matter source type and preservation condition to model both inorganic and organic facies. TOM: terrigenous organic matter; BFM: basin-fill model; MOC: marine organic carbon; PF: preservation factor; Fc: carbon flux; BE: burial efficiency; ABW: anoxic bottom water; OMZ: oxygen minimum zone (Mann and Zweigel, 2009).

Process stratigraphy concerns with the dynamics of the stratigraphy controls including the volume and granulometry of the sediment supply and the rate of generation and spatial distribution of accommodation (Catuneanu, 2006). By incorporating these factors, the stratigraphy of the basin-fill can be further analyzed through space and time, especially in terms of a mass or volume balance, between accommodation space generation and sediment flux. Rather than simply base-level change, process stratigraphy emphasizes the effects of changing accommodation space and sediment supply on the basin-fill stratigraphy (Catuneanu, 2006).

In building the model, vertical grid discretization of the model is based on sea-level curves from Miller et al. (2005) and Haq et al. (1987). The models are subdivided into 100 sub-layers to get a better vertical resolution in the stratigraphic units especially regarding sandy-shaly (SF) distribution and thickness variation. The thickness of a stratigraphic unit is measured from two present-day depth maps representing the top and base of the interval. The vertical variation may affect the different process stratigraphy results including PWD, sedimentation rate, and DBD as well as organic matter distribution within the interval. Formation is subdivided, applying a "sediment-partitioning method", into sub-layers equally, duration of each layer is related to sea-level; high sea-level will produce low sedimentation rate and vice versa (de Jager et al., 2016).

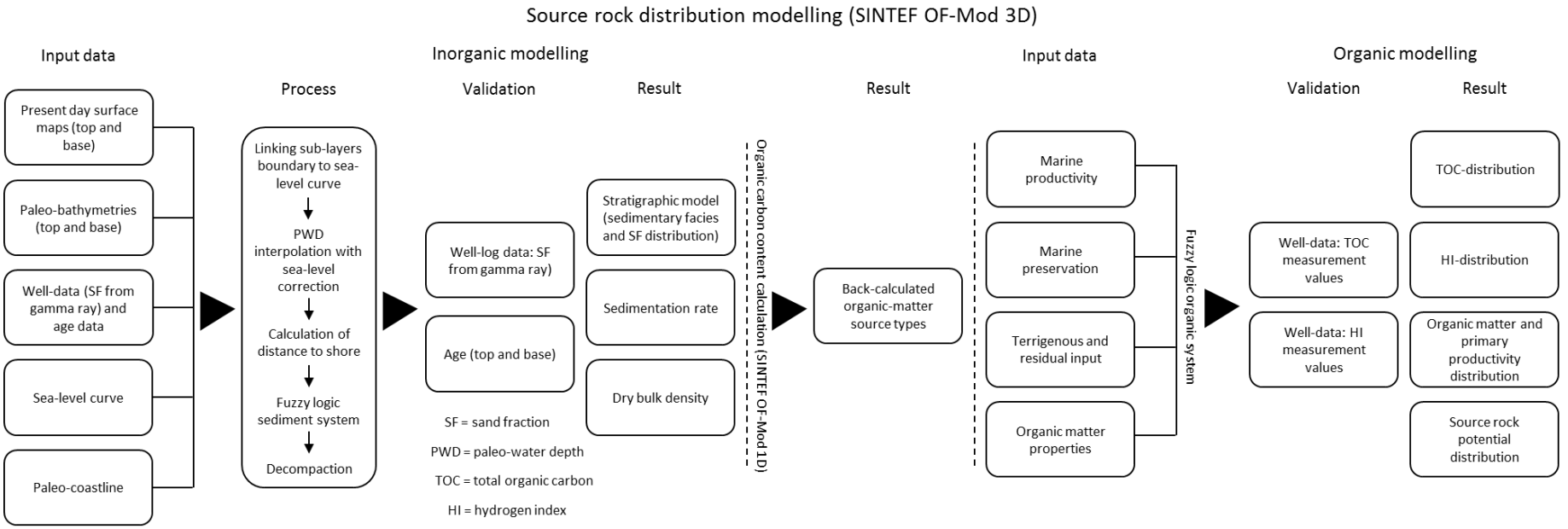

Figure 14. The general workflow of source rock distribution modelling using SINTEF OF-Mod 3D/1D from inorganic facies modelling to organic facies modelling to produce source rock distribution in terms of quantity (TOC) and quality (HI).

As primary productivity, sediment supply to the basin, as well as organic matter input vary with proximity of the basin to the coastline, paleo-coastline is one important factor in the modelling process. In OF-Mod, the paleo-coastline trajectory changes through time can be loaded to model the progradation-retrogradation or narrowness of the basin and required when coast cannot be found in PWD model.

Sand fraction spatial distribution is modelled by employing a fuzzy logic sedimentary model. It has the same principle as the paleo-bathymetry reconstruction fuzzy logic. However, instead of assigning one SF value for each sedimentary facies, in the OF-Mod, a series of values that vary through time can be assigned to single facies. It gives better vertical SF variation accordingly. Additionally, it is possible to add a lens of local SF increase by adding delta or turbidite during the input process.

The SF, as well as other interpolated input, is simulated in the decompaction process to produce sedimentation rate and sediment DBD. In the decompaction process, porosity-depth relationships, using the initial porosity of 0.49 and 0.75 and coefficient of 2.7E-4 and 4.4E-4 for sand and shale correspondingly, were assumed as the input parameters following the decompaction equation in **Eq. (4)**.

The PWD and the inorganic model results including SF, sedimentation rate, and sediment DBD, are exported into 1D data for each well to model the organic model in the OF-Mod 1D. Validation of the inorganic model uses calculated SF data in the well as well as ages derived from the NPD lithostratigraphic chart of the HB. By assigning a series of SF values instead of a single SF value, a better fit of modelled and measured SF could be achieved. However, multiple runs are sometimes required to fit the modelled and measured SF, especially by changing the SF values and trend in the fuzzy logic sedimentary model. The model is more reliable and might give better input for organic facies modelling in the OF-Mod 1D. The result of inorganic modelling incorporation with geochemical input data determined the amount and distribution of organic matter as well as source rock potential for each sub-layer.

Organic facies modelling

Source rock deposition is highly dependent on marine preservation (bacterial degradation and scavenging-reworking by benthic fauna), water-depth (transit time of organic matter in the water-column), sediment grain size, and sedimentation rate (Allen and Allen, 2013). In order to develop a comprehensive source rock model, OF-Mod considers all of those factors during the organic facies modelling by introducing inorganic facies modelling results as well as geochemical data from the wells (TOC and HI). Additionally, since the type and preservation

of organic matter deposited on the shelf is directly correlated with the basin-fill stratigraphy, linking organic-matter deposition and process stratigraphy is important procedure in the source rock modelling (Mann and Zweigel, 2009). For example, organic matter distribution is related to the depositional sequence stratigraphy, which is highly dependent on the shoreline trajectory (Pasley et al., 1993). Another example is increase of organic matter preservation in the sediment may correspond to increase of sedimentation rate as short oxygen exposure time and intense organic degradation occurred (Hartnett et al., 1998).

The organic facies model is constructed based on interplay of three organic matter source types (de Jager et al., 2015):

- Marine organic matter (MOM); which are produced by primary productivity at the upper water-column and degraded during settling to the sea-bottom. It consists of kerogen type I and II and has high HI and low Oxygen Index (OI).
- Terrigenous organic carbon (C_{terr}); which comes from the continent through sedimentation processes. It is generally type II or II kerogen dominated and has intermediate HI and OI.
- Residual organic carbon (C_{res}); which are detrital organic matter and will not produce significant hydrocarbons. It consists of a large part of type IV kerogen (inertinite) and has very low HI and high OI.

The TOC, OI, and HI values are calculated by determining the fraction of three organic matter source types content based on their relative concentrations in the total organic matter (de Jager et al., 2015). Back-calculation is performed using the scheme described in Justwan and Dahl (2005), employing the kinetic scheme Pepper Type B by Pepper and Corvi (1995). The model is validated using this back-calculated, initial TOC, and HI values, since OF-Mod model the original deposition (de Jager et al., 2015).

Another back-calculation, "process-based back-calculation", is performed in OF-Mod 1D. The process-based back-calculation allowed the measured TOC and HI data, together with the inorganic facies modelling results, to be back-calculated in order to obtain the value of each organic matter source type and how their fractions contribute to the total organic matter (Felix, 2014). Process-based back-calculation determine the ‘unknown’ organic matter content in the TOC by performing multiple computations based on end-member values input and TOC-HI data (**Figure 15a**). Therefore, in order to get the best-fit model from the measured TOC and HI data, it is necessary to adjust the end-member values. OF-Mod is also able to show the uncertainty between different computations in finding the best-fit ‘unknown’ of each organic

matter source type to match the fractions of the total organic matter (**Figure 15b)**. An illustration of process-based back-calculation with the involved formula and standard end-member values, and also an example of how OF-Mod calculates the uncertainty are shown in **Figure 15**.

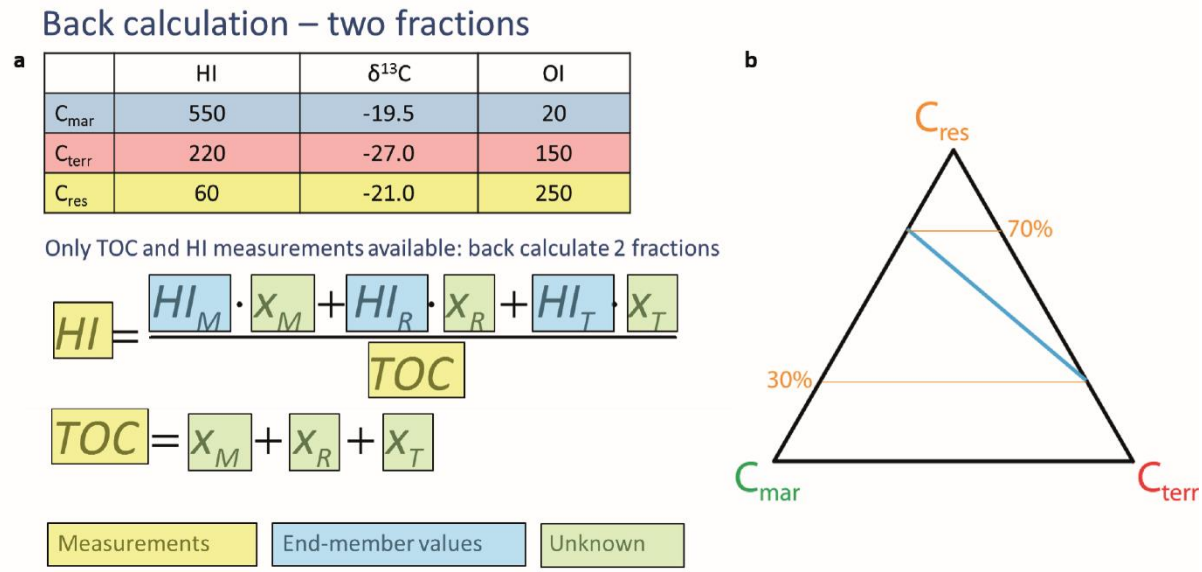

Figure 15. (a) Upper part: end-member values used for process-based back-calculation; lower part: process-based back-calculation of organic-matter source type from two fractions of measurement (TOC and HI). (b) Uncertainty in determining the 'unknown' in the process-based back-calculation. HI: hydrogen index; $\delta^{13}C$ = delta carbon 13; OI: oxygen index; TOC: total organic carbon; M= C_{mar} = marine organic carbon; T = C_{terr} = terrigenous organic carbon; R = C_{res} = residual organic carbon (de Jager et al., 2015; Felix, 2014).

Since the Early-Mid Triassic Interval only has one well penetration, additional geochemical data from other wells nearby in the HB are imported to give improved information regarding the organic matter source types. Careful consideration for the Early-Mid Triassic Interval is taken into account in analyzing the trend-line results as different locations may have diverse geological setting and basin-fill process. The results of 1D organic facies modelling are then exported to be further analyzed regarding the average trend-line of the organic matter source types for each source-rock interval. It is not necessary to use the average trend as the input for OF-Mod 3D. However, by analyzing the OF-Mod 1D back-calculation results, better input for OF-Mod 3D can be obtained. These process-based back-calculated organic matter are utilized as the main input, which are primary productivity, terrigenous, and residual organic matter, for organic facies and source rock distribution modelling in the OF-Mod 3D. Additionally, the same end member values of OF-Mod 1D are applied in the OF-Mod 3D as the organic facies setting.

OF-Mod considers three organic-matter source types, marine (autochthonous), terrestrial (allochthonous), and residual organic matter, in which every source type has different

deposition setting and preservation condition. The preservation conditions of organic matter during deposition and burial will affect the modelled source rock quality (Mann and Zweigel, 2009). In general, autochthonous produced MOM may experience degradation during settling in the water-column and the uppermost of sediment layer. The measured MOM fraction that reaches the sediment surface is carbon flux (CF) which corresponds to the primary productivity (PP) and water-depth (WD) as shown in the **Figure 16** and **Eq. (12)** from Betzer et al. (1984).

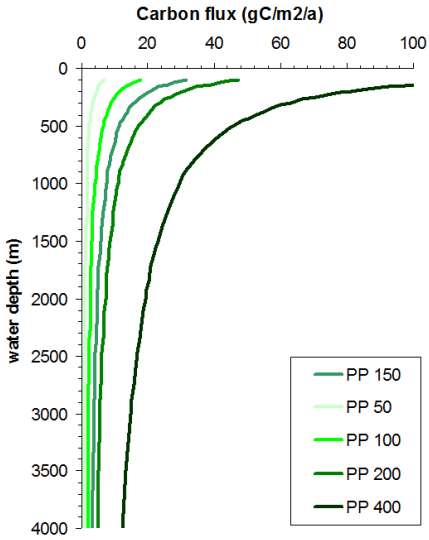

Figure 16. Calculated carbon flux of different primary productivity (PP) constant values by applying carbon flux equation from Betzer et al. (1984). Note that degradation of organic matter is faster in the upper water-column (de Jager et al., 2015).

$$CF = \frac{0.409 \cdot PP^{1.41}}{WD^{0.628}} \tag{12}$$

Commonly, PP is higher in coastal areas, where the locally increased nutrient supply most likely occurs due to upwelling or river input, than in distal open ocean areas (**Figure 17**) (Mann and Zweigel, 2009). OF-Mod calculated PP distribution as a function of distance to shore (**Figure 18**). In the PP input, distance to open ocean can be modified to vary through time as well as PP value range in the coast and ocean. Additional marine productivity can also be modelled by adding lenses in the local areas.

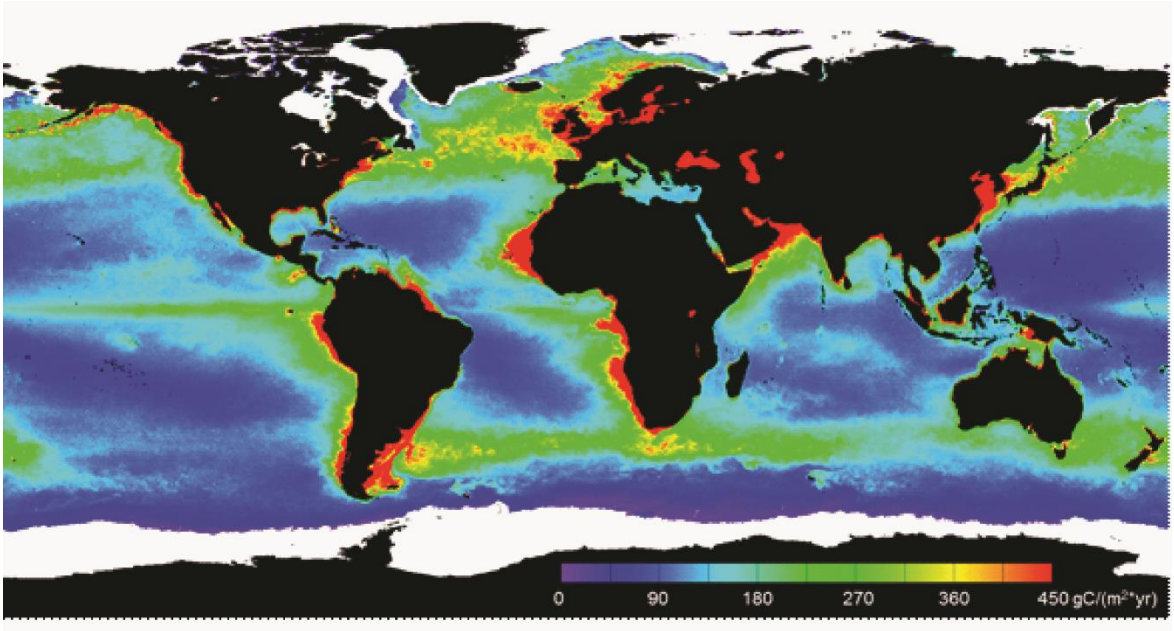

Figure 17. Primary productivity (PP) distribution in the world. Note the increased PP in the coastal and upwelling areas rather than in the open ocean (SeaWiFS Global Biosphere (September 1997-August 1998)).

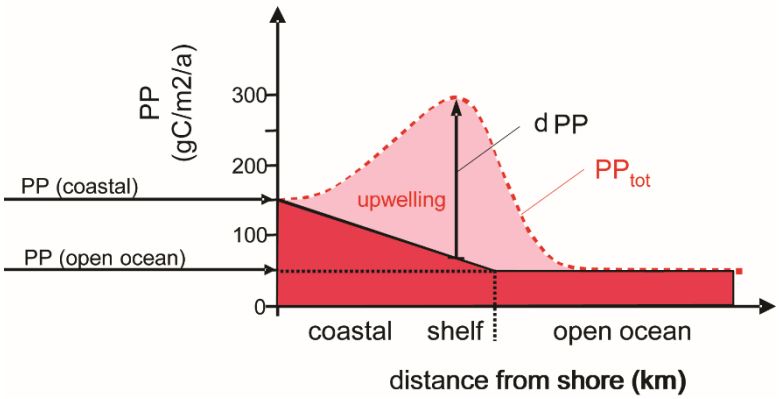

Figure 18. Primary productivity (PP) parameters plot from Mann and Zweigel (2009), modified after de Jager et al. (2015).

Based on the carbon flux data, MOM is mostly degraded in the uppermost water-column, depending on the organic particles (**Figure 16**). Another factor that improves the MOM preservation is an increase of oxygen-exposure time and burial efficiency at the sediment (Mann and Zweigel, 2009). Burial efficiency (BE) will determine the fraction of MOM that is preserved within the sediment. Sedimentation rate played a major role in defining the BE as shown by **Eq. (13)** from Betts and Holland (1991):

$$\log_{10} BE = \frac{1.39 \log_{10} SR}{\log_{10}(SR + 7.9)} + 0.34 \qquad (13)$$

In the marine preservation setting of OF-Mod, two methods of calculating the total marine organic carbon or carbon accumulation rate are well-defined, depending on the preservation conditions in terms of oxygenation, oxic and anoxic (**Figure 19**). Anoxic conditions develop where oxygen demand surpasses oxygen supply, and the vice versa for oxic conditions. Oxygen is primarily needed for degradation of organic matter. On the other hand, supply of oxygen mainly comes from the circulation of oxygenated water as a result of mixing by waves, or a cold, oxygen-bearing ocean-bottom currents movement. Anoxic conditions are more favourable for source rock deposition. However, when the sedimentation rate is very high, sometimes source rock might be deposited under oxic conditions generally (Allen and Allen, 2013). In the OF-Mod, carbon accumulation rate (CAR) in oxic conditions is calculated based on CF and BE as shown by **Eq. (14)** (Mann and Zweigel, 2009):

$$CAR = CF \cdot BE \tag{14}$$

On the contrary, anoxic conditions, in which PP and PF play an important role in defining the CAR, is computed by using the **Eq. (15)** (Mann and Zweigel, 2009):

$$CAR = PP \cdot PF \tag{15}$$

Increased preservation of MOM may happen in anoxic conditions as oxygen consumption by degradation process surpasses the oxygen supply reducing the aerobic degradation processes (Mann and Zweigel, 2009). Anoxic preservation conditions are therefore approached by using **Eq. (15)** instead of **Eq. (14)** in the OF-Mod. In this study, the scenario used for the preservation condition is oxic environment as one of the main focus is to compare various basin-fill processes on source rock distribution from three different source rock intervals.

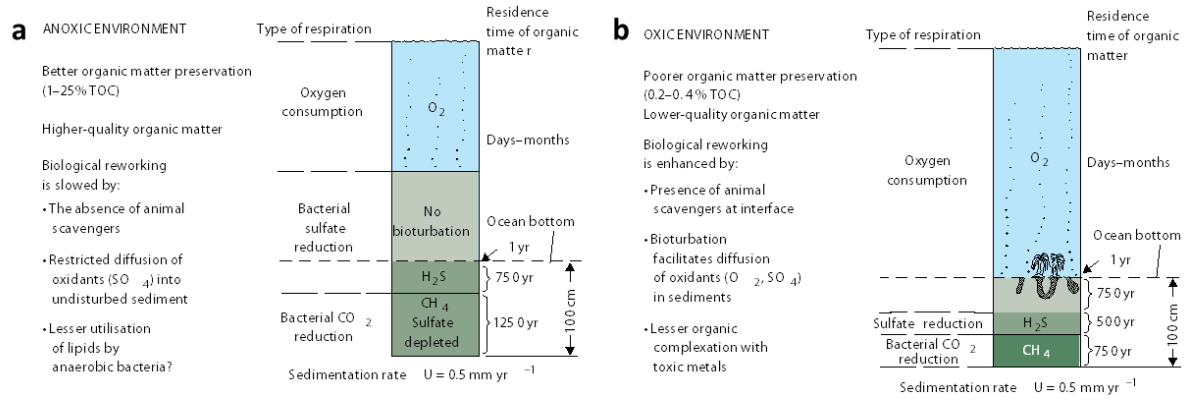

Figure 19. Organic-matter preservation under (a) anoxic and (b) oxic conditions. An anoxic environment is more favorable for organic-matter preservation (Allen and Allen, 2013).

The allochthonous organic matter is also an important fraction to be taken into consideration in organic facies modelling as 90% of OC burial occurrs in continental margin sediments (Hartnett and Devol, 2003) and in about 50% of shelves organic matter deposition

originates from terrestrial sources (Schlünz and Schneider, 2000). C_{terr} is not produced in situ in the marine environment and rather enters the basin through continental transport such as fluvial system and run-off (Mann and Zweigel, 2009). Since C_{terr} has already experienced degradation during continental transport, it is more resistant from further marine degradation in the marine basin (Hedges and Keil, 1995). The further the distance from the shoreline, the less grain size and quality of C_{terr} in the depositional area (Littke et al., 1991) and the more chemical degradation C_{terr} could experience as indicated by increase of inertinite/vitrinite ratio, except when the turbidity currents take control (Littke et al., 1997). In OF-Mod, the distribution of C_{terr} is highly associated with SF in which higher SF tends to consist of more C_{terr}. However, it is not necessary that pure sand will always have high C_{terr} due to winnowing of the lower density of organic particles in highly hydrodynamic regimes (Mann and Zweigel, 2009) (**Figure 20**). In addition, C_{terr} distribution varies laterally according to sedimentation rate. Higher sedimentation rate is induced by higher sand discharge, in consequence higher C_{terr} will be modelled across these areas (Mann and Zweigel, 2009). Nonetheless, C_{res} follows a different trend from C_{terr} as C_{res} will be highest with low SF (de Jager et al., 2015) (**Figure 20**). C_{res} is mainly sourced from the degradation of organic matter in the sink.

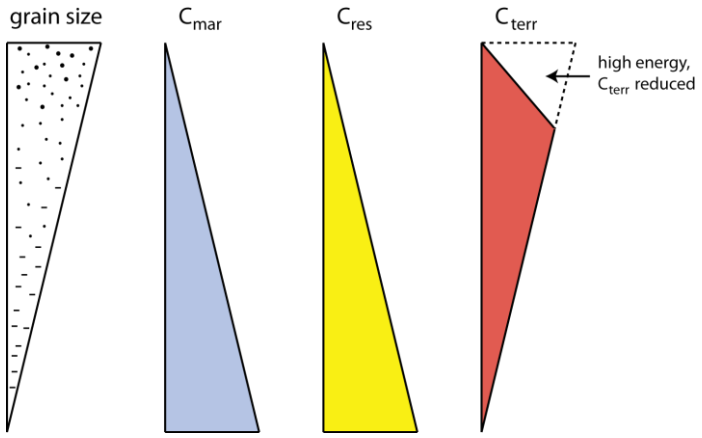

Figure 20. Hydrodynamic equivalence between average grain size of sediment and three organic-matter source types. $C_{mar:}$ marine organic carbon; C_{terr}: terrigenous organic carbon; $C_{res:}$ residual organic carbon (de Jager et al., 2015).

One of the main outputs of organic facies modelling is source rock quantity and quality distribution, represented by TOC and HI respectively. TOC is calculated by the fraction of the total organic matter (W_{Corg} (g)) in total weight from both W_{Corg} and inorganic matter weight (W_{Cinorg} (g)) (**Eq. (16)**). W_{Corg} consists of MOM, C_{terr}, and C_{res} ($gC/m^2/a$), while W_{Cinorg} is computed based on sedimentation rate (SR) (cm/ka) and sediment dry bulk density (DBD) (g/cm^3).

$$TOC = \frac{W_{C_{org}}}{W_{C_{org}} + W_{inorg}} = \frac{C_{mar} + C_{terr} + C_{res}}{C_{mar} + C_{terr} + C_{res} + DBD \cdot SR} \quad (16)$$

TOC values increase with the increase of PP and SR, dominated by burial efficiency. However, at some points when SR reachs ca. 10 cm/ka and higher, the TOC values are decreasing due to dilution effect, following the decreasing trend of PP (**Figure 21**). The distribution of TOC and HI are computed in the OF-Mod and validation of the results is done by comparing the model with the back-calculated TOC and HI values from the well data. In order to minimize the mismatch between the measured and modelled data, re-runs of the simulation, by changing the main organic matter input, preservation condition and end-member values, are often needed. Finally, source rock potential is also examined in the OF-Mod, following the cut-off values described in **Table 3**.

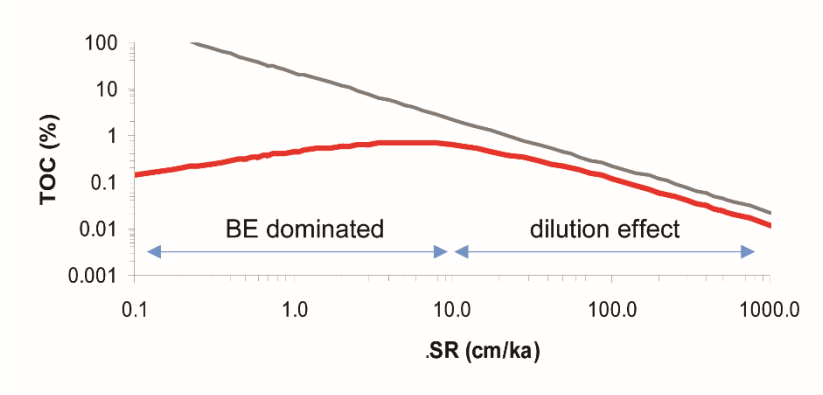

Figure 21. The relationship between sedimentation rate (SR) and primary productivity/burial efficiency (BE) and how it affects the amount of total organic carbon (TOC) modified after Felix et al. (2012).

Table 3. Source rock potential classification and their cut-off values in the OF-Mod.

TOC (wt.%)	HI*TOC /100	Source rock potential
>2.0	>10.0	Very good
>1.0	>5.0	Good
>0.5	>0.5	Fair
Rest	Rest	Poor

3.3 Modelling set-up

The source rock intervals of the study are bounded by formation tops based on avaliable surface maps from Statoil. NPD lithology descriptions and the lithostratigraphic chart helped determining the ages of the formation tops. The study also referred to several works, including Bugge et al. (2002), Langrock et al. (2003), Glørstad-Clark et al. (2010), Glørstad-Clark et al. (2011), Halland et al. (2013b), and Georgiev et al. (2017) in determining the age as well as the

sub-division of the intervals. Accordingly, the study divided the Early Cretaceous and Early-Mid Triassic Intervals into several formations, while the Late Jurassic Interval (the Hekkingen Fm) is discretized into two members. The sub-division of the intervals is summarized in **Table 4**.

3.3.1 PWD reconstruction

The PWD model was built on a grid of 672x526 cells with lateral resolution of 100 m and vertical discretisation of 10 layers. Some simulation runs have been performed at low-resolution: 20 tests with water-depth change of 200 m; to high-resolution simulations that consist of 80 tests for water-depth change of 20 m, for both Early Cretaceous Interval and The Late Jurassic Interval. In the simulation, 3 hiatus periods, base Tertiary, Late Jurassic, and Middle Jurassic, are accounted as 200 m hiatus thickness. The PWD reconstruction is done using the input parameters shown in **Eq. (4)**. Porosity-depth relationship is based on (Sclater and Christie, 1980).

Table 4. Sub-division of the source rock intervals in the study area.

Boundary	Interval	Sub-division	Age (Ma)
Top Kolje Fm - Top Hekkingen Fm	Early Cretaceous	Kolje Fm	130-113
		Klippfisk Fm	134-130
Top Hekkingen Fm - Top Fuglen Fm	Late Jurassic	Krill Member	154-144
		Alge Member	157-154
Top Kobbe Fm - Top Permian	Early-Mid Triassic	Kobbe Fm	243-240
		Steinkobbe Fm	247-243
		Havert-Klappmyss Fms	251-247

Table 5. Input parameters for the decompaction and backstripping simulation in the paleo-bathymetry reconstruction.

density of sandstone	2650 kg/m^3
density of shale	2000 kg/m3
density of mantle	2100 kg/m3
density of crust	3330 kg/m3
density of water	1030 kg/m3
initial porosity	0.49
porosity-depth curve coefficient	0.00027

The paleo-coastline is digitized based on the Norwegian Barents Sea map from NPD, as illustrated in **Figure 22**. The paleo-coastline is digitized following the structural highs and platforms around the HB as depicted in **Figure 22**, which shows the narrowness of the HB.

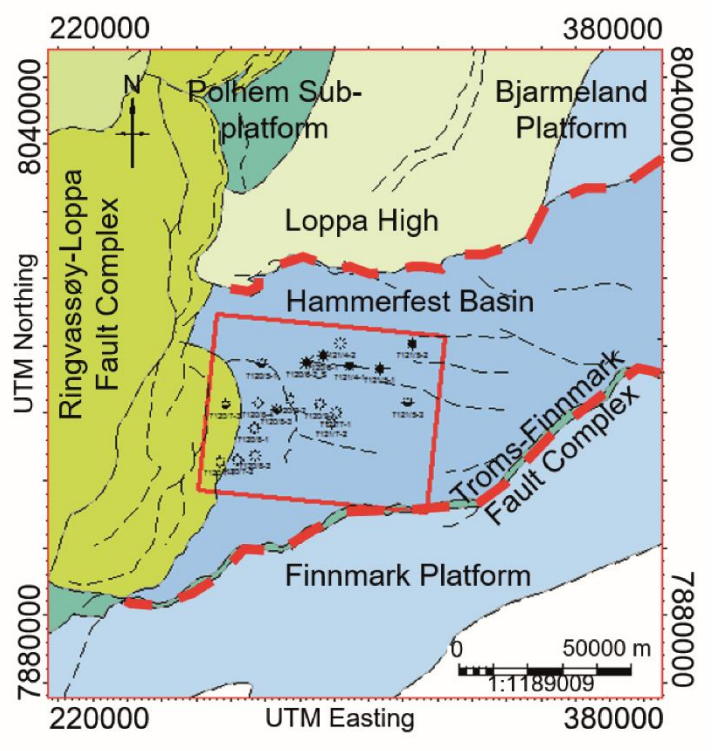

Figure 22. Paleo-coastline (red dashed line) digitization as the input for the paleo-bathymetry reconstruction and source rock distribution modelling for both Late Jurassic and Early Cretaceous Intervals in the Hammerfest Basin. Note the narrowness of the Hammerfest Basin (red square).

The simulation employing the fuzzy logic sedimentary model input is depicted in **Figure 23**. Both intervals utilize the same facies parameters of the fuzzy logic sedimentary model. An exception for the assigned SF values as different SF values have been assigned to the Early Cretaceous and Upper Jurassic intervals (**Figure 23**). Ideally, sand content is increasing toward the shallower facies and vice versa. However, for some formations, this fuzzy logic of SF distribution cannot be applied. It depends on the nature of the depositional environment and basin tectonic condition of the formation. Furthermore, sandy deposits of the Late Jurassic Interval are only found at the deeper area of the basin margins (both northern and southern), while shale cover the dominant part in the HB (Halland et al., 2013b). This is probably affected by the syn-rift tectonic setting during the deposition as well as flexural uplift that formed the bulge geometry in the HB. The tectonic development of the Late Jurassic Interval will be discussed further in the results and discussion of this study. In order to model this SF distribution, the assigned SF has been modified as shown in **Figure 23**, in which deeper facies of abyssal plain has high SF (0.4) while shallower facies of inner shelf has very low SF (0.05).

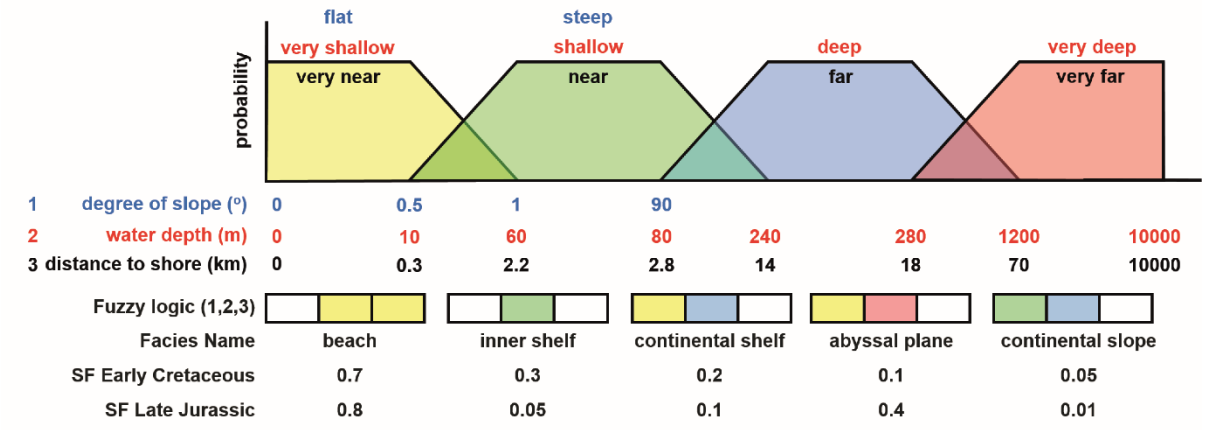

Figure 23. Fuzzy logic sedimentary model input of the Early Cretaceous and Late Jurassic Intervals. White colour shows that all the fuzzy logic parameters may be represented to define the facies name. For example, inner shelf facies can be defined by shallow water-depth in any degree of slope and in any distance to shore definitions. SF: sand fraction.

3.3.2 Source rock distribution modelling

The modelling is done in the OF-Mod by building the model with total 348.800 cells in the gridding of 67x52 cells with lateral resolution of 1000 m and vertical discretization of 100 layers. In the inorganic facies modelling part, all the parameters that are used in the PWD reconstruction are employed again in the OF-Mod, including paleo-coastline (**Figure 22**), decompaction and density parameters (**Eq. (4)**), and fuzzy logic sedimentary model (**Figure 23**) for the three source rock intervals. An exception is for the Early-Mid Triassic Interval regarding the paleo-coastline and fuzzy logic due to different tectonic setting and depositional environment in comparison with the Late Jurassic and Early Cretaceous Intervals. Shifting of shoreline trajectory through time and uplift of Loppa High in the northwestern part of the basin were taken into account in the digitization of paleo-coastline based on Glørstad-Clark et al. (2010). The fuzzy logic sedimentary model for the Early-Mid Triassic Interval employs the input parameters presented in **Figure 24**. More sandy sediment with coarsening upward vertical trend is considered for the Early-Mid Triassic Interval SF as compared to more shaly deposits of the Late Jurassic and Early Cretaceous Intervals (Bugge et al., 2002; Halland et al., 2013b). Deeper water-depth were also accounted to the fuzzy logic to see the progradation trend in the basin during Early-Mid Triassic (Glørstad-Clark et al., 2010).

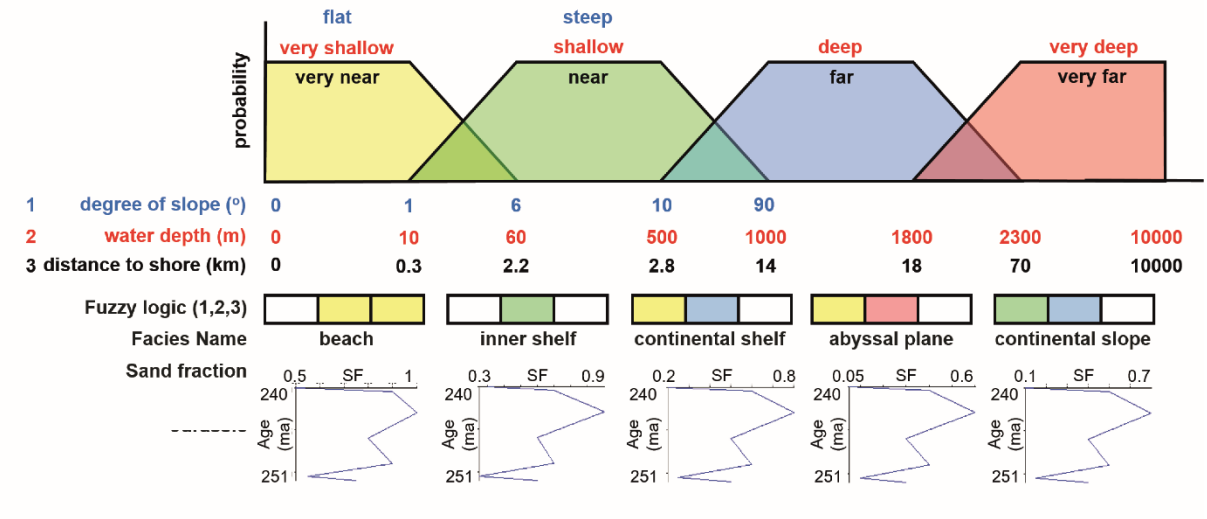

Figure 24. Fuzzy logic sedimentary model input for the Early-Mid Triassic Interval. SF: sand fraction.

Modification of SF is also implemented for both the Late Jurassic and Early Cretaceous Intervals. A range of SF values are assigned to account for the vertical variation in the interval and get a better fit between measured and modelled SF. The SF values of both intervals are shown in **Figure 25**. Since the Late Jurassic Interval has less vertical variation (mostly shale dominated), the SF is modelled as a linear trend.

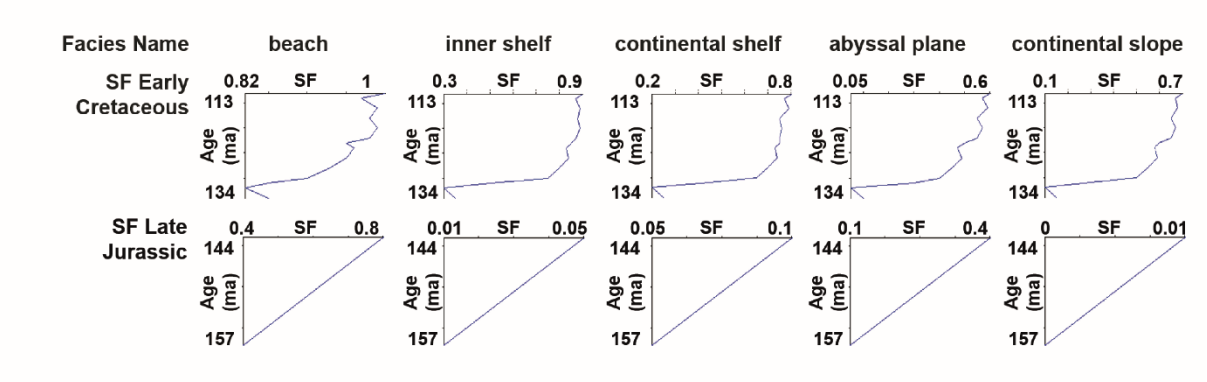

Figure 25. Modified sand fraction (SF) input for fuzzy logic of the Early Cretaceous and Late Jurassic Intervals.

Organic facies modelling is operated under oxic preservation conditions using the organic matter input from the results of OF-Mod 1D modelling. Primary productivity (PP) is modelled to be higher in the coastal areas than in the open ocean area (Mann and Zweigel, 2009). However, due to the narrowness of the HB, the values of PP Coast and PP Ocean are modelled to have small differences. In regard to PP, distance to open ocean (ca. 30 km) is assumed to be constant through time. An exception is made for the Early-Mid Triassic Interval since there is a change of shoreline trajectory during the deposition (Glørstad-Clark et al., 2010). A change

from 25 km to 30 km is assumed in the distance to open ocean input during the Early-Mid Triassic.

During Early-Mid Triassic, the period of 243-240 Ma is modelled with higher productivity (1-8 gC/m^2/a), and higher terrigenous (0.05-1 wt%) and residual OC input (1-2.5 wt%) than the period 251-244 Ma which is modelled with low PP (<1 gC/m^2/a) and low C_{terr} (<0.05 wt%) and C_{res} (<1 wt%) (**Figure 26**). The main input trend follows the back-calculation results trend with much lower value than the back-calculation. This may be caused by different data input in the OF-Mod 1D modelling, since only one well (7120/9-2) occurs in the study area, while the other wells come from various location outside the study area (**Figure 26**). The end-member values are modelled linearly with lower C_{res} value of 20 mgHC/gTOC instead of 60 mgHC/gTOC (**Figure 26**).

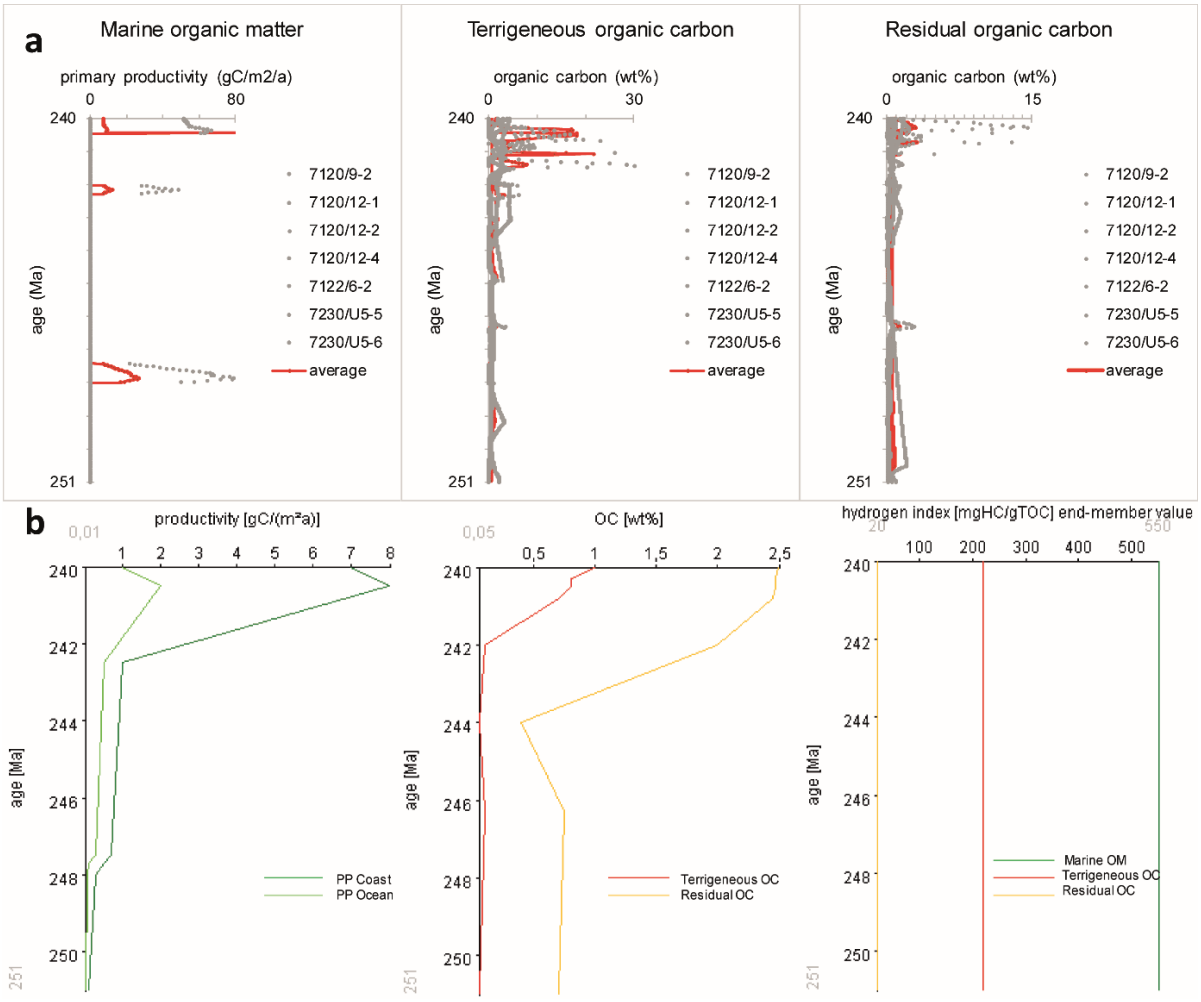

Figure 26. (a) OF-Mod 1D modelling results of the Early-Mid Triassic Interval with the average trend-line for every organic matter source type. (b) Organic-matter and end-member values input of the Early-Mid Triassic Interval for OF-Mod 3D modelling, based on OF-Mod 1D modelling results. PP: primary productivity; OC: organic carbon; OM: organic matter.

During the Late Jurassic, high values of PP (2-180 gC/m^2/a) are used to model the Hekkingen Fm with approximately decreasing trend toward the younger interval from 170-180 gC/m^2/a to 2-30 gC/m^2/a (**Figure 27**). This trend is also used in modelling the C_{terr} and C_{res} in which the lower interval corresponded to higher C_{terr} (ca. 6 wt%) and C_{res} (ca. 6.75 wt%), decreasing toward the upper interval with C_{terr} of ca. 1 wt% and C_{res} of ca. 1.75 wt% (**Figure 27**). The value is implied from a range of values in the OF-Mod 1D modelling results. An exception is made for C_{terr} since Hekkingen Fm is shale dominated, therefore C_{terr} is modelled with small values instead. End-member values of HI are modelled linearly. The lower interval (157-154 Ma) with higher organic matter input correlates to the Alge Member, while the upper interval (154-144 Ma) represents the Krill Member (Georgiev et al., 2017).

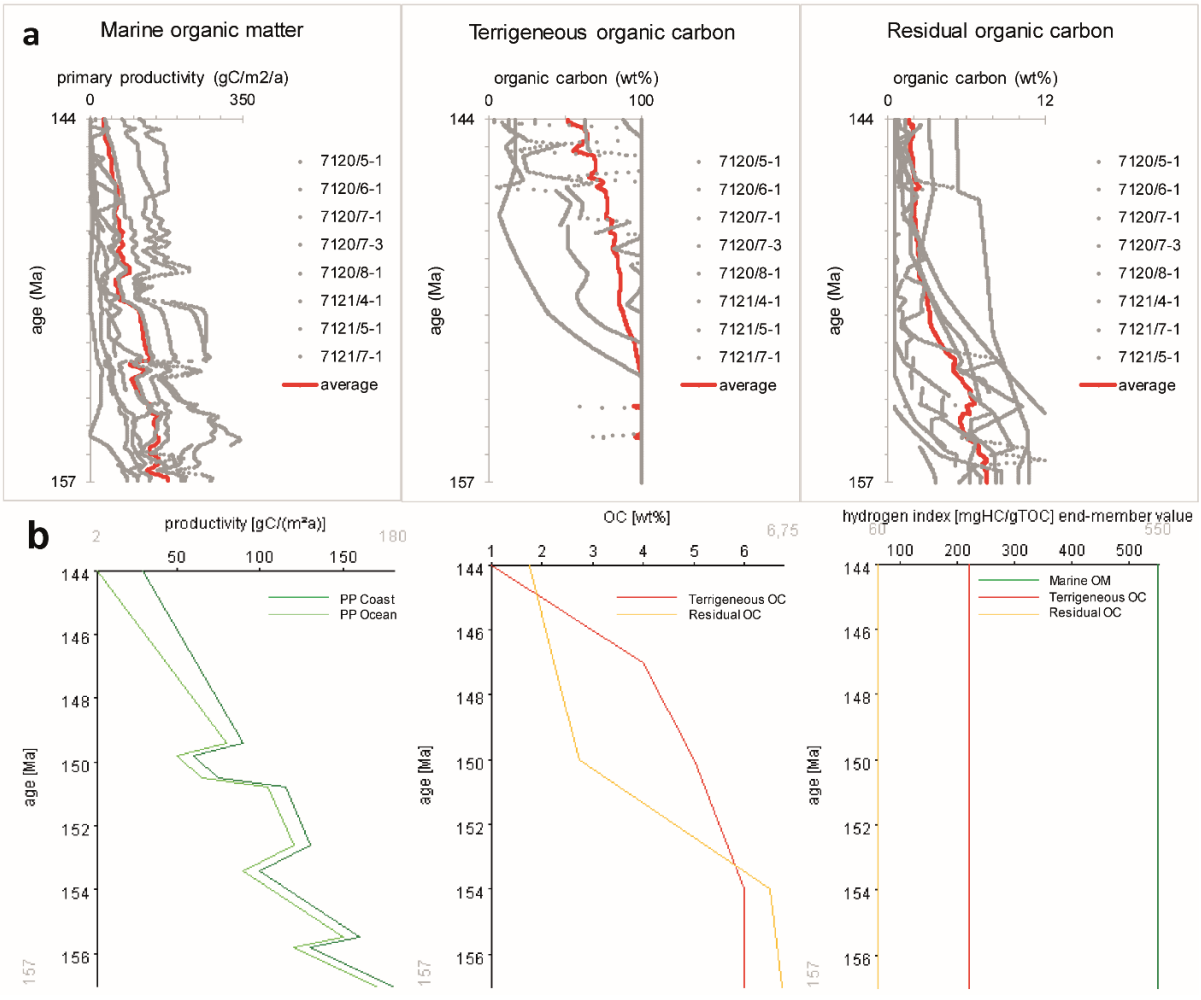

Figure 27. (a) OF-Mod 1D modelling results of the Late Jurassic Interval with the average trend-line for every organic matter source type. (b) Organic-matter and end-member values input of the Late Jurassic Interval for OF-Mod 3D modelling, based on OF-Mod 1D modelling results. PP: primary productivity; OC: organic carbon; OM: organic matter.

For the Early Cretaceous period, low values of PP (0.5-4 gC/m^2/a) are used to model the Early Cretaceous source rock with approximately decreasing trend toward the younger interval

from 3-4 gC/m^2/a to 0.5-0.75 gC/m^2/a (**Figure 28**). This trend is also used in modelling the C_{terr} in which the lower interval corresponds to higher C_{terr} (ca. 5 wt%), decreasing toward the upper interval with C_{terr} of ca. 0.5 wt% (**Figure 28**). On the other hand, in the 130-113 Ma period, C_{res} is also similary modelled as C_{terr} (decreasing trend from ca. 3 wt% to 1.5 wt%, with increasing trend during 134-130 Ma from ca. 0.5 wt% to 3 wt%. The values are inferred from the range of values in the OF-Mod 1D modelling results. An exception is for C_{terr} since the Early Cretaceous is shale dominated, therefore C_{terr} is modelled with a low value instead. End-member values of HI are modelled with decreasing trend since the two formations, the Klippfisk Fm (134-130 Ma) and the Kolje Fm (130-113 Ma), have different sediment packages, shale-carbonate and shale-sand respectively (Bugge et al., 2002; Halland et al., 2013b; Langrock et al., 2003).

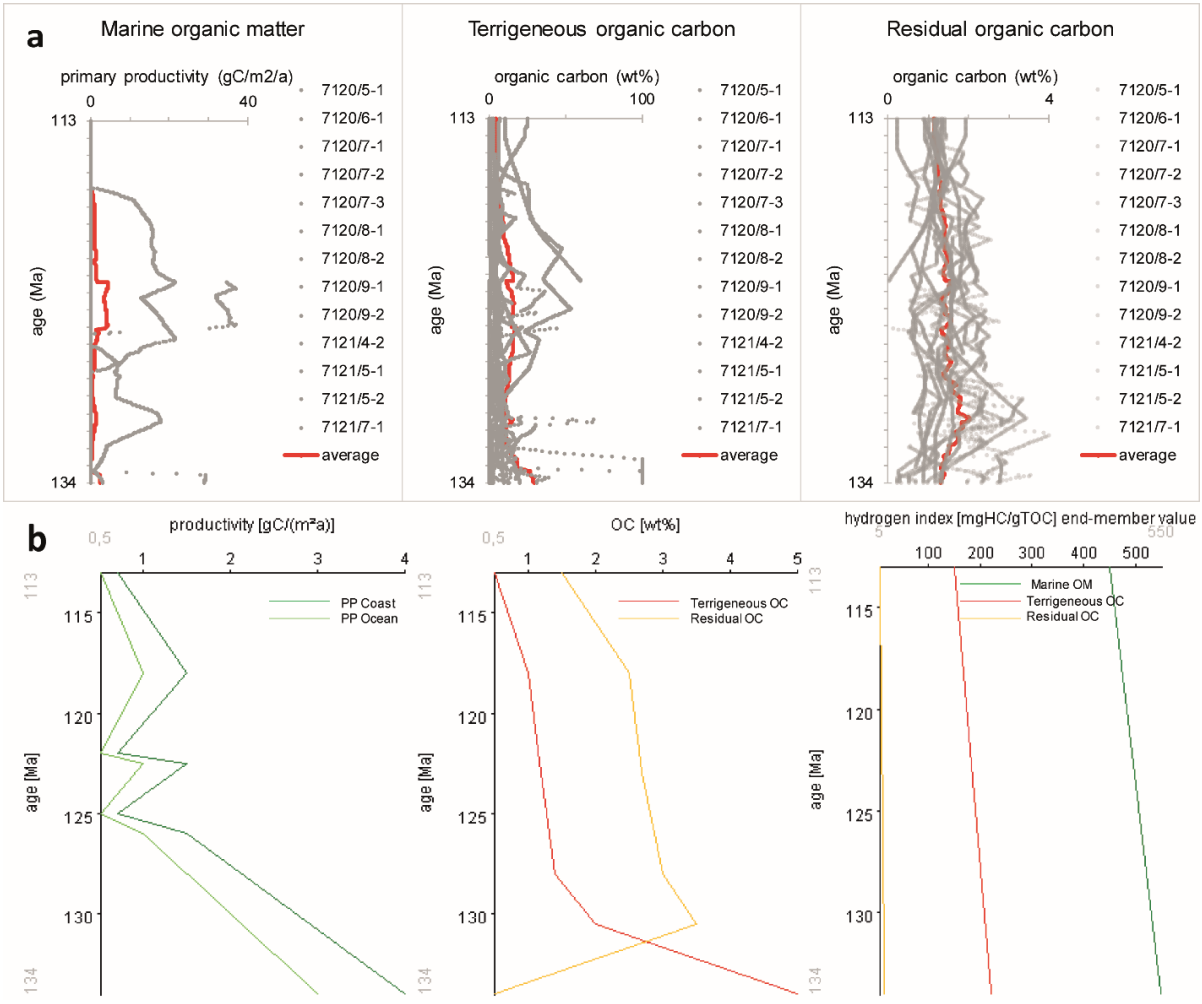

Figure 28. (a) OF-Mod 1D modelling results of the Early Cretaceous Interval with the average trend-line for every organic matter source type. (b) Organic-matter and end-member values input of the Early Cretaceous Interval for OF-Mod 3D modelling based on OF-Mod 1D modelling results. PP: primary productivity; OC: organic carbon; OM: organic matter.

Chapter 4
Results and interpretation

The paleo-bathymetry reconstruction of the research restores some of the formation tops present in the Hammerfest Basin (HB) with the focus in the Early-Mid Triassic, the Late Jurassic, and the Early Cretaceous Intervals. Therefore, further interpretation and discussion will be targeting on those intervals. In general, the three source rock intervals are deposited in the shelf facies depositional environment. Laterally, the eastern proximal part of the basin is characterized by more sandy sediments, with slower sedimentation rate and shallower paleo-water depth (PWD). The western distal area of the basin indicates deep shelf depositional environment with more shaly sediments, faster sedimentation rate and deeper PWD. An exception to this are the Late Jurassic sedimentary rocks due to the active tectonics during the deposition.

The bathymetry classification from Nagy et al. (2001) as shown in **Figure 29** is adopted to describe the paleo-bathymetry reconstruction results. Special focus of paleo-bathymetry reconstruction is given to the top Hekkingen Fm and top Kolje Fm by applying best-fit water-depth change from the PWD simulation. Additionally, sedimentation rate and sand-fraction results are described following the classification shown in **Figure 30**.

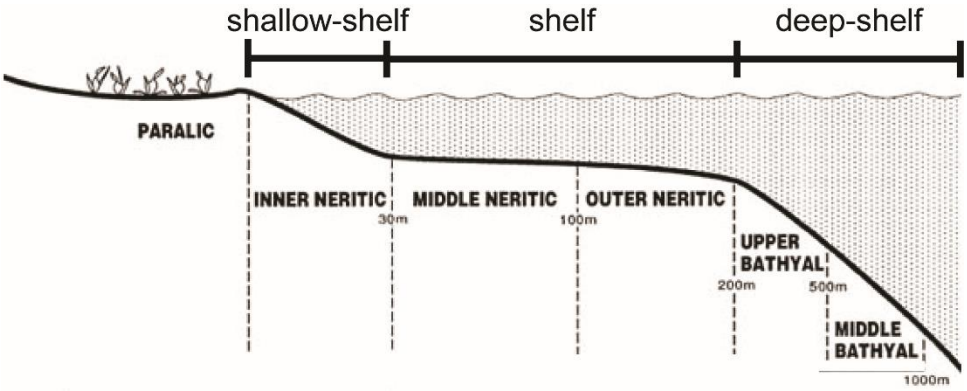

Figure 29. Bathymetry zones classification modified after Nagy et al. (2001) which is used in the study to describe the water-depth zones. Note that the terms shallow shelf, shelf, and deep shelf does not necessary represent the water depth value. Instead, they are used to describe the sedimentary facies based on the physiography of the basin.

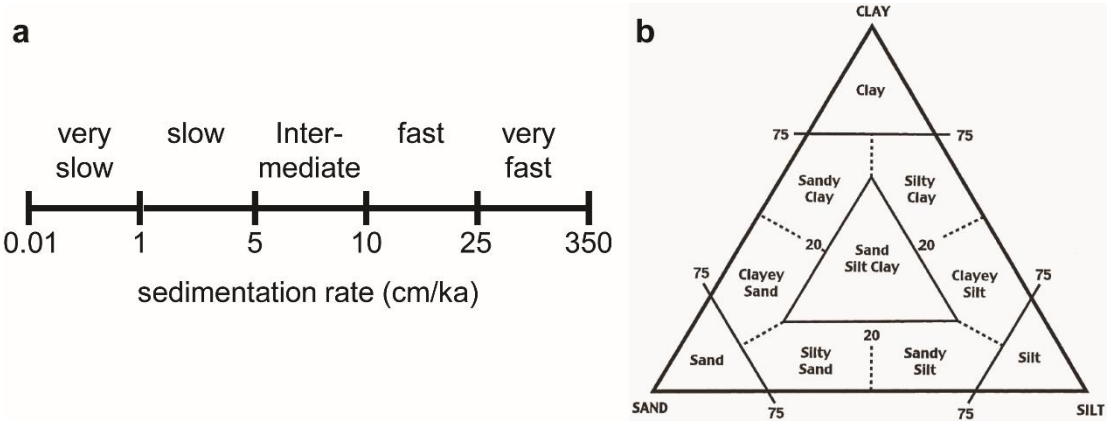

Figure 30. (a) Sedimentation rate classification. The classification is inferred from Müller and Suess (1979) regarding the sedimentation rate in the oceans, in order to describe the sedimentation rate results in the study area. (b) Ternary diagram for clastic textural groups (Shepard, 1954) which is used in the study to describe the sand-fraction groups. Note that in this study, both clay and silt are referred as shale.

The inorganic facies commonly distribute following the depositional environment and the tectonic setting of the period, validated by the sand fraction (SF) measurement from the gamma-ray log data (**Figure 31**). During the Early-Mid Triassic, the inorganic facies distribution patterns are controlled by the sedimentation as well as shoreline trajectory for the deposition of each phase. In the Late Jurassic, the different patterns of inorganic facies distribution mainly depend on the tectonic conditions during the deposition including the fault control of the basin. Variously, during the Early Cretaceous, the inorganic facies distribute as a passive infill of the remaining tectonic accommodation space from the previous active tectonic setting. The diverse inorganic facies distribution between the three omit source rock intervals may reflect varied rift stages in a widening intracratonic rift basin of the HB (e.g. Faleide et al., 2008; Larsen et al., 1993; Roberts, 2003; Roberts and Gee, 1985). On the results, the faults are only added as an illustration as faulting is not included in the modelling.

The organic facies are modelled to fit the available total organic carbon (TOC) and hydrogen index (HI) data in the wells to give more reliable results in terms of source rock quantity and quality distribution (**Figure 31**). Each modelled source rock interval is interpreted and evaluated in terms of the organic matter source type and preservation condition to reveal the source rock distribution in the basin. In general, the organic matter in the source rocks is distributed according to the basin-fill deposition and basin-architecture.

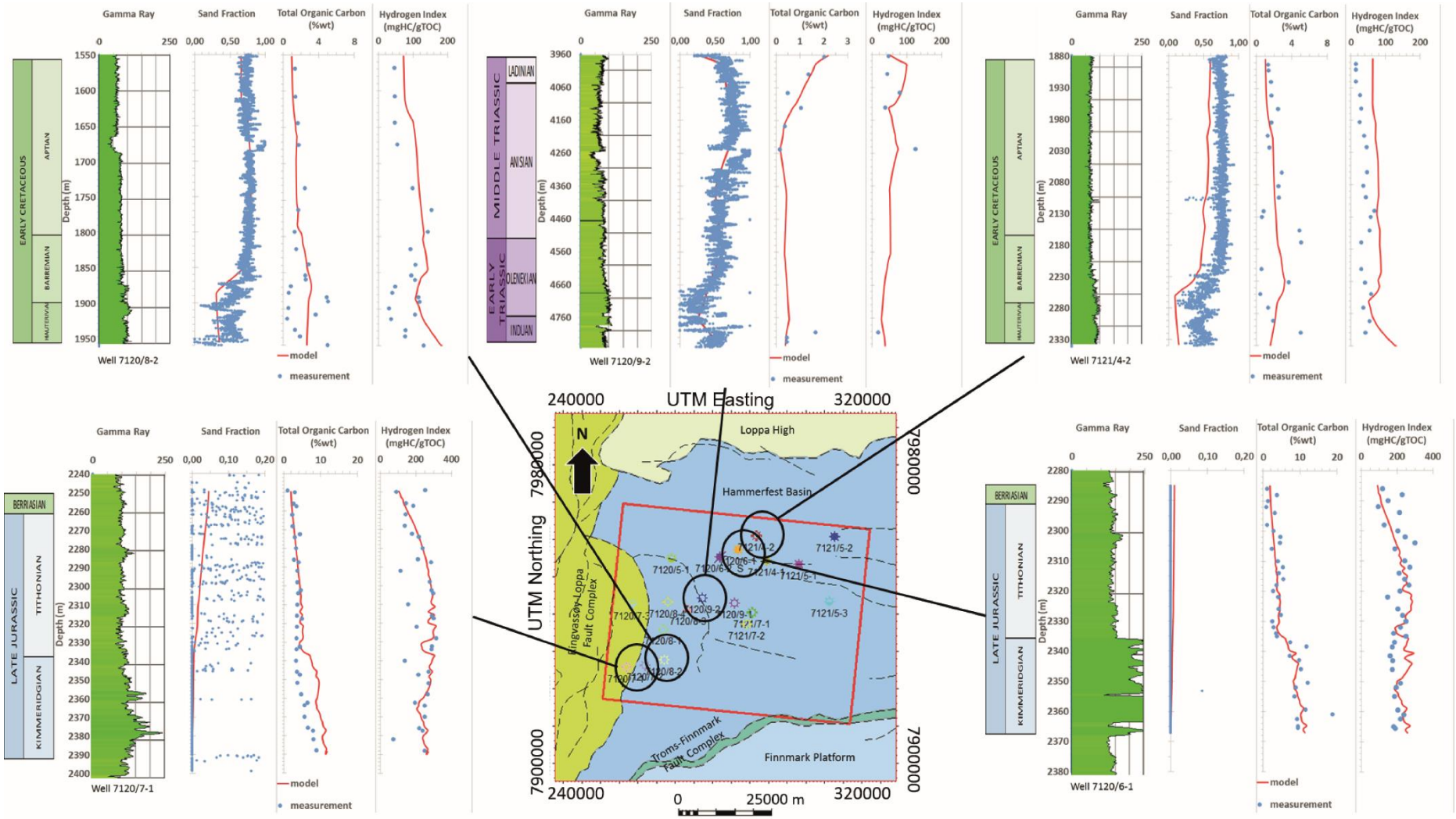

Figure 31. Validation results of five wells for the three source rock intervals in the study area: the Early-Mid Triassic Interval (well 7120/9-2), the Late Jurassic Interval (well 7120/6-1 and 7120/7-1), and the Early Cretaceous Interval (well 7120/9-2 and 7121/4-2). There are relatively good matches between measured and modelled data. In comparison to the Late Jurassic and Early Cretaceous Intervals, the Early-Mid Triassic Interval shows a poor geochemical data coverage.

4.1 Early-Mid Triassic Interval

4.1.1 Results

The results of the paleo-bathymetry reconstructions and the inorganic facies modelling of the Early-Mid Triassic Interval (251-240 Ma) are shown in **Figure 32** and **Table 6**. Based on the results, the Early-Mid Triassic is dominated by lower bathyal bathymetries (mean water depth of 1191 ± 289 m) with shelf depositional environment as shown by the PWD histogram of the interval and the PWD map of the top Early-Mid Triassic Interval respectively (**Figure 32**). Laterally, the bathymetry of the top Early-Mid Triassic Interval is deepening from the east to the west in the study area as shown by the changing of sedimentary facies from shallow-shelf and shelf environment to deep-shelf environment, separated by the NE-SW trending sedimentary facies boundary in the east and the N-S striking, west-dipping normal fault in the west (**Figure 32**). The N-S striking, west-dipping normal faults in the west separate the shallow-shelf – shelf facies of the HB with the deep-shelf facies of the Ringvassøy-Loppa Fault Complex (RLFC) (**Figure 1**). In the HB part, the PWD gradually deepens from 400 m to 900 m before a sharp deepening in the RLFC from 900 m to 1700 m (**Figure 32**). A northwest trending deep-shelf environment of the paleo-Loppa High (**Figure 1**) is found in the northwestern part of the basin (**Figure 32**). Within the interval, there is a shallowing trend of mean water depth from lower bathyal zone of 1416 ± 187 m during 251-247 Ma and 1130 ± 179 m during 247-243 Ma to middle bathyal zone of 881 ± 182 m during 243-240 Ma (**Table 6**).

During the Early-Mid Triassic, there is a gradual coarsening upward deposition of the sand-shale sediments from 251-247 Ma with the SF of 0.42 ± 0.11 to 247-243 Ma and 243-240 Ma with the SF of 0.57 ± 0.09 and 0.67 ± 0.13 respectively (**Table 6**). Laterally, the sandy deposit distributes mainly on the basin proximal area while the shaly sediment is predominantly deposited on the basin distal area during the Early-Mid Triassic (**Figure 33**). On the basin proximal area, the sandy deposit is getting coarser toward the southeast as illustrated by an increase of SF; indicating the sediment is supplied from the southeast during the Early-Mid Triassic (northwestward sedimentation). Additionally, during 243-240 Ma, supplementary sources supply sediments from the west and north of the basin as indicated by local sandy deposit distribution (**Figure 33**).

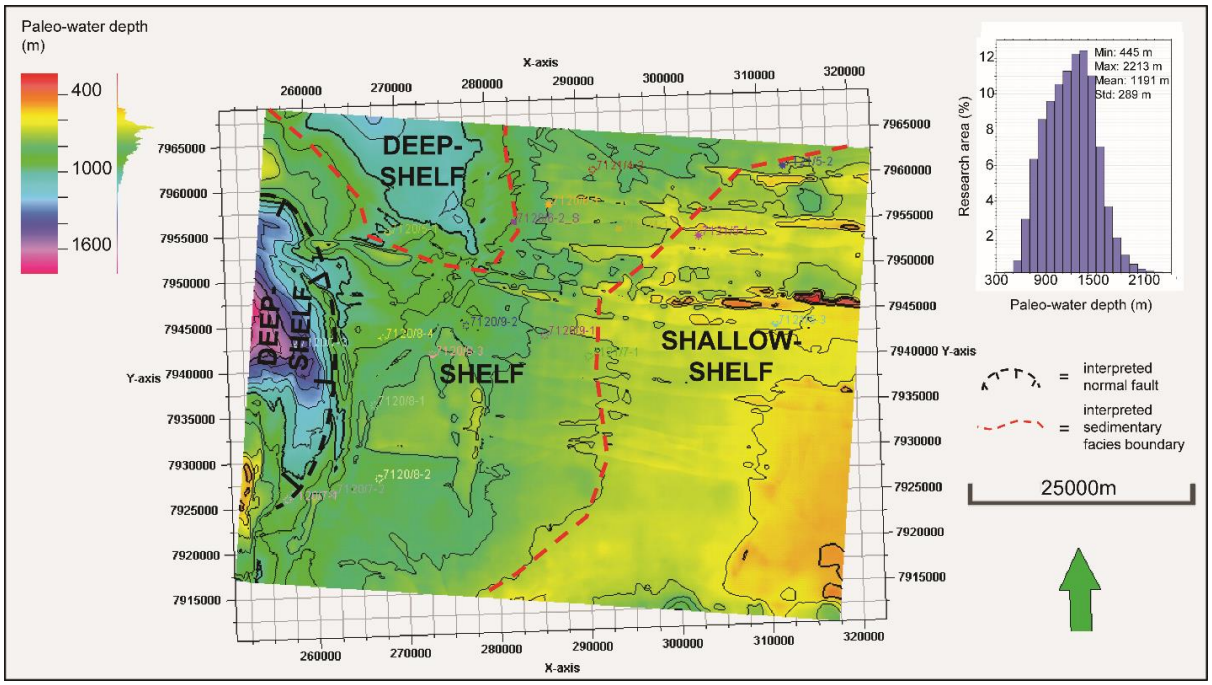

Figure 32. The interpreted paleo-water depth (PWD) map of the top Early-Mid Triassic Interval (240 Ma) with the histogram of water depth values during the Early-Mid Triassic (251-240 Ma).

Table 6. Results of the inorganic facies modelling for the Early-Mid Triassic Interval.

Inorganic facies	Formation	Age (Ma)	Min	Max	Mean	Std
Paleo-water depth (m)	Kobbe Fm	243-240	445	1773	881	182
	Steinkobbe Fm	247-243	679	1943	1130	179
	Havert-Klappmyss Fms	251-247	902	2214	1416	187
Sedimentation rate (cm/ka)	Kobbe Fm	243-240	0.4	60	21	7
	Steinkobbe Fm	247-243	0.4	41	20	5
	Havert-Klappmyss Fms	251-247	0.5	314	48	34
Sand fraction	Kobbe Fm	243-240	0.16	0.93	0.67	0.13
	Steinkobbe Fm	247-243	0.40	0.86	0.57	0.09
	Havert-Klappmyss Fms	251-247	0.15	0.60	0.42	0.11
Dry bulk density (g/cm^3)	Kobbe Fm	243-240	0.79	1.30	1.13	0.08
	Steinkobbe Fm	247-243	0.95	1.26	1.06	0.06
	Havert-Klappmyss Fms	251-247	0.78	1.08	0.96	0.08

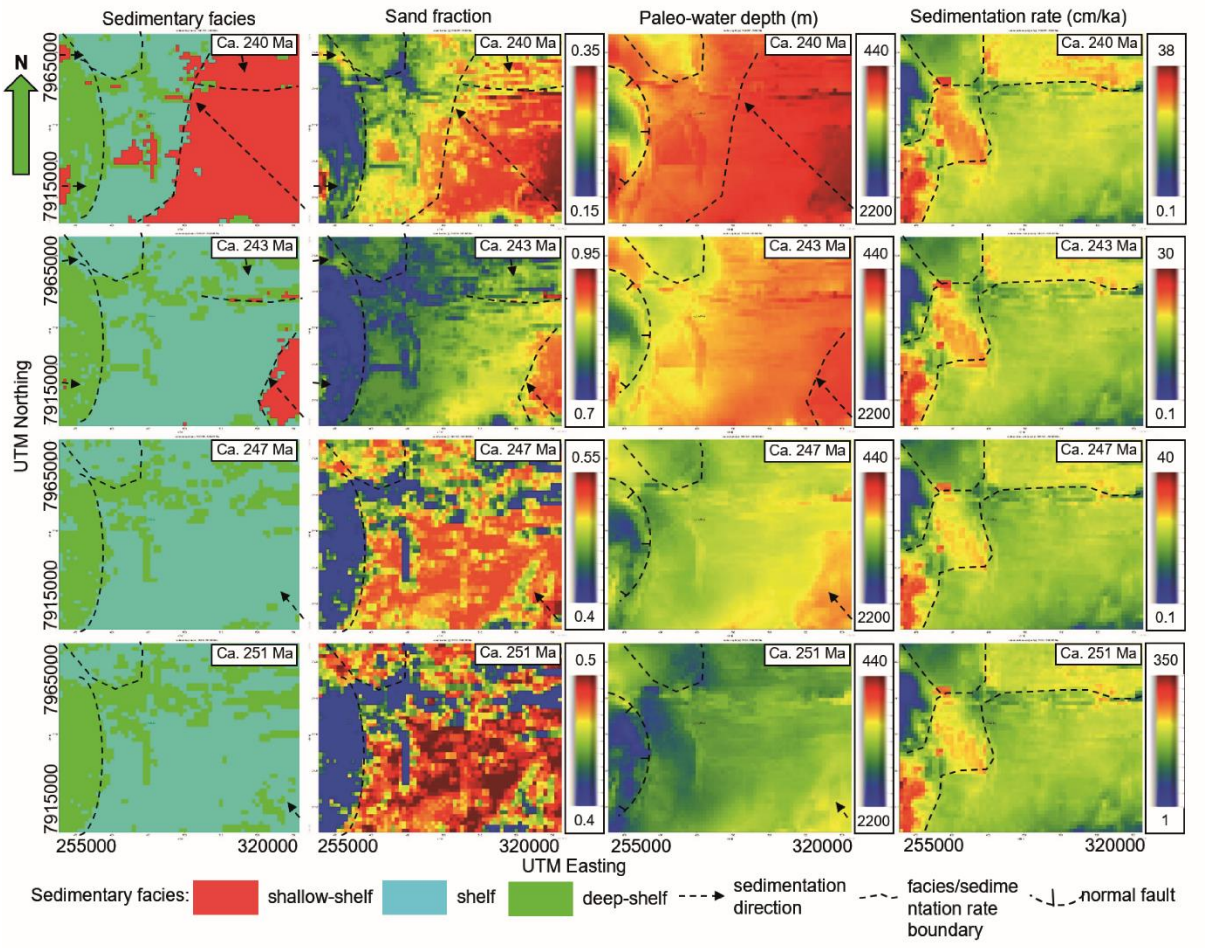

Figure 33. The interpreted 2D maps of the inorganic facies modelling results of the Early-Mid Triassic Interval through certain time periods within the interval. Note that not all of the facies use the same scale. Instead, due to the different range of facies values between particular time-slices, auto-scale is sometimes preferred to visualize the lateral distribution.

The Early-Mid Triassic is dominated by a fast-very fast sedimentation rate in the study area, reaching 314 ± 34 cm/ka at 251 Ma (**Figure 33**). The mean sedimentation rate is 48 ± 34 cm/ka during 251-243 Ma (**Table 6**). Following, sedimentation slows down and is rather stable with the rate of 20 ± 5 cm/ka and 21 ± 7 cm/ka at 247-243 Ma and 243-240 Ma respectively (**Table 6**). Spatially, the working area can be separated into NE-SW trending area subjected to fast sedimentation rate (20-40 cm/ka), intermediate sedimentation rate of 15-20 cm/ka in the southern part of the shallow-shelf – shelf area, and the area with very slow-slow sedimentation rate of 0.1-10 cm/ka in the northwestern deep-shelf area (**Figure 33**). The distribution of the sedimentation rate relates to the northwestward sedimentation as well as multiple sediment sources encountered during the Early-Mid Triassic including the southeast, the north and the west of the basin. In southwestern-most part of the basin, very fast sedimentation rate is probably induced by turbidite toward the deep-shelf from the northwestward sedimentation and an additional local source from the west (**Figure 33**). In addition, the fast sedimentation rate in

the northeast area is caused by an additional local sediment source from the north. The very-slow – slow sedimentation rate in in the northern part of the west deep-shelf as well as the northwest deep-shelf, indicates the remoteness of these areas from the main sediment source of the basin (**Figure 33**).

During the Early-Mid Triassic, the dry bulk density (DBD) is gradually increasing from 0.96 ± 0.07 g/cm^3 at 251-247 Ma to 1.06 ± 0.06 g/cm^3 at 247-243 Ma and 1.13 ± 0.08 g/cm^3 at 243-240 Ma (**Table 6**). The gradual increment of the DBD is well-correlated to the SF content increment, indicating a coarsening upward trend as more sandy sediment is progressively filling the basin during the Early-Mid Triassic. In general, the DBD is distributed according to the SF distribution in the basin (**Table 6**).

During the Early-Mid Triassic, the primary productivity is generally very low generally as indicated by the mean values of 0.08 ± 0.11 gC/m^2/a in the 251-247 Ma, 0.52 ± 0.17 gC/m^2/a in the 247-243 Ma, and 2.55 ± 1.78 gC/m^2/a in the 243-240 Ma (**Table 7**). This affects the distribution of almost no marine organic matter (MOM) within the total amount of organic content in the Early-Mid Triassic source rocks (**Table 7**). The organic contents are more related to the terrigenous organic carbon (C_{terr}) and the residual organic carbon (C_{res}) as a result of more sediments filling the basin during the Early-Mid Triassic. In general, the amount of both C_{terr} and C_{res} in the Early-Mid Triassic is poor quantity as indicated by their mean value trend through time. The C_{terr} varies from 0.01-0.74 wt% and the C_{res} are between 0.09-2.09 wt% during the Early-Mid Triassic (**Table 7**). These affect the distribution of a poor quantity of the TOC as indicated by the mean TOC values of 0.45 ± 0.06 wt% during 251-247 Ma and 0.33 ± 0.10 wt% during 247-243 Ma (**Table 7**). An exception is for the period of 243-240 Ma as it shows a good quantity of the mean TOC, 1.02 ± 0.54 wt% (**Table 7**) and a very good quantity of TOC, 2-2.32 ± 0.54 wt% at the 240 Ma especially in the deep-shelf area in the RLFC part of the basin (**Figure 34**).

Regarding the source rock quality and the kerogen type, the Early-Mid Triassic Interval is dominated by a very low – low hydrogen (**Table 7**). In the lower interval (251-247 Ma) the mean HI value is very low, 38 ± 9 mgHC/gTOC. Differently, the middle (247-243 Ma) and upper intervals (243-240 Ma) respectively show low mean HI values of 57 ± 10 mgHC/gTOC and 76 ± 20 mgHC/gTOC (**Table 7**).

Table 7. The results of the organic facies modelling results of the Early-Mid Triassic Interval.

Organic facies	Formation	Age (Ma)	Min	Max	Mean	Std
Primary productivity ($gC/m^2/a$)	Kobbe Fm	243-240	0.47	7.90	2.55	1.78
	Steinkobbe Fm	247-243	0.32	0.93	0.52	0.17
	Havert-Klappmyss Fms	251-247	0.01	0.71	0.08	0.11
Marine organic matter (wt%)	Kobbe Fm	243-240	0	0.02	0	0
	Steinkobbe Fm	247-243	0	0	0	0
	Havert-Klappmyss Fms	251-247	0	0	0	0
Residual organic carbon (wt%)	Kobbe Fm	243-240	0.09	2.09	0.71	0.38
	Steinkobbe Fm	247-243	0.09	0.44	0.28	0.09
	Havert-Klappmyss Fms	251-247	0.29	0.60	0.42	0.08
Terrigenous organic carbon (wt%)	Kobbe Fm	243-240	0.02	0.74	0.31	0.21
	Steinkobbe Fm	247-243	0.04	0.07	0.06	0.01
	Havert-Klappmyss Fms	251-247	0.01	0.07	0.04	0.02
Total organic carbon (wt%)	Kobbe Fm	243-240	0.11	2.32	1.02	0.54
	Steinkobbe Fm	247-243	0.13	0.50	0.33	0.10
	Havert-Klappmyss Fms	251-247	0.35	0.61	0.45	0.06
Hydrogen index (mgHC /gTOC)	Kobbe Fm	243-240	38	122	76	20
	Steinkobbe Fm	247-243	41	88	57	10
	Havert-Klappmyss Fms	251-247	24	54	38	9

Laterally, the organic facies are similarly distributed according to the basin-fill deposition during the Early-Mid Triassic as illustrated in **Figure 34**. The TOC is distributed following the pattern of the C_{res} distribution. The amount of TOC, as well as C_{res}, through time is lower in the shallow-shelf area of the HB part (0.1–2.1 wt% and 0.1-1.7 wt% respectively) and progressively increasing toward the northwest before a sharp increase in the west at the deep-shelf area of the RLFC (0.4-2.3 wt% and 0.33-2 wt% respectively) (**Figure 34**). On the contrary, higher HI values are mainly dispersed in the shallow-shelf and shelf of the HB part (35-69 mgHC/gTOC), gradually decreasing northwestward with sudden drop in the west at the deep-shelf the RLFC (32-52 mgHC/gTOC) (**Figure 34**). The C_{terr}, on the other hand, has generally different patterns for the lower interval and the upper interval. In the lower interval, the distribution of the C_{terr} is similar with the HI distribution, which is higher in the shelf area of the HB part (0.03-0.07 wt%) than the deep-shelf of the RLFC (0.02-0.05 wt%). In the upper interval, the C_{terr} is low in the shallow-shelf of the HB part (0.02-0.25 wt%) and gradually increasing toward the northwest (0.06-0.35 wt%) and RLFC (0.06-0.45 wt%) as the main accumulation of higher C_{terr} (**Figure 34**).

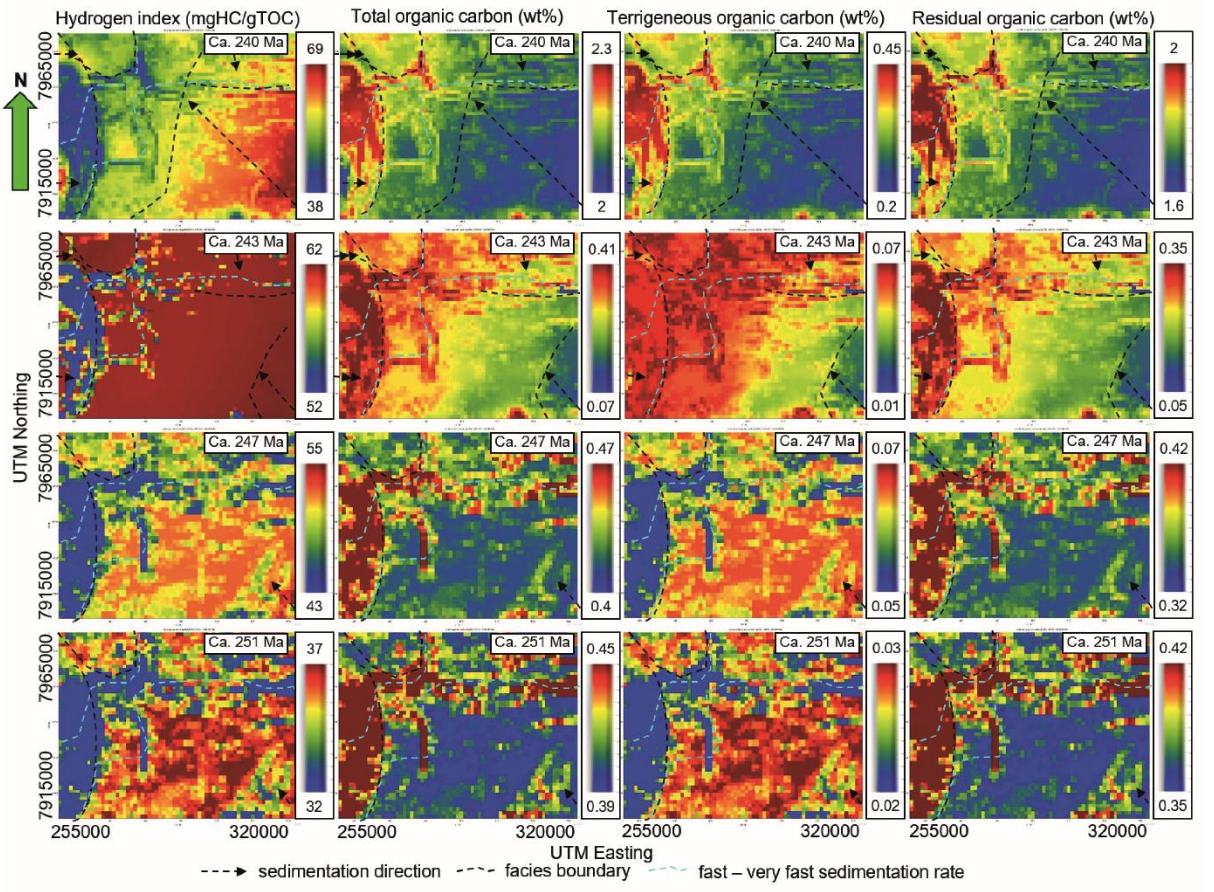

Figure 34. The interpreted 2D maps of the organic facies modelling results of the Early-Mid Triassic Interval through certain time periods within the interval. Note that not all of the facies use the same scale. Instead, due to the different range of facies values between particular time-slices, auto-scale is sometimes preferred to visualize the lateral distribution.

4.1.2 Interpretations

Based on the results, the Early-Mid Triassic is a period of deep PWD that possesses large accommodation space for a great amount of sediment deposition (**Figure 33**). Lower bathyal bathymetry zone of 1400–1100 m (**Table 6** and **Figure 33**) dominates the Early Triassic as a result of the regional subsidence in the Barents Sea (Faleide et al., 2008; Gabrielsen et al., 1990; Larssen et al., 2002). The subsidence was triggered by the Late Permian-Early Triassic rifting (Doré, 1991; Gudlaugsson et al., 1998; Johansen et al., 1994; Wood et al., 1989; Ziegler, 1988), correlated with deepening of the rift from a shallow-water to a deep-water environment.

Generally, the Early-Mid Triassic has a shallowing upward trend of water depth (**Figure 35**), which contradicts the global eustatic sea-level rise during the Early-Mid Triassic by Haq et al. (1987). Since the HB has an intracratonic setting and has been affected by several tectonic phase including the regional subsidence in the Late Permian-Early Triassic, the development of middle-lower bathyal PWD (700-1400 m, **Figure 35**) during the Early-Mid Triassic is out of

scale of the global eustatic sea-level change (± 30 m (Haq et al., 1987)). The shallowing upward trend of the PWD in the study area is also controlled by the high input of the sediments with fast-very fast sedimentation rate (20-175 cm/ka) to the basin throughout the Early-Mid Triassic (**Figure 35**). This affects the development of the shallow-shelf facies, which is well-correlated with higher SF and shallower PWD distribution in the basin (**Figure 33**) and indicate that the sediment influx outpaces the rise of the sea level, creating a shallowing upward trend of PWD in the study area. The fast-very fast sedimentation rate may also have outpaced the subsidence rate generally, coupling the effects to the shallowing PWD upward in the study area.

The fast-very fast sedimentation rate during ca.251-249 Ma (**Figure 35**), with maximum sedimentation rate of ca. 313 cm/ka in the RLFC part of the study area (**Table 6** and **Figure 33**), correspondingly marks the Early Triassic as a transition to clastic deposition from shallow-water carbonate environment (Faleide et al., 2008; Gabrielsen et al., 1990; Glørstad-Clark et al., 2010). Based on the SF distribution (**Figure 33**), the clastic input largely sources from the southeast of the basin as a result of uplift and erosion in the southeast of the basin (Jacobsen and van Veen, 1984; Johansen et al., 1993; Larssen et al., 2002; Riis et al., 2008; Skjold et al., 1998; Van Veen et al., 1993). The sedimentation remains stable at the fast rate throughout the Early-Mid Triassic following the very fast sedimentation rate during the Early Triassic (**Figure 35**) and delivering thick Early-Mid Triassic siliciclastic deposits (800-1400 m) with a coarsening upward trend in the basin (**Figure 36**).

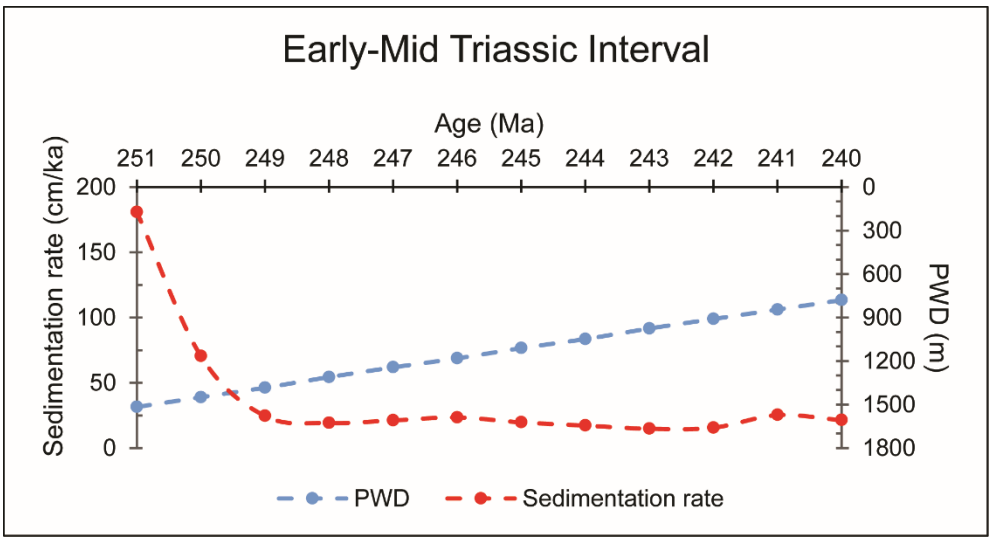

Figure 35. Mean paleo-water depth and mean sedimentation rate change through time during the Early-Mid Triassic. The sedimentation rate curve shows a very fast sedimentation rate during 251-249 Ma

prior to remaining stable at the fast rate until 240 Ma. The paleo-water depth (PWD) curve shows a shallowing trend throughout the Early-Mid Triassic.

The SF distribution shows that sandy sediments are deposited northwestwardly especially during 243-240 Ma (**Figure 33**). The paleo-bathymetry at the same period similarly shows landward shallowing as indicated by the development of the shallow-shelf facies along the northwestward deepening trend of the PWD (**Figure 33**). These may imply basinward shoreline trajectory approximately from the southeast of the basin, where the sediment supply mainly comes from, shifting further northwestward infilling the basin with more sandy sediments with time. This supports the interpretation of progradation (**Figure 37**) primarily from the east and southeast of the basin toward the west-northwest in the open-shelf environment (Glørstad-Clark et al., 2010; Høy and Lundschien, 2011; Riis et al., 2008) with limited input from the north (Glørstad-Clark et al., 2011; Høy and Lundschien, 2011). The progradation of sediment is also well indicated in the Early-Mid Triassic Interval cross-section (**Figure 36**) as a coarsening upward trend with laterally decreasing sand sediment trend from the east (SF 0.75-0.9) to the west (SF ca. 0.75).

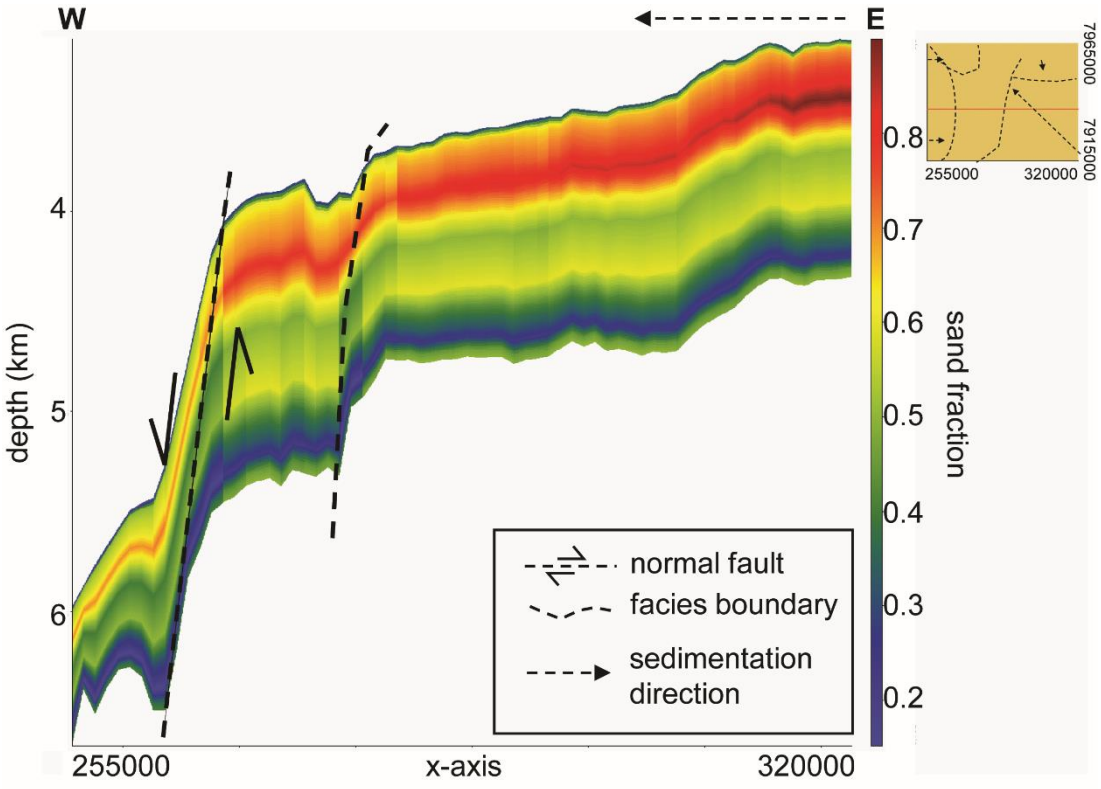

Figure 36. An East-West cross-section of the thick Early-Mid Triassic siliciclastic deposit. A coarsening upward trend as well as laterally decreasing of sand fraction trend toward the west are well illustrated. The west dipping normal fault in the west separate the HB part from the RLFC part of the study area.

Rift sequence stratigraphic pattern

The progradation of sediment consisting of shale and sandy shale (SF 0.15-0.50) in the lower interval, overlain by sandy shale, shaly sand and sand (SF 0.40-0.86) in the middle interval and shaly sand and sand (SF 0.67-0.93) with minor shale (SF ca. 0.16) at the top of the sequence in the upper interval (**Table 6**). The coarsening upward sequence is formed by the three depositional phases which are under-filled, filled, and over-filled upward (Martins-Neto and Catuneanu, 2010) as a consequence of the volume balance between sediment supply and accomodation space (**Figure 37**). During the Early-Mid Triassic, each phase is represented by the deposition of the Havert-Klappmyss Fms, Steinkobbe Fm, and Kobbe Fm respectively according to their process stratigraphy characteristics.

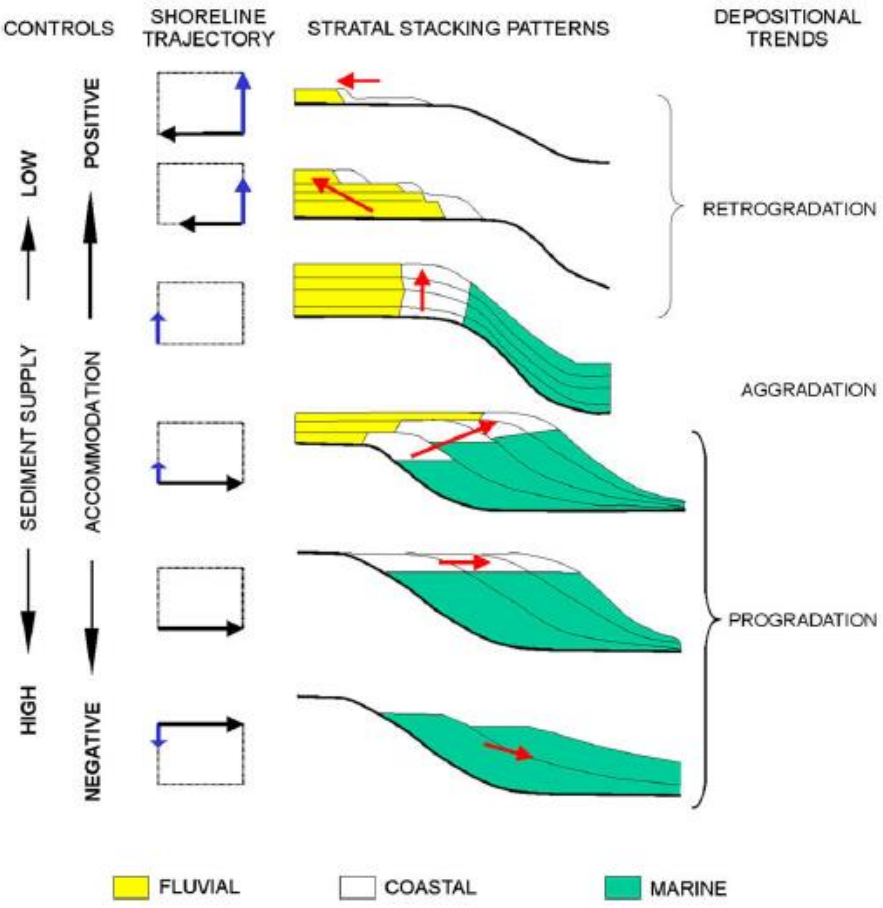

Figure 37. Depositional trends pattern as a result of different shoreline trajectory, process stratigraphy and volume balance between sediment supply and accommodation space (Martins-Neto and Catuneanu, 2010).

The first phase, which was the deposition of the Havert-Klappmyss Fms, took place during the Induan-Olenekian (251-247 Ma) (Glørstad-Clark et al., 2010), marked by a thin sandy shale deposit with SF ca. 0.5, overlain by shale (SF 0.15-0.25) and coarsening upward trend of sandy-shale (SF 0.25-0.5) (**Figure 36**). This phase has generally high accommodation

space as indicated by lower-middle bathyal bathymetry (mean PWD 1416 ± 187 m) which was primarily formed due to regional subsidence in the Barents Sea (Faleide et al., 2008; Gabrielsen et al., 1990; Larssen et al., 2002). The lowermost sandy shale is interpreted as a maximum flooding surface, marking the Late Permian-Early Triassic boundary (Glørstad-Clark et al., 2010). Even though the sedimentation rate is very fast (mean sedimentation rate 48 ± 34 cm/ka) (**Table 6**) during the Induan-Olenekian, the sediment supply is not able to exceed the high accommodation space, created by the regional subsidence. Besides, the shale and sandy shale dominated sediment (**Figure 33**) in this sequence infers the long distance of the basin from the landward shoreline during the Induan-Olenekian (Glørstad-Clark et al., 2010), thus supporting the underfilled phase (Martins-Neto and Catuneanu, 2010) during the Induan-Olenekian (**Figure 38**).

The second phase, which was the deposition of the Steinkobbe Fm, occurred during the Anisian (247-243 Ma) (Glørstad-Clark et al., 2010). This sequence consists of a generally coarsening upward trend of sandy shale – sand sediments (SF 0.40-0.86) (**Figure 36**) and lower accommodation space than the underlying sequence as indicated by a lower-middle bathyal bathymetry (mean PWD 1130 ± 179 m) (**Table 6**). However, the HB part is shallowing faster than the RLFC part during this period (**Figure 33**). The HB part has PWD of 680-1200 m (**Figure 33**). Even though the sedimentation rate is slower than in the first phase (mean sedimentation rate 20 ± 5 cm/ka) (**Table 6**), the sediment supply is able to fill the generated accommodation space as indicated by the thickness of the sequence (600-800 m) which is more or less balanced with the PWD (**Figure 36)**. Besides, as more shaly sand and sand sediments filled this sequence, especially in the proximal HB part, it infers the proximity of the basin from the basinward shoreline (Glørstad-Clark et al., 2010). This supports the filled phase (Martins-Neto and Catuneanu, 2010) during the Anisian (**Figure 38**), especially in the proximal HB part, while the RLFC part remains in an underfilled phase.

The last phase, which was the deposition of the Kobbe Fm, occurred during Anisian-early Ladinian (243-240 Ma) (Glørstad-Clark et al., 2010). This sequence consists of a generally coarsening upward trend of shaly sand – sand sediments (SF 0.70-93) with minor shale – sandy shale sediments (SF 0.16-0.50) at the top of the sequence (**Figure 36**). Following the shallowing trend of water depth during the Early-Mid Triassic (**Figure 35**), this sequence has the shallowest water depth in comparison with the two underlying sequences, as indicated by the middle bathyal bathymetry zone (mean PWD 881 ± 182 m) (**Table 6**). During this period, the development of the shallow-shelf facies in the HB part is faster than before, as a result of more

basinward progradation of sandy sediments and shallowing PWD (445-900 m) (**Figure 33**). The sedimentation rate is slight faster than the second phase (mean sedimentation rate 21 ± 7 cm/ka) (**Table 6**) and the sedimentation is able to surpass the decrease of accommodation volume as indicated by the thickness of the sequence (500-700 m) (**Figure 36**). Besides, as more sandy sediments filled this sequence, especially in the shallow-shelf facies in the proximal HB part, it infers the more proximity distance of the basin from the basinward shoreline during the Anisian-early Ladinian and considered as the maximum progradation of the system (Glørstad-Clark et al., 2010). This supporting the overfilled phase (Martins-Neto and Catuneanu, 2010) during the Anisian-early Ladinian (**Figure 38**), especially in the shallow-shelf facies in the proximal HB part, with maximum progradation of sediments (**Figure 33**). The RLFC part remains in an underfilled phase. During this period, the deep-shelf of the paleo-Loppa High starts emerging (Glørstad-Clark et al., 2010) as indicated by a fast shallowing of PWD from ca. 1200 m to ca. 700 m (**Figure 33**).

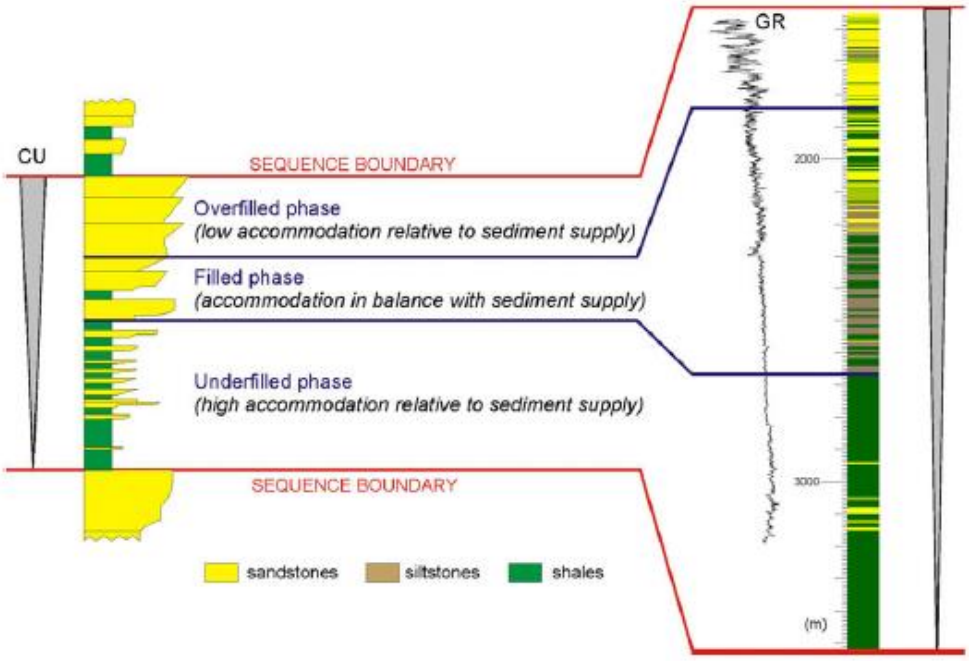

Figure 38. Rift sequence internal architecture with general coarsening upward trend (Martins-Neto and Catuneanu, 2010).

Deposition of the sequences with some phases involved in the overall coarsening upward trend (**Figure 38**) during the Early-Mid Triassic Interval is in an agreement with the rift-sequence stratigraphy pattern from Martins-Neto and Catuneanu (2010). This is also supported by the thickness variation in the Early-Mid Triassic Interval (**Figure 36**) (Anell et al., 2013). The Havert-Klappmyss Fms shale is thickening eastward to the RLFC part while the Steinkobbe Fm and the Kobbe Fm is thickening westward to the shoreline of the study area (**Figure 36**)

(Glørstad-Clark et al., 2010). These thickness variations may indicate syn-sedimentary deposition (Anell et al., 2013) even though the rifting evidence is not clear in the study area since the younger tectonic activities and burial by thick younger stratigraphic units overprinted it (Faleide et al., 2008; Gudlaugsson et al., 1998). Probably, it has been affected by rifting further north in the Barents Sea (Anell et al., 2013; Faleide et al., 2008; Surlyk, 1990). Additionally, the Early-Mid Triassic Interval is bounded by sandy shale sediment, which is in accordance to the maximum flooding surfaces in the Barents Sea (Glørstad-Clark et al., 2010).

Organic matter source types

Based on the results (**Table 7** and **Figure 34**), the organic facies distribute according to the basin-fill deposition during the Early-Mid Triassic. The Early-Mid Triassic Interval is more terrestrially-sourced in terms of organic matter (allochthonous) with a generally poor-fair quantity of the C_{terr} (0.01-0.74 wt%) and poor-very good quantity of the C_{res} (0.09-2.09 wt%) (**Table 7**). Very low primary productivity (0.01-7.90 $gC/m^2/a$) (**Table 7**) and high input of the sand-shale sediments (SF 0.15-0.93) (**Table 6**) with fast-very fast sedimentation rates (mean sedimentation rate 20-175 cm/ka) (**Figure 35**) are the main factors causing the organic matter within the source rock to be more allochthonous during the Early-Mid Triassic. Due to the regional subsidence toward deep-water environment during Early Triassic (Faleide et al., 2008; Gabrielsen et al., 1990; Glørstad-Clark et al., 2010; Larssen et al., 2002), the lower bathyal PWD (1400-1100 m) (**Table 6** and **Figure 33**) reduced the carbon flux (**Eq.** (12)). Most of the MOM fraction, produced by the PP, has already experienced degradation in the uppermost water-column during the settling throughout the Early-Mid Triassic.

The C_{terr} is not produced in situ and rather enters the basin through sedimentation, originated from the continent (Mann and Zweigel, 2009). The correlation between the C_{terr} and sedimentation throughout the Early-Mid Triassic is also indicated in the lateral distribution maps. Generally, the C_{terr} (**Figure 34**) distributes according to the SF distribution (**Figure 33**), following the main northwestward sedimentation trend in the basin. During 251-247 Ma, the main accumulation of the C_{terr} is in the shelf area where the higher SF is deposited while during the period of 243-241 Ma, the distribution of the C_{terr} is inversely proportional to the SF distribution (**Figure 33** and **Figure** 34). However, the C_{terr} is not always necessarily associated with pure sand, it can be the other way around since the winnowing of the lower density organic particles may occur in a highly energetic hydrodynamic regime (Mann and Zweigel, 2009). This is related to turbidite that may occur in the deep-shelf area of the basin during the maximum progradation (243-241 Ma), transporting the C_{terr} further into the basin deep-shelf

area in the west. During the maximum progradation period, C_{terr} amounts are increasing northwestward (**Figure 34**), following the progradation direction in the basin (**Figure 33**). Since the C_{terr} distribution is related to the sedimentation and SF distribution, the organic matter is interpreted to originate from a fluvial or deltaic system of the continental facies in the sediment source area (Glørstad-Clark et al., 2010). During the Early-Mid Triassic, the main sediment source was in the southeast of the basin (Jacobsen and van Veen, 1984; Johansen et al., 1993; Larssen et al., 2002; Riis et al., 2008; Skjold et al., 1998; Van Veen et al., 1993). Since the organic matter is mainly sourced from the continental facies, the C_{terr} is mainly derived from the land plant, which most likely signify type III kerogen (vitrinite) and therefore the HI values are relatively low (24-122 mgHC/gTOC) during the Early-Mid Triassic (**Table 7**).

Contradictorily, the C_{res} is distributed (**Figure 34**) following the shaly sediments distribution (**Figure 33**), mainly in the RLFC part of the study area. This may suggest that the C_{res} is mainly sourced from the degradation of the C_{terr}, caused by relatively long sediment transport from the coastline towards the basin deep-shelf. Due to degradation process, the C_{res} mainly consist of type IV kerogen (vitrinite). Thus, the main organic matter source type during the Early-Mid Triassic is land-derived and the source rock distribution will depend on the distribution of the C_{terr} and C_{res}.

The poor quantity of the C_{terr} and C_{res} is probably related to the uplift and erosion of the source areas. Due to the uplift and erosion, the C_{terr} has been eroded and degraded already in the source area, reducing the quantity of the C_{terr} in the basin fill. Another factor is the shoreline trajectory during the Early-Mid Triassic. Since the shoreline was further landward in the Early Triassic, the amount of the transported C_{terr} into the basin was low due to the degradation during the sediment transport. This is shown by the general increase of the organic matter quantity toward the maximum progradation period when the shoreline is further shifted basinward (**Figure 34**).

Preservation conditions

Because the organic matter of the Early-Mid Triassic Interval is terrestrially-sourced, the preservation of the C_{terr} mainly depends on the sediment transport and sorting (Mann and Zweigel, 2009). Generally, since the C_{terr} has already experienced some degradation processes due to sediment transport from the source to sink, it may cause C_{terr} to be more resistant from further degradation in the basin (Hedges and Keil, 1995) which is good for potential organic matter preservation. Based on the lateral distribution of the C_{terr} and C_{res} shown in **Figure 34**, the ratio of C_{res}/C_{terr}, which is approximately equal to the ratio of inertinite/vitrinite, increased

toward the deep-shelf area in the basin except during the period of the maximum progradation throughout the Early-Mid Triassic (**Figure 34**). Lower inertinite/vitrinite ratios of the organic matter are mainly found in the HB part. This high inertinite/vitrinite ratio of organic matter in the basin slope may indicate higher degree of chemical degradation (Littke et al., 1997), reducing the source rock quality potential there. However, during the period of the maximum progradation, since turbidite can transport C_{terr} further into the RLFC part, a lower ratio of C_{res}/C_{terr} can also be found in the RLFC part of the study area (**Figure 34**).

During the Early-Mid Triassic, the coarsening upward trend of the sediments affects the transition to more C_{terr} content and relatively low HI values due to dilution effects and poor preservation. Furthermore, the sedimentation rate may also control the preservation condition. Fast-very fast sedimentation rates may indicate that the organic matter is deposited under oxic conditions (Allen and Allen, 2013) throughout the Early-Mid Triassic. In the Early-Mid Triassic Interval, the oxic conditions are also indicated by its poor quantity (TOC) as well as low quality (HI) of the organic matter (**Table 7**). The oxic conditions are coupled with the effects of poorer preservation during the Early-Mid Triassic and result in generally poor quantity and quality of organic matter. The fast-very fast sedimentation rates throughout the Early-Mid Triassic decrease the quantity and quality of the organic matter due to the dilution effect. The decrease of the sedimentation rate in the Early Triassic (**Figure 35**) increases the preservation of the organic matter afterward as indicated by slight increase of the organic matter upward (**Figure 34**). Laterally, based on the increase of organic matter accumulation toward the deep-shelf (**Figure 34**), preservation conditions are probably also increased following this distribution. The increase of preservation conditions toward the deeper area in the shelf environment are typical for a rift setting (Watts, 2012). This is in accordance with the interpretation of the basin-fill process of the Early-Mid Triassic Interval.

Source rock potential and distribution

In general, the Early-Mid Triassic Interval has poor source rock potential (**Figure 39**). Source rocks are distributed according to the basin-fill process especially the sedimentation in the basin. Laterally, the main accumulation of the TOC during the Early-Mid Triassic is in the RLFC part (TOC 0.4-2.3 wt%), reducing gradually toward the southeast to the source area (TOC 0.07-2 wt%) (**Figure 34**). On the other hand, the main accumulations of higher quality source rocks are in the HB part, decreasing northwestward following the sedimentation direction from the shallow-shelf area to the deep-shelf area. The RLFC part is the main

accumulation of the TOC and has the lowest source rock quality during the Early-Mid Triassic (**Figure 34**).

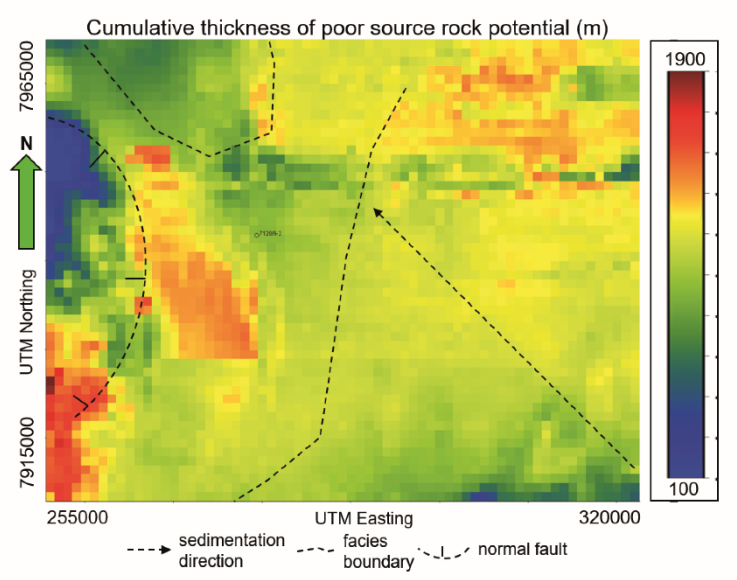

Figure 39. Cumulative thickness of the source rock potential distribution of the Early-Mid Triassic Interval.

Vertically, the best source rock potential in the Early-Mid Triassic Interval is within the Kobbe Fm (243-240 Ma). This is shown by the accumulation of higher quantity and quality in this interval in comparison to the underlying units. The TOC is gradually increasing upward from ca. 1 wt% to ca. 2.3 wt%, with the highest TOC accumulated in the uppermost shale unit (**Figure 40**). Variously, the HI increases upward from ca. 80 mgHC/gTOC to ca. 120 mgHC/gTOC in the sandy unit, before a sharp decrease in the uppermost shale unit (HI 60-90 mgHC/gTOC) (**Figure 40**).

The Kobbe Fm has a more favourable setting for the source rock potential due to shallower PWD, proximity to the shoreline, and slower sedimentation rate as compared to the two underlying units during the Early-Mid Triassic. However, since the organic matter quantity and quality and the preservation conditions are generally low, the Early-Mid Triassic Interval has poor source rock potential in the study area. Additionally, as the source rock is constituted from type III (vitrinite) and type IV (vitrinite) kerogen with poor quantity, it has the potential to either generate small amounts of gas or generate no hydrocarbons at all.

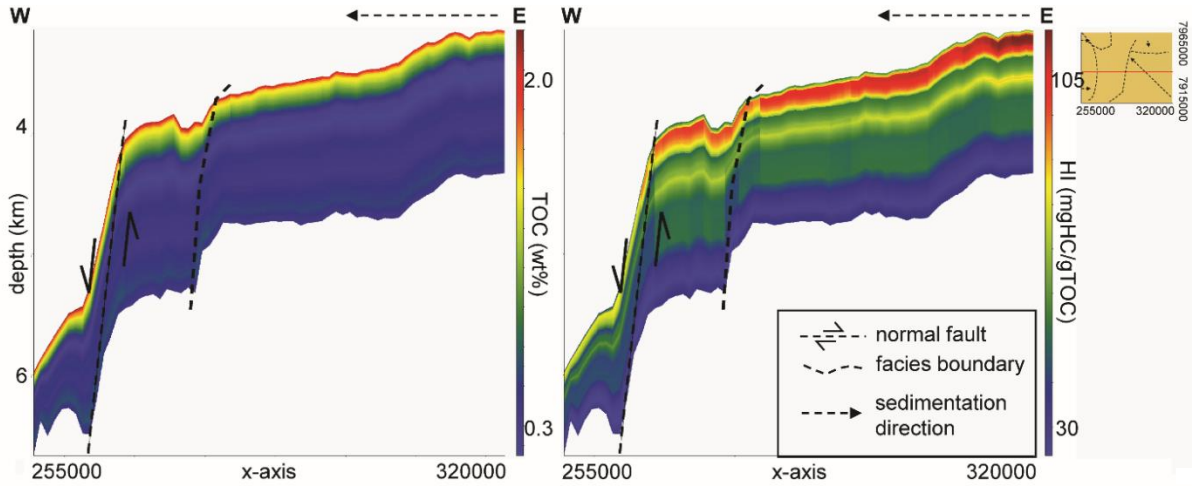

Figure 40. An east-west cross section of the TOC and HI accumulation for the Early-Mid Triassic Interval. Vertically, the best source rock potential accumulates in the uppermost (the Kobbe Fm) interval. Laterally, the higher HI values accumulate in the eastern part of the basin. Generally, it has poor source rock potential within the whole interval.

4.2 Late Jurassic Interval

4.2.1 Results

The results of the paleo-bathymetry reconstruction and the inorganic facies modelling of the Late Jurassic Interval (157-144 Ma) are shown in **Figure 41** and **Table 8**. Based on the results, the Late Jurassic is dominated by upper bathyal bathymetries (mean water depth of 332 ± 149 m) with half graben basin geometry defined by E-W striking, northward dipping normal faults in the north, and E-W striking, southward dipping normal faults in the south and N-S striking, westward dipping normal faults in the west of the HB and in the boundary area between the HB and RLFC at the westernmost part of the study area (**Figure 41**). There is a deep-shelf area with PWD of 500-900 m in the northwesternmost of the HB, separated from the half-graben area (PWD of 50-500 m) by the facies boundary (**Figure 41**). Based on the histogram of PWD's (**Figure 41**), the Late Jurassic Interval typically depicts a unimodal distribution skewed to the right with a long right-tail. The right-skewed distribution indicates a wide range of PWD distributions in the basin with the shallower water depths dominating the area (half-graben area). The long right-tail in the skewed distribution illustrates a local greater water depth area as found in the northwesternmost of the basin (deep-shelf area) (**Figure 41**). This histogram distribution is also reflected by the high standard deviation of the Late Jurassic Interval (**Figure 41** and **Table 8**).

Laterally, the bathymetry configuration of the Late Jurassic Interval is controlled by the normal faults in the basin. The neritic-upper bathyal bathymetries zone (PWD 20-250 m) is mainly bounded by the normal faults including the E-W trending basin-axis, the RLFC, and the

block in between two N-S striking, west-dipping normal faults where the shallowest water depths (20 m) occur (**Figure 41**). In the north of the E-W striking, north dipping normal faults and in the south of the E-W striking, south dipping normal fault, the water depths are within the range of upper bathyal zone (PWD 250-500 m). The middle bathyal bathymetry zone is only found in the northwesternmost of the basin as the deep-shelf environment (PWD 500-900 m) (**Figure 41**). Within the interval, there is a slight shallowing trend of mean water depth from 370 ± 146 m during 157-154 Ma to 324 ± 148 m during 154-144 Ma (**Table 8**). The shallowing water depth mainly occurrs in the western N-S trending block and the RLFC of the study area (**Figure 42**).

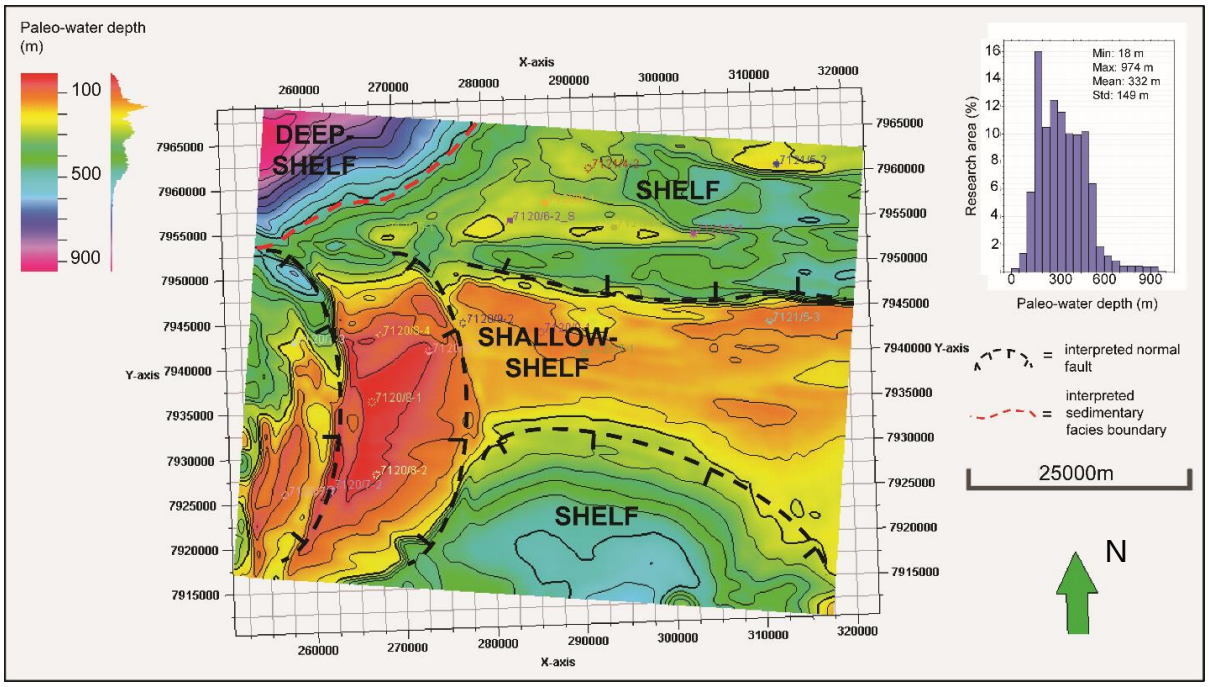

Figure 41. Interpreted paleo-water depth (PWD) map of the top Late Jurassic Interval (144 Ma) with the histogram of water depth values during the Late Jurassic (157-144 Ma).

During the Late Jurassic, the lithology is dominated by shale as indicated by very low value of the SF (0.01 ± 0.01 and 0.02 ± 0.02) both vertically and laterally (**Table 8** and **Figure 42**) without any significant trend as compared to the Early-Mid Triassic Interval. The shale dominated lithology of the Late Jurassic is also reflected by very low mean value of DBD (0.68 ± 0.01 and 0.69 ± 0.01 g/cm^3), which generally correlates with the SF value distribution (**Table 8**). Minor variations of the SF values are constrained within 0.02-0.12 in the southern margin of the basin and in the northern part of the basin as scattered deposit (**Figure 42**). These may imply that the sediment supply entered the basin from the south and north during the Late Jurassic (**Figure 42**).

Table 8. The results of the inorganic facies modelling of the Late Jurassic Interval.

Inorganic facies	Formation	Age (Ma)	Min	Max	Mean	Std
Paleo-water depth (m)	Krill Member	154-144	18	965	324	148
	Alge Member	157-154	115	974	370	146
Sedimentation rate (cm/ka)	Krill Member	154-144	0	20	2	2
	Alge Member	157-154	0	6	1	1
Sand fraction	Krill Member	154-144	0	0.12	0.02	0.02
	Alge Member	157-154	0	0.07	0.01	0.01
Dry bulk density (g/cm^3)	Krill Member	154-144	0.68	0.76	0.69	0.01
	Alge Member	157-154	0.68	0.72	0.68	0.01

The Late Jurassic is dominated by very slow sedimentation rates (mean sedimentation rate of 1 ± 1 cm/ka during 157-154 Ma and 2 ± 2 cm/ka during 154-144 Ma) (**Table 8** and **Figure 42**). The sedimentation mostly took place in the north of the E-W striking, north dipping normal fault and in the two west dipping fault blocks of the basin (**Figure 42**). In the northern part, sedimentation rate increases northward, from 1 cm/ka to 2 cm/ka, whereas in the two west dipping fault blocks the sedimentation rate is increasing toward the southwest, from 1 cm/ka to 3 cm/ka (**Figure 42**). In contrast, there is almost no sedimentat filling the E-W trending basin axis, eastern of the southern margin, and in the northwest deep-shelf area (**Figure 42**). This may indicate that the main sediment accumulation areas during the Late Jurassic are the northern area and the western fault blocks, constrained by the normal faults in the basin. Within the interval, there is a slow-intermediate rate of sedimentation filling the basin during the period of each member's upper depositional period (6 cm/ka at 154-152 Ma and 20 cm/ka at 144 Ma) (**Figure 42**).

Throughout the Late Jurassic, the primary productivity (PP) is very high in general especially in the lower interval (Alge Member). The mean value of the PP is 138.70 ± 15.02 $gC/m^2/a$ for the lower interval (157-154 Ma), whereas the upper interval (Krill Member, 154-144 Ma) has a mean value of PP 62.36 ± 34.42 $gC/m^2/a$ (**Table 9**). The very high primary productivity during the Late Jurassic produces very high quantity of the MOM which mainly constitutes the TOC. The sedimentation rate is very slow, delivering shale dominated sediment and affect the distribution of more C_{res} amounts with minor C_{terr} (**Table 9**).

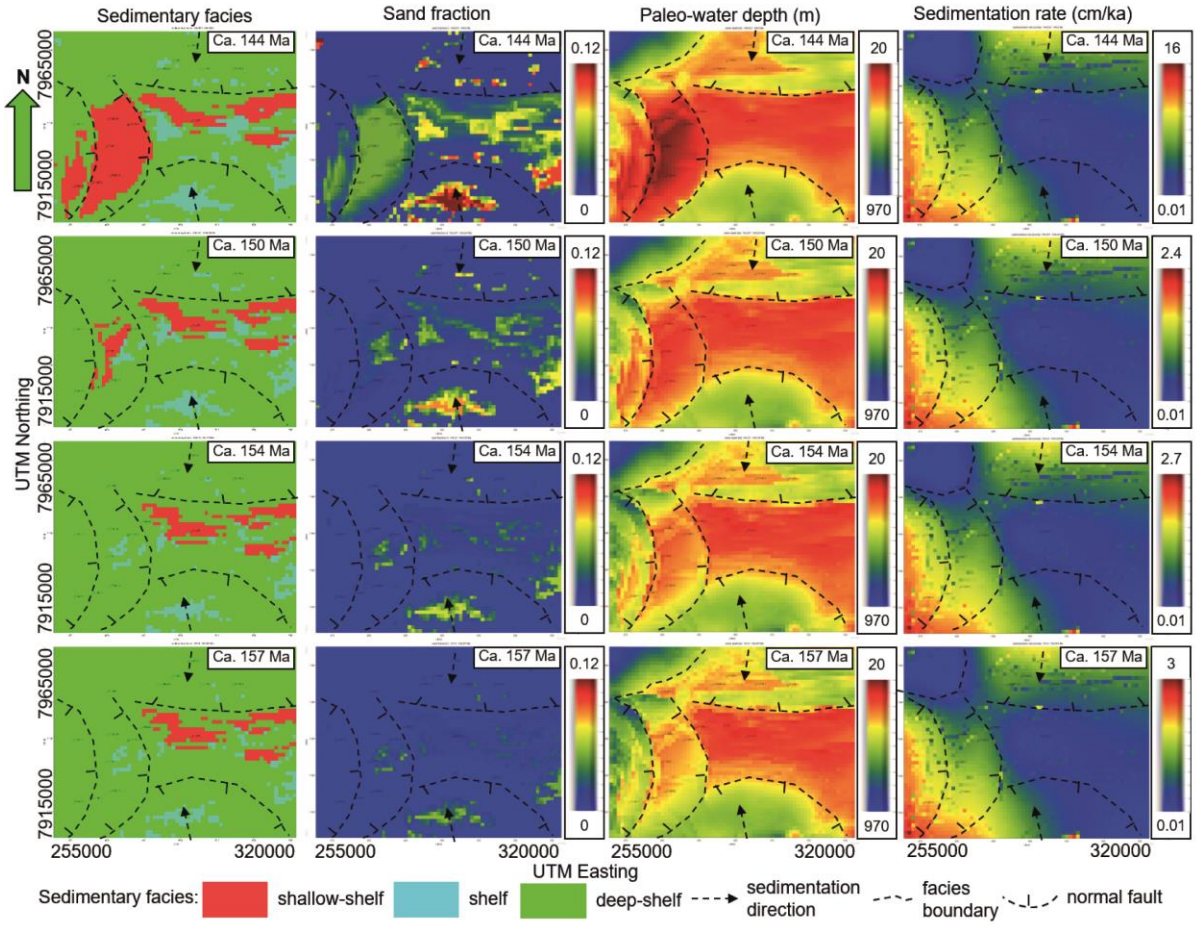

Figure 42. The interpreted 2D maps of the inorganic facies modelling results of the Late Jurassic Interval through certain time periods within the interval. Note that not all of the facies use the same scale. Instead, due to the different range of facies values between particular time-slices, auto-scale is sometimes preferred to visualize the lateral distribution.

In general, the amounts of both C_{res} and MOM in the Late Jurassic are good-very good quantity as indicated by their mean value trend through time. The C_{res} values are 2.74 ± 1.12 wt% and 1.20 ± 0.99 wt% and the MOM values are 6.60 ± 0.10 wt% and 2.87 ± 1.27 wt% at the 157-154 Ma and 154-144 Ma correspondingly (**Table 9**). On the other hand, the mean values of C_{terr} are 0.04 ± 0.07 wt% during 157-154 Ma and 0.08 ± 0.09 wt% during 154-144 Ma. These affects the distribution of the very good quantity of TOC as indicated by the mean TOC values of 9.38 ± 1.15 wt% for the Alge Member and 4.15 ± 2.09 wt% for the Krill Member (**Table 9**). The maximum/high TOC values (11.43-13.87 wt%) are mainly accumulated in the two fault blocks and the northern part of the basin. On the contrary, the minimum TOC values (1.73-6.52 wt%) are mainly accumulated in the northwestern deep-shelf and the southeasternmost margin of the basin (**Table 9** and **Figure 43**).

Table 9. The results of the organic facies modelling of the Late Jurassic Interval.

Organic facies	Formation	Age (Ma)	Min	Max	Mean	Std
Primary productivity ($gC/m^2/a$)	Krill Member	154-144	2.24	129.39	62.36	34.42
	Alge Member	157-154	107.61	175.84	138.70	15.02
Marine organic matter (wt%)	Krill Member	154-144	1.54	6.09	2.87	1.27
	Alge Member	157-154	6.06	6.74	6.60	0.10
Residual organic carbon (wt%)	Krill Member	154-144	0	6.19	1.20	0.99
	Alge Member	157-154	0.01	7.16	2.74	1.12
Terrigenous organic carbon (wt%)	Krill Member	154-144	0.01	0.60	0.08	0.09
	Alge Member	157-154	0	0.54	0.04	0.07
Total organic carbon (wt%)	Krill Member	154-144	1.73	11.43	4.15	2.09
	Alge Member	157-154	6.52	13.87	9.38	1.15
Hydrogen index (mgHC /gTOC)	Krill Member	154-144	61	344	187	61
	Alge Member	157-154	61	314	198	44

Regarding the source rock quality and kerogen type, the Late Jurassic Interval is dominated by high-very high HI as indicated by the HI modelling results (**Table 9**). Both lower and upper intervals have high mean value of HI, 198 ± 44 mgHC/gTOC at 157-154 Ma and 187 ± 61 mgHC/gTOC at 154-144 Ma which are commonly distributed in the basin axis and some areas of the northern part of the basin (**Table 9** and **Figure 43**). In the two fault blocks and the eastern part of the northern area, the HI values are dominated by maximum/very high values, 250-344 mgHC/gTOC (**Figure 43**). On the contrary, the northwest deep-shelf and the southeasternmost margin of the basin show minimum HI values of 61 mgHC/gTOC (**Figure 43**).

Within the Late Jurassic Interval, there is a decreasing trend of each organic facies from the lowermost part (157 Ma) to the uppermost part of the interval (144 Ma). The time of 157 Ma is represented by the maximum value from each organic facies including MOM (6.74 ± 0.10 wt%), C_{res} (7.16 ± 1.12 wt%), C_{terr} (0.54 ± 0.07 wt%), TOC (13.87 ± 1.15 wt%), and HI (313.65 ± 43.68 mgHC/gTOC) (**Table 9** and **Figure 43**). These gradually decrease toward the younger interval until finally the organic facies reach their minimum values generally at 144 Ma. The age of 144 Ma, contrary to the age of 157 Ma, is represented by the minimum value from each organic facies including MOM (1.54 ± 1.27 wt%), C_{res} (0 ± 0.99 wt%), C_{terr} (0 ± 0.09 wt%), TOC (1.73 ± 2.09 wt%), and HI (61 ± 60.59 mgHC/gTOC).

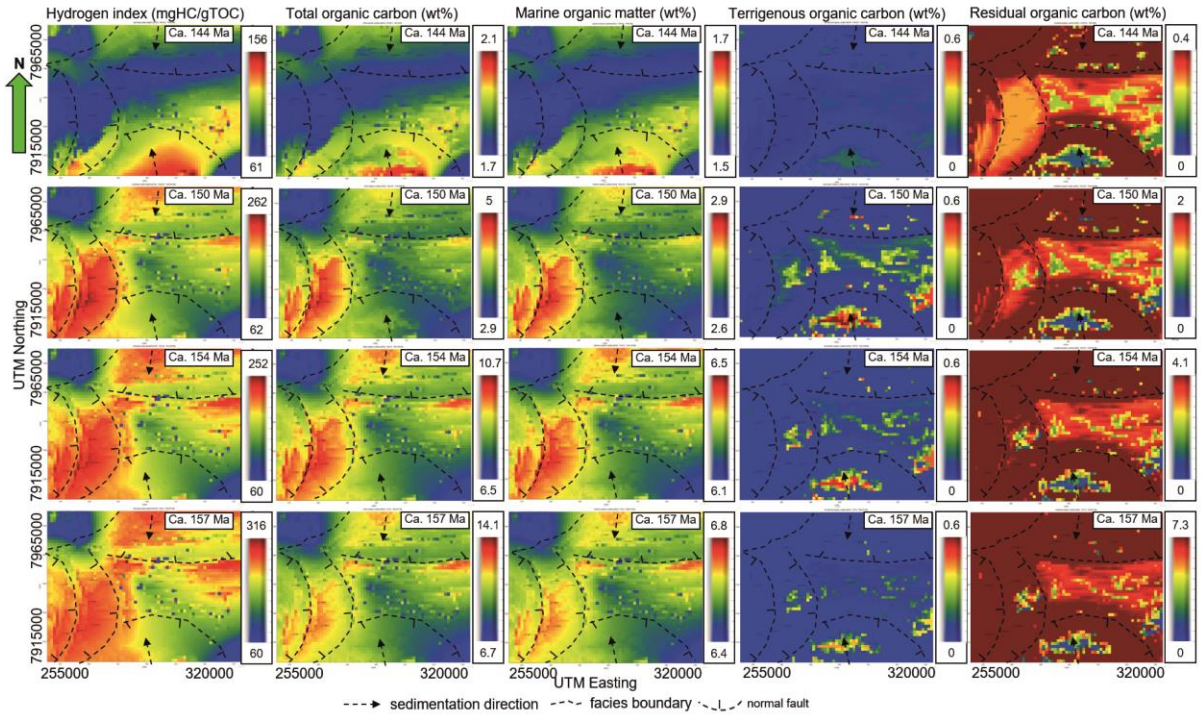

Figure 43. The interpreted 2D maps of the organic facies modelling results of the Late Jurassic Interval through certain time periods within the interval. Note that not all of the facies use the same scale. Instead, due to the different range of facies values between particular time-slices, auto-scale is sometimes preferred to visualize the lateral distribution.

Laterally, the organic facies distributes according to the basin-fill deposition during the Late Jurassic (**Figure 43**). The TOC disperses following the pattern of MOM distribution. Similarly, HI also scatters reflecting the TOC distribution pattern. Both TOC and HI are higher in the two western fault blocks and in the northern part than the northwestern deep-shelf, southeasternmost margin, and E-W basin axis of the basin (**Figure 43**). C_{terr} and C_{res} are mainly dispersed following the same pattern of SF distribution in which a higher SF is followed by higher C_{terr} and lower C_{res} and vice versa (**Figure 43**).

4.2.2 Interpretations

Based on the results, the Late Jurassic (157-144 Ma) is a period of shallow PWD with neritic-upper bathyal bathymetries in the HB part (20-500 m) and middle bathyal bathymetry in the RLFC part (500-900 m) of the basin (**Figure 42**). The paleo-bathymetry of the Late Jurassic is controlled by normal faults, forming half-graben geometry in the basin during the Late Jurassic (**Figure 42**). This is associated with the Mid Jurassic-Early Cretaceous block-faulting along E-W to NE-SW trending and N-S trending, west-dipping normal faults (Clark et al., 2013) associated with active rifting periods in the Barents Sea (Faleide et al., 2008; Faleide et al., 1993).

Syn-rift stratigraphic pattern

Generally, the Late Jurassic has a slight shallowing upward trend of water depth (**Figure 44**), which contradicts the global sea-level rise during the Late Jurassic (Haq et al., 1987; Miller et al., 2005). Since the Late Jurassic Interval has been deposited during the syn-rift phase and rotation of the fault blocks, the tectonic activity can outpace the global sea-level rise. The tectonic activity can also outpace the very slow sedimentation rate (1-5 cm/ka) (**Figure 44**). Since the sedimentation rate is very slow during the Late Jurassic, the fluctuation of the water depth is predominantly driven by the tectonic activity during the Late Jurassic. In the study area, the slight shallowing of the PWD commonly occurs in the two west-dipping fault blocks, including the HB part and the RLFC part, bounded by the N-S striking, west dipping normal faults in the western part. Separately, the rest of the basin are subjected to slight deepening of the PWD (**Figure 42**). The slight shallowing of the PWD may be controlled by the rotation of the fault blocks during the Late Jurassic, uplifting part of the fault blocks and outpacing the global sea-level rise. On the other hand, the slight deepening of the PWD may result from the increased tectonic subsidence as well as the global sea-level rise. Since the water depth fluctuation in the basin is small; for example in the E-W trending basin axial part it deepens from ca. 130 m during 157 Ma to ca 150 m during 144 Ma (**Figure 42**). The subsidence rate is probably very low during the Late Jurassic. It infers relatively stable tectonic conditions during the deposition, also indicated by a very slow and relatively stable sedimentation rate (**Figure 44**). During the syn-rift phase, these conditions may be encountered in the late syn-rift stage. The fluctuation of sedimentation rate during 153-152 Ma and ca 145-144 Ma may correspond to the rise of sea-level as well as the change of sedimentation. The first peak corresponds to the transition from the lower unit Alge Member to the upper unit Krill Member, while the later peak relates to the transition to Early Cretaceous sedimentation.

A very slow sedimentation rate results from the low amount of sediment input into the basin during the Late Jurassic. This is well indicated by thin shale deposits with thicknesses of less than ca. 200 m (**Figure 45**) as a result of the Late Jurassic deposition. The shale thickness shows a slight lateral thickening pattern toward the normal faults, emphasizing a syn-sedimentary control during the active rifting period (late syn-rift) (**Figure 45**). The low input of the sediments may signify the global sea-level rise in the source area, preventing the source area from erosion. As a result, the Late Jurassic is dominated by low amount of shale (SF 0-0.02) deposition with limited sand content (max SF ca. 0.12) (**Table 8**). Based on the SF and sedimentation rate distribution, the sediment is mainly sourced from both the south and north

of the study area. It mainly accumulates in the northern area and the western fault blocks, where the higher sedimentation rate is found (**Figure 42**). Since the deposition of the Late Jurassic took place during the syn-rift period, as well as the rise of global sea-level with very slow sedimentation rate, the basin develops into more sediment-starved basin. The half graben geometry, especially in the fault blocks, may promote the preservation of the basin fill as tectonically bordered-restricted depositional environments (**Figure 45**).

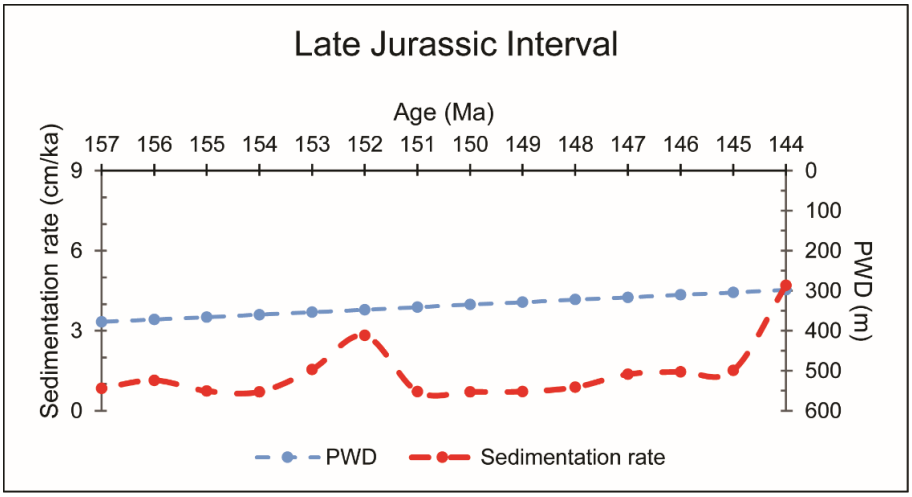

Figure 44. Mean paleo-water depth and mean sedimentation rate change through time during the Late Jurassic. The sedimentation rate curve shows a relatively stable and very slow sedimentation rate with some fluctuations during 153-151 Ma and at the end of deposition. The paleo-water depth (PWD) curve shows a shallowing trend throughout the Late Jurassic.

Based on the SF and sedimentation rate distribution, there are low amounts of sediments in the E-W trending basin axis, the eastern part of the southern margin, and the northwest deep-shelf area (**Figure 42**). The low amounts of sediment accumulation in the northwest deep-shelf area are due to remoteness of the sink area from the source. Besides, since the sedimentation rate is very slow, the sedimentation is not able to further transport the material toward this area. The low amounts of sediments in the E-W trending basin axis and in the eastern part of the southern margin are probably due to erosion as these areas are the main footwall areas in the basin that may experience later uplift and erosion (**Figure 42**). In addition, there is an accumulation of higher SF content within the shale deposit (SF 0.06-0.12) in the southern margin of the basin. This accumulation is most likely sourced from the south, filling the basin as sediment by-pass through the steep fault scrap in the south (**Figure 42** and **Figure 46**). Sediment by-pass in the sediment-starved environment is typical for rift settings especially during the syn-rift period. In addition, since the sedimentation rate is higher in the southern and northern margins, the sediment loading causes subsidence of these hanging wall areas, therefore the footwall areas in the E-W basin axis compensate through flexural uplift (**Figure 46**). The

mechanism of the flexural uplift is the main control on the basin-bulge geometry with E-W trending structures in the HB.

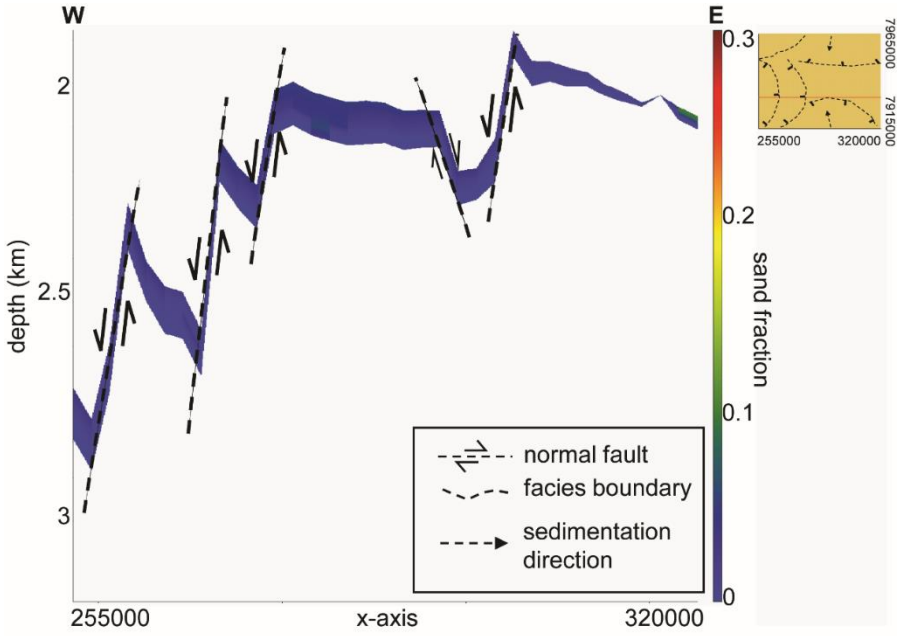

Figure 45. An East-West cross-section of the Late Jurassic shale deposits. The sand fraction (SF) distribution shows no significant variation both vertically and laterally. The normal faults subdivide the basin into several fault blocks which potentially become locally restricted deep-water environments. in some of the fault blocks.

The Hekkingen Fm is deposited and is divided into two members: the Alge Member and the Krill Member (Georgiev et al., 2017). The Alge Member is deposited during the period 157-154 Ma (Georgiev et al., 2017). During the deposition, the sedimentation is slight slower than the upper unit (sedimentation rate 1-6 cm/ka) in a deeper paleo-bathymetry (**Table 9**). This period is also more stable than the later period as the fault block rotation is not so intense, as indicated by no shallow-shelf facies in the western fault blocks. The end of the Alge Member deposition is marked by a slight increase of sedimentation rate during 154-153 Ma from ca 1 cm/ka to 2-3 cm/ka (**Figure 44**) as well as the rotation of the fault blocks, indicated in the sedimentary facies and PWD map (**Figure 42**). Based on the global sea-level curve (Miller et al., 2005), the period 154-153 Ma is also marked by a drop of the global sea-level.

Following, the deposition of the Alge Member, deposition of the Krill Member took place during 154-144 Ma (Georgiev et al., 2017). During the deposition, the sedimentation rate is slightly higher than the underlying unit (sedimentation rate 2-20 cm/ka) with a shallower paleo-bathymetry (**Table 9**). This period is also marked by the rotation of the western fault blocks as indicated by relatively rapid shallowing of the water depth, from ca. 270 m to ca. 20 m, as well as the development of the shallow-shelf facies in the western fault blocks (**Figure 42**). The end

of the Krill Member deposition is marked by a slight increase of sedimentation rate during 145-144 Ma from ca. 2 cm/ka to ca. 5 cm/ka (**Figure 44**). Based on the global sea-level curve (Miller et al., 2005), the period of 145-144 Ma is also marked as drop of the global sea-level. The different characteristics of the basin-fill process as well as tectonic conditions of each member affect the distribution of the organic matter and the preservation conditions during the Late Jurassic.

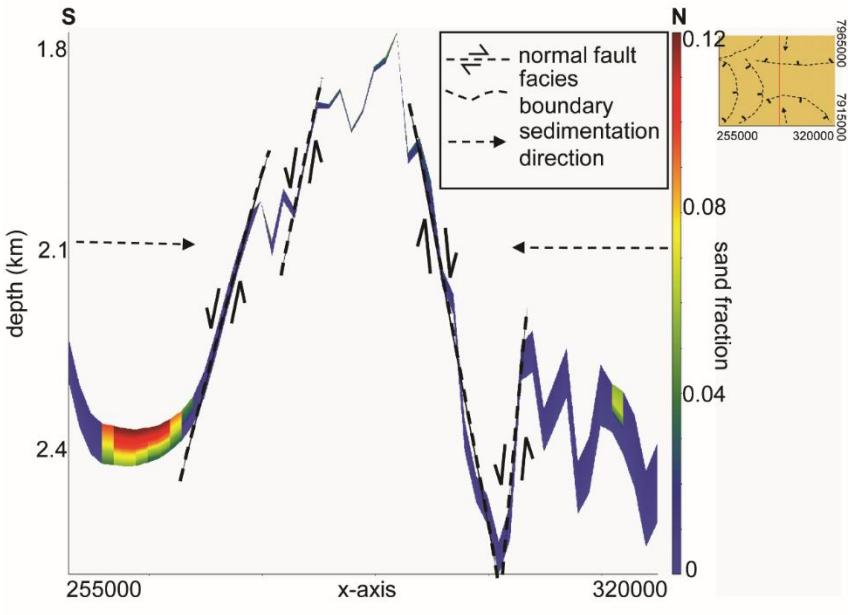

Figure 46. A North-South cross-section of the Late Jurassic shale deposits. Sediments with higher sand fraction content accumulate in the south part of the basin as a sediment-bypass from the nearby fault scarp. The result of the flexural uplift of the HB bulge is also seen in the cross section, represented by the E-W basin axis.

Organic matter source types

Based on the results (**Table 9** and **Figure 43**), the organic facies distribute according to the basin-fill deposition during the Late Jurassic. The Late Jurassic Interval is more marine-sourced in terms of organic matter (autochthonous) with a good-very good quantity of the MOM (1.54-6.74 wt%) as a result of generally very high primary productivity (2.24-175.84 gC/m^2/a) (**Table 9**). The poor quantity of the C_{terr} (mean C_{terr} 0.04-0.08 wt%) (**Table 9**) and very slow sedimentation rate (mean sedimentation rate 1-5 cm/ka) (**Figure 44**) support this interpretation, signifying that the terrestrial input contributes insignificant amount to the organic matter quantities in the basin during the Late Jurassic.

The HB was an enclosed basin in the Late Jurassic, as a result of the Mid Jurassic-Early Cretaceous rifting periods. Due to the relatively proximal distance to the surrounding shorelines, the HB obtains more nutrient supply input from continental run-off that may

contribute to the PP during the Late Jurassic due to a favourable setting for marine organisms. The enclosed basin is also a favourable environment for the development of marine phytoplankton, especially in the arid climatic regions. Besides, the water depth during the Late Jurassic is not as great as in the Early-Mid Triassic, reducing the degradation of carbon during settling. Additionally, the rise of the sea-level may also boost the amount of marine alginite in the basin. All of these conditions contribute to the very high PP during the Late Jurassic.

The high amount of the C_{res} is as a result of shale accumulation in the basin as the OF-Mod associates C_{res} with shale deposition in the low-energy hydrodynamic regime. Based on the C_{res} distribution map (**Figure 43**), the C_{res} distribution is associated with the SF distribution (**Figure 42**), indicating that the C_{res} is sourced from the source area and transported with the shale deposit. The Cres alternatively can be sourced from the degraded carbon flux during the settling in the water column as well. Due to the sea-level rise, as well as deepening of the PWD in most part of the basin, the distance to the shoreline may increase and thus reduce the amount of the transported C_{res} in the basin (**Figure 43**). However, the C_{res} may also have resulted from the degradation of the aerobic bacteria as indicated by the extent of C_{res} deposition in most parts of the basin (**Figure 42**). This, however, must occur under anoxic conditions due to the absence of bottom-water oxygen (Allen and Allen, 2013).

Since the organic matter is mainly marine-sourced and related to the primary productivity, the MOM is mainly derived from the marine algae and bacteria such as exinite and sporinite. This signifies type II kerogen and therefore the HI values are relatively high (61-344 mgHC/gTOC) during the Late Jurassic. The very high quantity of the organic matter during the Late Jurassic is probably related to the very slow-slow sedimentation rate (limited dilution) and the late syn-rift setting. In this setting, subsidence rate outpaces the sedimentation rate. In addition, the preservation conditions during the Late Jurassic play an important role in determining the high quantity and quality of the organic matter.

Preservation conditions

The organic matter of the Late Jurassic Interval is marine-sourced, MOM, and it is generally prone to be degraded as well as diluted during deposition. Thus, the preservation of the MOM depends on some factors, including environment conditions during deposition, such as water depth, sediment grain size and sedimentation rate. The shallow water depths during the Late Jurassic may favor the MOM preservation since the reduced carbon flux is limited and the scavenging of organic matter by fauna during the settling in the water column is limited.

This is indicated by the very good quantity of the MOM preserved throughout the Late Jurassic (1.54-6.74 wt%) (**Figure 43**).

The Late Jurassic Interval is dominated by shale deposition (SF of 0-0.12) that may also enhance the preservation of the organic matter in the sink as shale has low permeability (**Table 8**). The low permeability of shale inhibits the diffusion of oxidants from the water column into the sediments. This is in contrast with the Early-Mid Triassic shaly-sand, where the deposition take place in a high-energy environment and is most likely well oxygenated. Therefore, the bacterial activity is lower in the Late Jurassic Interval than in any other coarse-grained sediments.

The sedimentation rate throughout the Late Jurassic is very slow (mean sedimentation rate 1-2 cm/ka) (**Table 8**) and this also favors the preservation of the organic matter in the sediments. Since the sedimentation rate is very slow, the amount of mineral matter filling the basin will be low and thus the dilution of the organic matter is limited. The shallow water depth, as well as shale deposition and very slow sedimentation rate, are the important factors favoring the source rock bed deposition during the Late Jurassic.

The Alge Member is deposited with slightly slower sedimentation rates than the Krill Member. These conditions favor the preservation as clastic dilution is strongly limited. In combination with high TOC (6.52-13.87 wt%) and HI (61-314 mgHC/gTOC) deposition take place in a favourable preservation condition with elevated surface PP (107.61-175.84 $gC/m^2/a$).

The Krill Member is deposited with a slight faster sedimentation rate than the Alge Member. However, since it is still in the range of very slow-slow sedimentation rate (mean sedimentation rate ca. 2 cm/ka), clastic dilution is still limited and thus favorable for preservation of organic matter. Good preservation conditions are reflected by relatively high TOC (1.73-11.43 wt%) and HI (61-344 mgHC/gTOC) values in the Krill Member, indicated the extent of favourable preservation conditions with elevated surface PP (2.24-129.39 $gC/m^2/a$) in the Krill Member as well.

Nevertheless, the Krill Member has lower TOC than the Alge Member because of different basin-fill process as well as preservation conditions between two members. During the deposition of the Krill Member, the two western blocks as the main accumulation of the basin-fill experienced rapid shallowing due to fault block rotation in the Late Jurassic. The rapid shallowing of the fault blocks weakens the water-column preservation as the water movement is more intense in the shallow water and thus limits the stratification in the water column. Besides, the PP is decreasing upward due to the shallowing of the PWD in the fault blocks. The

active rotation of the fault blocks may not be favorable for marine organisms, as a quiet environment is more favourable for marine organism development. However, the subsided part of the fault block (near the normal faults) may still serve good conditions for preservation as it has deeper environment than the uplifted part and the sediment is thickening in this area. Further, this area can have a local deep-restricted depositional environment, bounded by the uplifted part of the fault block and the normal fault.

Finally, the sedimentation rate is faster during Krill Member deposition, especially in the transition from the Alge Member to the Krill Member deposition and at the end of Krill Member deposition. The fastest rate can reach ca. 20 cm/ka. The higher sedimentation rate dilutes the organic matter and as a result the TOC value is lower in the Krill Member. However, the sedimentation may also provide additional organic matter input to the source rock, thus contributing to the HI, as HI during the Krill Member remains high even with lower TOC.

Laterally, the preservation conditions increase in the main accumulation area in the basin (the western fault blocks and the northeastern hanging wall area) as indicated by the accumulation of high TOC and HI values (**Figure 43**), following the higher sedimentation rate (**Figure 42**). The fact that the main accumulation area has a greater sedimentation rate reflects thicker shales are deposited there, enhancing the organic matter preservation. Additionally, good preservation conditions are also found in the thinner shale areas of the E-W trending basin axis, indicating that the deepening trend of the PWD and slower sedimentation rate in the corresponding area enhance the organic matter preservation. However, due to the thinner shale accumulation, the remoteness of the area from the nutrient supply and sedimentation, and the openness of the area as the main footwall in the basin, the preservation conditions are worse than the main accumulation area (**Figure 43**). On the contrary, the northwestern deep-shelf area in the basin shows the worst preservation conditions in the basin as indicated by the lower TOC and HI values throughout the Late Jurassic (**Figure 43**). This is probably related to the greatest water depths in the basin (500-970 m), as well as the remoteness of the area from the nutrient supply and sedimentation (**Figure 43**). Variously, in the later stages of deposition (146-144 Ma), when the sedimentation rate is faster (reaching ca. 16 cm/ka), the preservation trend shows a different distribution (**Figure 43**). The better preservation is dispersed especially in the southern margin with ENE-WSW trend (**Figure 43**), where the sedimentation rate is slower and the water depth is much greater than in the fault blocks (**Figure 42**).

Source rock potential and distribution

In general, the Late Jurassic Interval has a good-very good source rock potential with a few poor-fair intervals in the upper part of the Hekkingen Fm (**Figure 47**). Source rocks distribute according to the basin-fill process especially the sedimentation rate as well as the paleo-bathymetry, controlled by the half-graben geometry in the basin. Laterally, the main accumulation of the high quantity (TOC 3-18 wt%) and quality (HI 200-340 mgHC/gTOC) source rocks are in the western fault blocks and the northern hanging wall part of the basin in the Late Jurassic Interval (**Figure 43**). The lowest quantity (TOC 1.7-6.5 wt%) and quality (HI ca. 60 mgHC/gTOC) of the source rocks are in the northwest deep-shelf area of the basin.

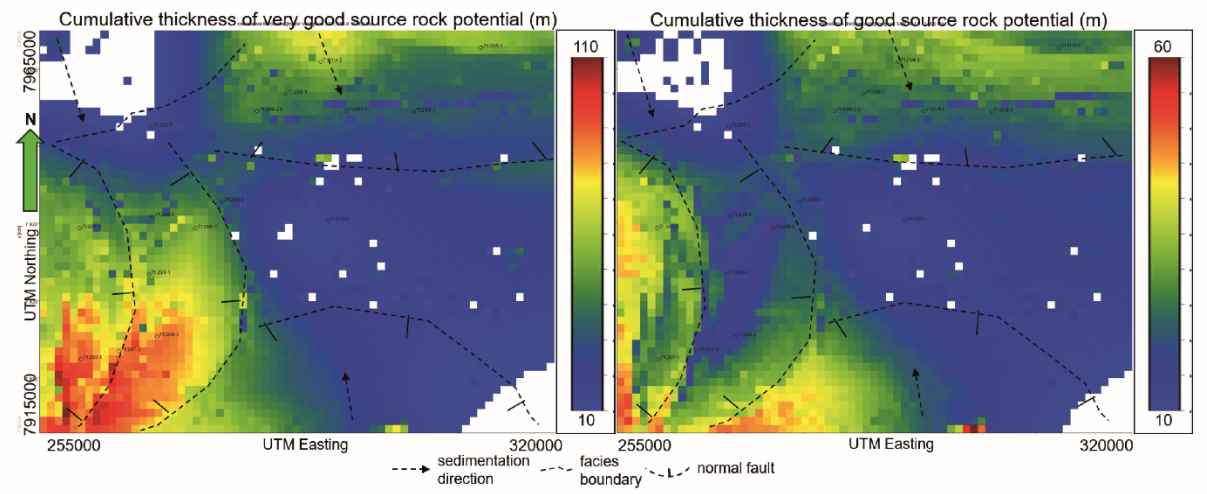

Figure 47. Cumulative thickness of the source rock potential distribution of the Late Jurassic Interval.

Vertically, the best source rock potential in the Late Jurassic is within the Alge Member and lower-middle part of the Krill Member (157-148 Ma), dominated by very good source rock potential (TOC 6-13 wt%, HI 200-340 mgHC/gTOC) (**Figure 48**). The source rock potential is gradually decreasing from good potential at ca. 148 Ma toward poor potential at 144 Ma (TOC 1.7-6 wt%, HI 60-200 mgHC/gTOC) (**Figure 48**).

The Alge Member and lower-middle part of the Krill Member are more favorable for the source rock potential due to a deeper water column, elevated primary productivity, and slower sedimentation rate. In addition, since the organic matter quantity-quality and the preservation conditions are generally high, the Late Jurassic Interval has good-very good source rock potential in the study area. The source rock is mainly constituted from type II kerogen with very good quantity, thus it has potential to generate oil/gas in economic amounts. The main kitchen areas are the western fault blocks and the northern hanging wall part of the basin which are dominated by good-very good source rock potential. Generally, the shale deposition in an

enclosed basin with half-graben geometry and relatively shallow water depth, in combination with elevated primary productivity, marine-sourced organic matter, favourable preservation conditions, very slow-slow sedimentation rate, relatively quiet tectonic conditions, and global sea-level rise favor the deposition of good-very good oil/gas-prone source rocks during the Late Jurassic in the HB.

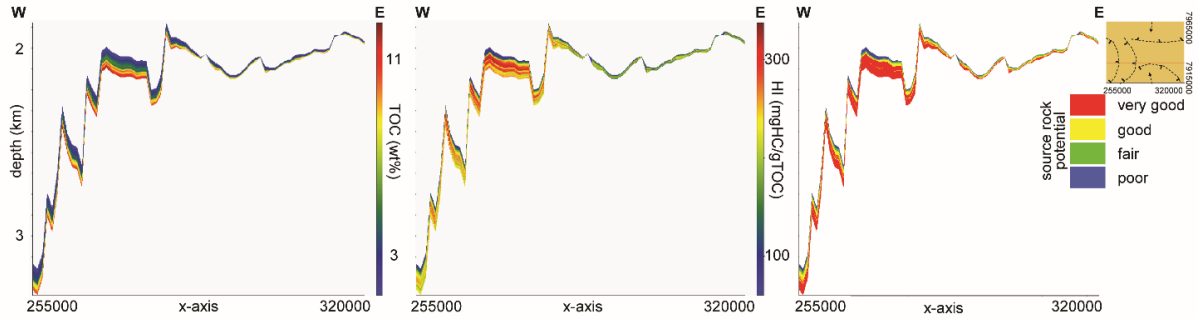

Figure 48. An east-west cross section of the TOC-HI accumulations and the source rock potential for the Late Jurassic Interval. Vertically, the best source rock potential occurs in the whole interval, including the Alge Member and part of Krill Member, except the uppermost interval. Generally, it is dominated by very good source rock potential.

4.3 Early Cretaceous Interval

4.3.1 Results

The results of the paleo-bathymetry reconstruction and the inorganic facies modelling of the Early Cretaceous Interval (157-144 Ma) are shown in **Figure 49** and **Table 10**. Based on the results, the Early Cretaceous is dominated by upper-middle bathyal bathymetries (mean water depth of 326 ± 115 m) with shallow-shelf – deep-shelf depositional environment. The shelf is separated by N-S striking, westward dipping normal faults in the west and an ENE-WSW trending facies boundary in the basin-axis and in the northwestern part of the basin (**Figure 49**). The HB is separated from the Tromsø Basin by the deep-shelf of the RLFC in the westernmost part of the study area (**Figure 1**). During the Early Cretaceous, the water depth was ranging from 280-600 m in the HB part, whereas the water depth was 420-770 m in the RLFC part of the study area (**Figure 49**).

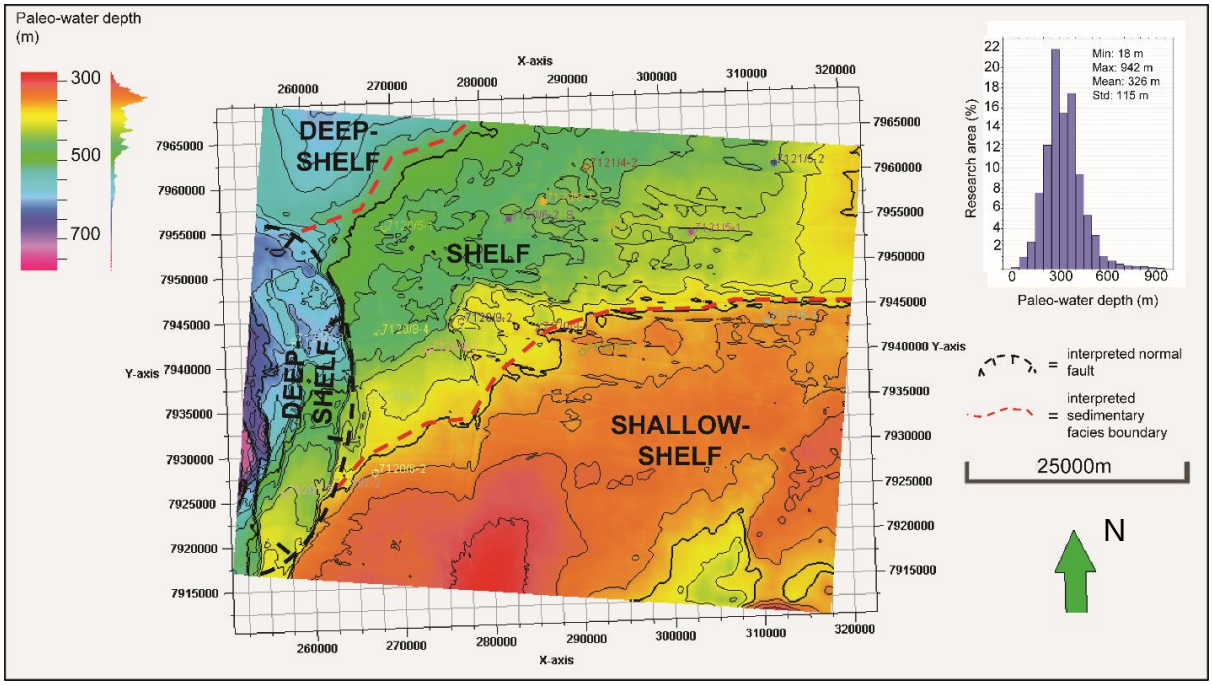

Figure 49. Interpreted paleo-water depth (PWD) map of the top Early Cretacecous Interval (113 Ma) with the histogram of water depth values during the Early Cretaceous (134-113 Ma).

In the HB part, the PWD is shallowing gradually toward the northwest, from the shallow-shelf facies in the southeast (PWD 280-400 m) toward the shelf facies (PWD 380-500 m) and the deep-shelf facies (PWD 500-600 m) in the northwestern-most part of the HB (**Figure 49**). Based on the PWD histogram (**Figure 49**), the Early Cretaceous Interval typically depicts a unimodal distribution skewed to the right. The right-skewed distribution indicates a wide range of PWD distributions in the basin with the shallower water depths dominating the area (the HB part). The right tail in the skewed distribution illustrates a local deeper water depth area as found in the deep-shelf area of the RLFC (**Figure 49**). Within the interval, the lower part (134-130 Ma) depicts a similar basin geometry as the Late Jurassic Interval with half-graben and deep-shelf features (**Figure 41**). On the other hand, the upper part (130-113 Ma), which predominantly forms the Early Cretaceous depositional environment, shows a shelf depositional environment separated by facies boundaries (**Figure 50**), similar to the Early-Mid Triassic Interval (**Figure 32**). There is a slight deepening trend of mean water depth in general from 307 ± 151 m during 134-130 Ma to 333 ± 98 m during 130-113 Ma (**Table 10**). The deepening of the water depth mainly occurs in the western fault block, the RLFC, the E-W trending basin-axis, and the northern margin of the study area. Alternatively, the shallowing of the water depth is mainly constrained in the southern margin and the northwestern-most part of

the basin (**Figure 50**). This configuration shapes the shelf depositional environment during the Early Cretaceous in general.

Table 10. The results of the inorganic facies modelling of the Early Cretaceous Interval.

Inorganic facies	Formation	Age (Ma)	Min	Max	Mean	Std
Paleo-water depth (m)	Kolje Fm	130-113	76	857	333	98
	Klippfisk Fm	134-130	18	942	307	151
Sedimentation rate (cm/ka)	Kolje Fm	130-113	0.5	69	7	7
	Klippfisk Fm	134-130	1	104	12	9
Sand fraction	Kolje Fm	130-113	0.39	0.81	0.64	0.11
	Klippfisk Fm	134-130	0.15	0.62	0.30	0.06
Dry bulk density (g/cm^3)	Kolje Fm	130-113	0.94	1.23	1.11	0.08
	Klippfisk Fm	134-130	0.78	1.10	0.88	0.04

During the Early Cretaceous, the lithology shows a sharp transition from sandy-shale deposition during 134-130 Ma with mean SF of 0.30 ± 0.06 to shaly-sand deposition during 130-113 Ma with mean SF of 0.64 ± 0.11 (**Table 10**). This is also reflected by low values of DBD (0.88 ± 0.04 g/cm^3) which increase during 130-113 Ma with DBD of 1.11 ± 0.08 g/cm^3 (**Table 10**). Laterally, the shaly-sand deposits are distributed mainly on the HB part while sandy-shale and shale sediments are restricted to the RLFC part of the study area (**Figure 50**). The shaly-sand deposits are filling the HB from multiple sediment sources. The shallow-shelf facies (SF 0.60-0.82) is mainly filled from the south as the SF is getting coarser northward. The shaly-sand is also filled from the north toward the northern part of the basin, which give the shelf facies depositional environment with SF 0.55-0.8 and the deep-shelf facies depositional environment with SF 0.6-0.8 (**Figure 50**).

The Early Cretaceous is dominated by slow-intermediate sedimentation rates (mean sedimentation rate of 12 ± 9 cm/ka during 134-130 Ma and 7 ± 7 cm/ka during 130-113 Ma) (**Table 10**). The higher sedimentation rates (6-45 cm/ka) commonly occur in the western part, southern part and northern part of the basin, whereas, the sedimentation rate is generally very slow in the E-W axis of the basin (1-5 cm/ka). The maximum sedimentation rate is constrained in the northwestern-most part of the basin (**Figure 50**). Within the interval, the sedimentation

is getting slower during 134-130 Ma from 2-40 cm/ka to 1-20 cm/ka, whereas during 130-113 Ma sedimentation is getting more rapid from 1-25 cm/ka to 2-45 cm/ka (**Figure 50**).

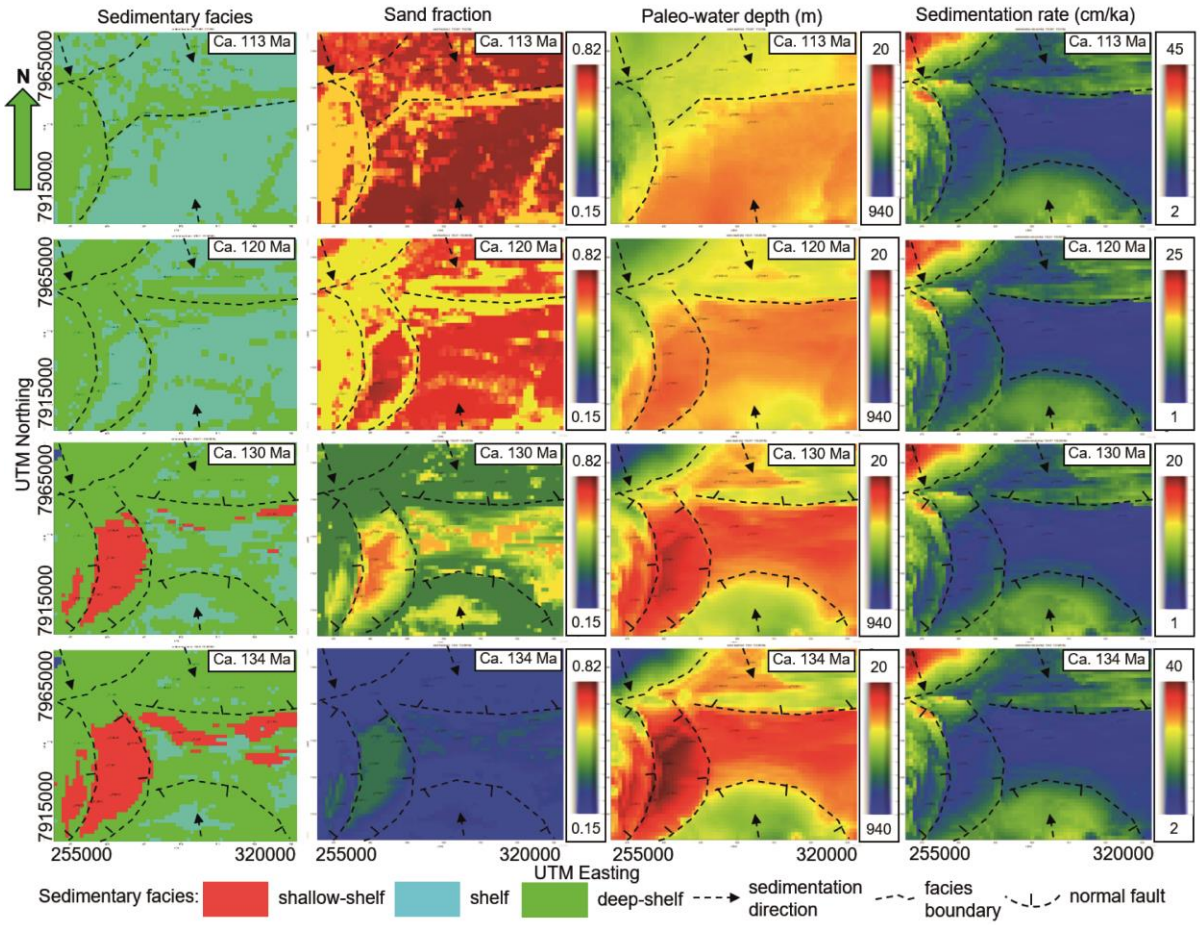

Figure 50. The interpreted 2D maps of the inorganic facies modelling results of the Early Cretaceous Interval through certain time within the interval. Note that not all of the facies use the same scale. Instead, due to the different range of facies values between particular time-slices, auto-scale is sometimes preferred to visualize the lateral distribution.

Throughout the Early Cretaceous, the primary productivity (PP) is very low in general. The mean value of the PP is 2.87 ± 0.33 gC/m^2/a during 134-130 Ma, whereas the interval of 130-113 Ma has mean value of the PP 1.01 ± 0.48 gC/m^2/a (**Table 11**). The very low primary productivity during the Early Cretaceous affects the distribution of almost zero MOM within the total amount of organic content in the Early Cretaceous source rock (**Table 11**). On the other hand, the organic contents are more related to the C_{terr} and C_{res} because of more sedimentation filling the basin during the Early Cetaceous. In general, the amounts of both C_{terr} and C_{res} in the Early Cretaceous are fair-good quantity as shown by their mean value trend through time. The C_{terr} are 1.41 ± 0.45 wt% and 0.83 ± 0.26 wt%, and the C_{res} are 1.34 ± 0.53 wt% and 0.92 ± 0.45 wt% during 134-130 Ma and 130-113 Ma respectively (**Table 11**). These

promote a distribution of good-very good quantity of TOC as indicated by the mean TOC values of 2.76 ± 0.22 wt% during 134-130 Ma and 1.76 ± 0.62 wt% during 130-113 Ma (**Table 11**).

Table 11. The results of the organic facies modelling of the Early Cretaceous Interval.

Organic facies	Formation	Age (Ma)	Min	Max	Mean	Std
Primary productivity ($gC/m^2/a$)	Kolje Fm	130-113	0.50	2.77	1.01	0.48
	Klippfisk Fm	134-130	2.13	3.97	2.87	0.33
Marine organic matter (wt%)	Kolje Fm	130-113	0	0.01	0	0
	Klippfisk Fm	134-130	0	0.03	0.01	0
Residual organic carbon (wt%)	Kolje Fm	130-113	0.28	2.09	0.92	0.45
	Klippfisk Fm	134-130	0.34	2.27	1.34	0.53
Terrigenous organic carbon (wt%)	Kolje Fm	130-113	0.38	1.85	0.83	0.26
	Klippfisk Fm	134-130	0.65	2.59	1.41	0.45
Total organic carbon (wt%)	Kolje Fm	130-113	0.66	3.09	1.76	0.62
	Klippfisk Fm	134-130	1.91	3.22	2.76	0.22
Hydrogen index (mgHC /gTOC)	Kolje Fm	130-113	62	146	90	15
	Klippfisk Fm	134-130	65	198	120	36

In the lower part of the Early Cretaceous Interval, the very good quantity of TOC is mainly dispersed in the western fault block and the RLFC part of the basin. The TOC increases gradually from the shallow-shelf facies (0.7-1.7 wt%) toward the northwestern deep-shelf facies (0.8-1.9 wt%) of the basin with a sharp transition from the HB part to the RLFC part of the basin (1-1.9 wt%) (**Figure 51**).

Regarding the source rock quality and kerogen type, the Early Cretaceous Interval is dominated by low HI (**Table 11**). The mean HI value of the lower interval (134-130 Ma) is 120 ± 36 mgHC/gTOC, while the upper interval (130-113 Ma) has a mean value of HI 90 ± 15 mgHC/gTOC (**Table 11**). In the lower interval, the HI reaches high quality values of ca. 200 mgHC/gTOC at the fault blocks at 134 Ma. In general, the higher values of HI are scattered in the HB part, whereas lower values of HI are confined in the RLFC part of the basin (**Figure 51**).

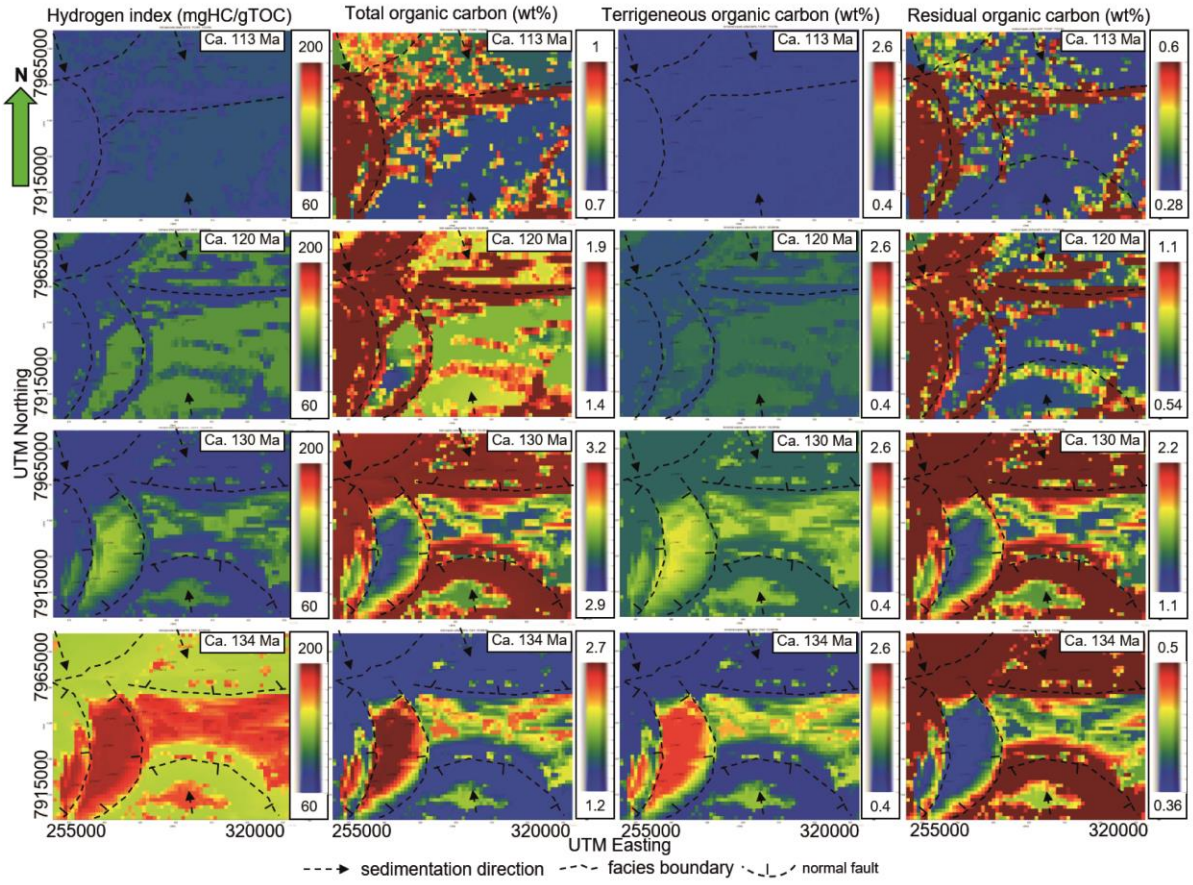

Figure 51. The interpreted 2D maps of the organic facies modelling results of the Early Cretaceous Interval through certain time periods within the interval. Note that not all of the facies use the same scale. Instead, due to the different range of facies values between particular time-slices, auto-scale is sometimes preferred to visualize the lateral distribution.

Within the Early Cretaceous, there is a general decreasing trend of each organic facies from the lower interval (134-130 Ma) to the upper interval (130-113 Ma) (**Figure 51** and **Table 11**). Laterally, the organic facies distribute according to the basin-fill deposition during the Early Cretaceous (**Figure 51**). The TOC and HI disperse following the pattern of C_{terr} and C_{res} distribution in the basin. Commonly, the organic facies are higher in the HB part than in the RLFC part of the basin. However, the HI follows the opposite trend as the higher HI is mainly accumulated in the RLFC part of the basin (**Figure 51**).

4.3.2 Interpretations

Based on the results, the Early Cretaceous (134-113 Ma) is a period of shallow PWD with upper-middle bathyal bathymetry (PWD 20-940 m) (**Figure 50**). The paleo-bathymetry of the beginning of the Early Cretaceous is half-graben geometry as a result of the extent of the rifting events that occurred during the Mid Jurassic-Early Cretaceous (Faleide et al., 2008; Faleide et al., 1993). Toward the end of deposition, the paleo-bathymetry is rather shallow-shelf - deep-

shelf environment, similar to the Early-Mid Triassic Interval, as a result of passive infill of the left-over tectonic accommodation space remaining after the rifting events.

Generally, the Early Cretaceous has a deepening upward trend of water depths (**Figure 52**), in accordance to the global sea-level rise trend during the Early Cretaceous (Haq et al., 1987; Miller et al., 2005). The deepening of the PWD is probably related to the tectonic subsidence during the Mid Jurassic-Early Cretaceous rifting events as well as an effect from the global sea-level. However, some parts of the basin experienced a shallowing upward trend instead, including the southern margin and the northwestern-most deep-shelf area in the basin, as indicated in the PWD map, as well as sedimentary facies map, where the shallow-shelf facies develop into shelf and deep-shelf facies (**Figure 50**). The main factor controlling the shallowing of the water depth is the sedimentation rate variation in the basin, as indicated by the higher sedimentation rates (10-45 cm/ka: 100-450 m/Ma) in these areas (**Figure 50**), outpacing the sea-level rise (ca. 100-150 m/Ma) (Haq et al., 1987). The areas subjected to the shallowing of the water depth are the main sediment accumulation zones in the basin due to the proximity from the sediment sources, in the northwest and southeast parts of the basin. This is also indicated in the SF distribution map in which shaly sand – sand deposits progressively fill northwestwardly in the south and southeastwardly in the north. The sediment sources are interpreted to be the Finnmark Platform to the southeast of the HB and the Loppa High to the northwest (**Figure 1**). Due to the remoteness of the E-W basin axis area from the sediment sources, the sediment accumulation rate are slower in this area. Consequently, the sediment thickness distribution will vary with thicker sediments being deposited in the southern and northern margins, while thinner sediments are deposited in the basin axis.

During the Early Cretaceous, the sedimentation rate is relatively slow-intermediate with some fluctuations especially in the beginning and toward the end of deposition where the sedimentation rates are higher (**Figure 52**). These are in accordance with global sea-level falls (Haq et al., 1987; Miller et al., 2005). Due to the fall of the global sea-level in the Hautarevian (134-130 Ma), the source areas may have experienced erosion and continually supplied sediments to the basin. Additionally, at the end of the Late Jurassic deposition, the western fault blocks and the E-W trending basin axis were relatively shallow. This shallowness, in combination with high nutrient supply and global sea-level drop, may favor the development of a carbonate factory environment along the E-W trending basin axis. Due to the deepening of the water depth throughout the Early Cretaceous, the carbonate is dissolved and deposit clastic sediments, indicated by higher SF (0.4-0.62) accumulation in the basin axis during the

Hauterivian. As the SF is calculated from the gamma ray log, lower value of gamma ray may also correspond to limestone/dolomite. Subsequently, the sedimentation rate is rather stable and progressively filling the basin with thick shaly-sand – sand deposits as a passive infill of the left-over accommodation space remaining from the Late Jurassic-Hauterivian geometry (**Figure 53**). During the Barremian-Aptian (130-113 Ma), the depositional environment is a shallow-shelf – deep shelf rather than a half-graben geometry (**Figure 50**).

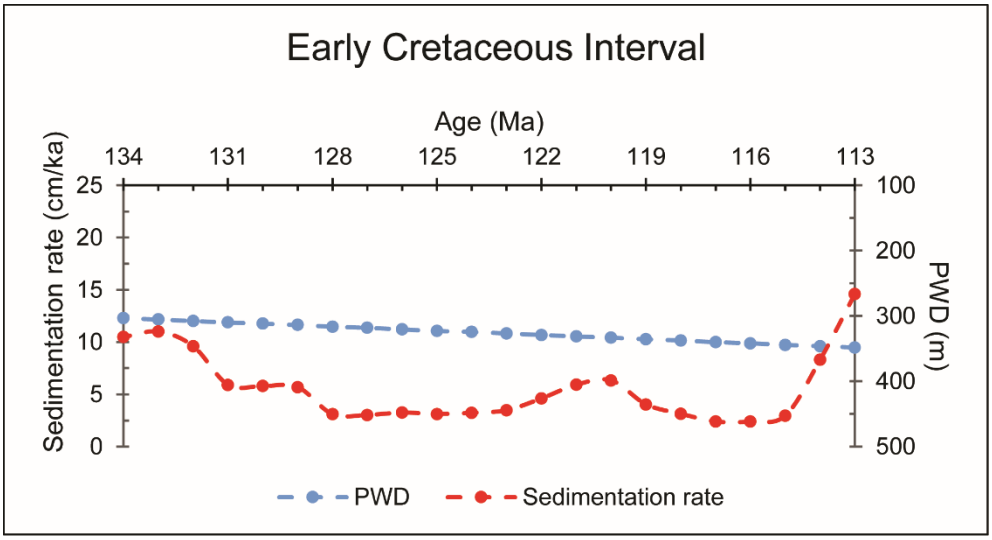

Figure 52. Mean paleo-water depth and mean sedimentation rate change through time during the Early Cretaceous. The sedimentation rate curve shows a fluctuating trend with very slow-intermediate sedimentation rates. The paleo-water depth (PWD) curve shows an overall deepening trend throughout the Early Cretaceous.

Late syn-rift - post-rift stratigraphic pattern

In the Early Cretaceous, there are two different basin-fill processes, as indicated by the distinctive trend of the sedimentary facies, sedimentation rate, and PWD. The Hauterivian (134-130 Ma) is more related to the late syn-rift deposition with half-graben geometry while the Barremian-Aptian (130-113) is related to the sag or post-rift stratigraphic pattern deposition with shallow-shelf – deep-shelf environment. These are reflected by the deposition of the Klippfisk Fm and the Kolje Fm respectively. Additionally, in between these deposits, there is a sharp transition from shale deposition in the lower interval to shaly-sand – sand deposition in the upper interval, marked by the rise of global sea-level and change of sedimentation rate trend toward relatively more stable (**Figure 53**). Thus, the sharp transition is interpreted as the boundary between the Klippfisk Fm and the Kolje Fm and may be considered as an unconformity in the HB. However, the post-rift setting is more dominant in the Early Cretaceous Interval as the thickness is rather variable following the sedimentation rate and basin accommodation space geometry than syn-depositional sedimentation. Different characteristics,

especially in terms of sedimentation and depositional environment between two depositional periods in the Early Cretaceous, may affect how the basin-infill material including organic material accumulate in the basin.

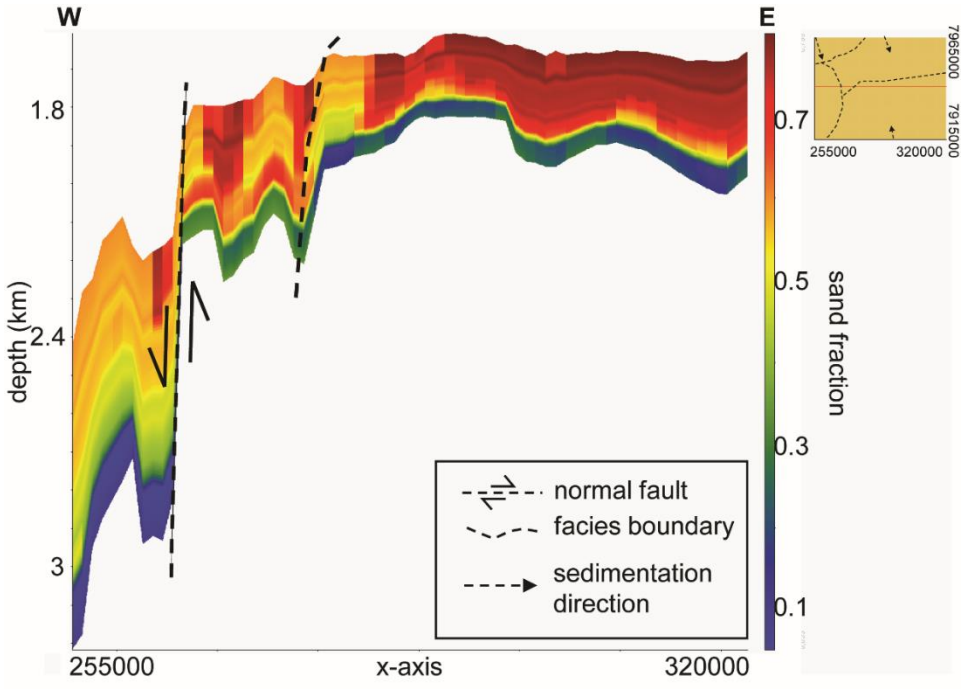

Figure 53. An East-West cross-section of the thick Early Cretaceous shale-sand deposits. The sand fraction (SF) distribution shows a sharp transition from shale to shaly sand-sand deposit upward. Laterally, there is a thickness variation depending on the basin geometry. The west dipping normal fault in the west separates the HB part from the RLFC part of the study area.

Organic matter source types

Based on the results (**Table 11** and **Figure 51**), the organic facies distribute according to the basin-fill deposition during the Early Cretaceous. The Early Cretaceous Interval is more terrestrially-sourced in terms of organic matter (allochthonous), similar to the Early-Mid Triassic Interval with generally poor-very good quantity of the C_{terr} (0.38-2.59 wt%) and the C_{res} (0.28-2.27 wt%) (**Table 11**). Very low primary productivity (0.50-3.97 $gC/m^2/a$) (**Table 11**) and high input of the sand-shale sediments (SF 0.15-0.81) (**Table 10**), with very slow-intermediate sedimentation rate (mean sedimentation rate 5-15 cm/ka) (**Figure 52**), are the main factors causing the more terrestrially-sourced organic matter types in the Early Cretaceous Interval. Most of the MOM fraction has already experienced degradation during the settling in the water column as well as more oxic conditions that cause intense bioturbation on the deposited MOM.

The C_{terr} and C_{res} (**Figure 51**) distribute according to the SF distribution (**Figure 50**), where the C_{terr} is associated with shaly-sand – sand distribution while the C_{res} relates to shale

distribution. Sedimentation distributes the C_{terr} and C_{res} following the northwestward and southeastward sedimentation in the southern and northern parts of the basin respectively (**Figure 51**). An exception for the Klippfisk Fm, as the main accumulations of the C_{terr} is in the E-W trending basin axis instead, surrounded by the C_{res} accumulations (**Figure 51**). The C_{terr} is mainly sourced from the erosion of the basin high formed during the Late Jurassic block faulting, as well as possible supply from the southern source area through shallow western fault blocks. The C_{res} typically accumulates with the shale deposits in the deeper part of the basin, as a result of the degradation from the sediment transport into the basin.

Since the organic matter is mainly sourced from the continental facies, the C_{terr} is mainly derived from land plants, which most likely signify type III kerogen (vitrinite), while the C_{res} is sourced from the degradation of the C_{terr} (type IV kerogen (inertinite)), and thus affects the low HI values (mean HI 90-120 mgHC/gTOC). The poor-fair quantity of the C_{terr} and C_{res} in general may be associated with the preservation conditions during the deposition of the Early Cretaceous Interval.

Preservation conditions

Based on the lateral distribution of the C_{terr} and C_{res} (**Figure 51**), the ratio of C_{res}/C_{terr}, which is approximately equal to the ratio of inertinite/vitrinite, is lower in the E-W trending basin axis than the surrounding area during the deposition of Klippfisk Fm. However, it is lower in the shallow-shelf – shelf area than in the deep-shelf areas during the Barremian-Aptian (Kolje Fm). The areas with higher inertinite/vitrinite ratios of organic matter have higher degree of chemical degradation, reducing the source rock quality potential.

During the Early Cretaceous, the lower interval is dominated by the shale and carbonate deposits while the upper interval consist shaly-sand – sand predominantly and therefore the lower interval has better preservation due to its finer grain sediments. In addition, since the sedimentation rates are slow-intermediate, the sedimentation may oxygenate the depositional environment and cause oxic conditions during the Early Cretaceous generally. This is indicated by good quantity (mean TOC ca. 1.76 wt%) combined with low quality (HI ca. 90 mgHC/gTOC) especially in the Kolje Fm. In the Klippfisk Fm, the TOC and HI are slight higher than the Kolje FM (mean TOC ca. 2.76 wt% and mean HI ca. 120 mgHC/gTOC) as a result of better preservation conditions due to shale-dominated sediments and the left-over of the weakened favourable preservation condition from the Late Jurassic Interval. However since the sedimentation rate is higher during the Hauterivian, the sedimentation dilutes the organic matter and as a result it reduces the organic matter quantity even in the extent of weakened favourable

preservation conditions. Laterally, during the Hauterivian, the preservation conditions increase in the E-W trending, basin axis area, while during the Barremian-Aptian, the preservation conditions increase toward the deep-shelf areas including the RLFC part of the study area. However, since the chemical degradation is higher in the deep-shelf area, it results in more inertinite dominated and thus has less potential for generating hydrocarbons.

Source rock potential and distribution

In general, the Early Cretaceous Interval has poor-fair source rock potential (**Figure 54**). Source rock distribution is according to the generated accommodation space, as well as the basin-fill processes, especially the sedimentation in the basin. Laterally, the main accumulations of high TOC (2-2.7 wt%) and HI (150-200 mgHC/gTOC) during the Hauterivian are in the western fault blocks and E-W trending basin axis. It decreases gradually upward and the main accumulations of higher TOC (1-1.9 wt%) are shifted to the deep-shelf areas, while the higher HI (90-140 mgHC/gTOC) accumulate in the shallow-shelf – shelf areas of the basin during the Barremian-Aptian.

Vertically, the best source rock potential in the Early Cretaceous is within the Klippfisk Fm and lower part of the Kolje Fm (134-126 Ma) (**Figure 55**). This is shown by the accumulation of higher quantity and quality of the source rocks in these intervals as compared to the overlying unit (**Figure 55**). The Klippfisk Fm is more favorable for the source rock potential due to shallower water depth, shale and carbonate dominated, and the extent of presumably weakened favourable preservation conditions from the Late Jurassic Interval. However, since the organic matter quantity and quality and the preservation conditions are generally low, the Early Cretaceous Interval has poor-fair source rock potential in the study area (**Figure 55**). In addition, since the source rock consists of type III kerogen (vitrinite) and type IV kerogen (vitrinite) with poor-fair quantity, it has a potential to both generate low amounts of gas and or generate no hydrocarbons at all.

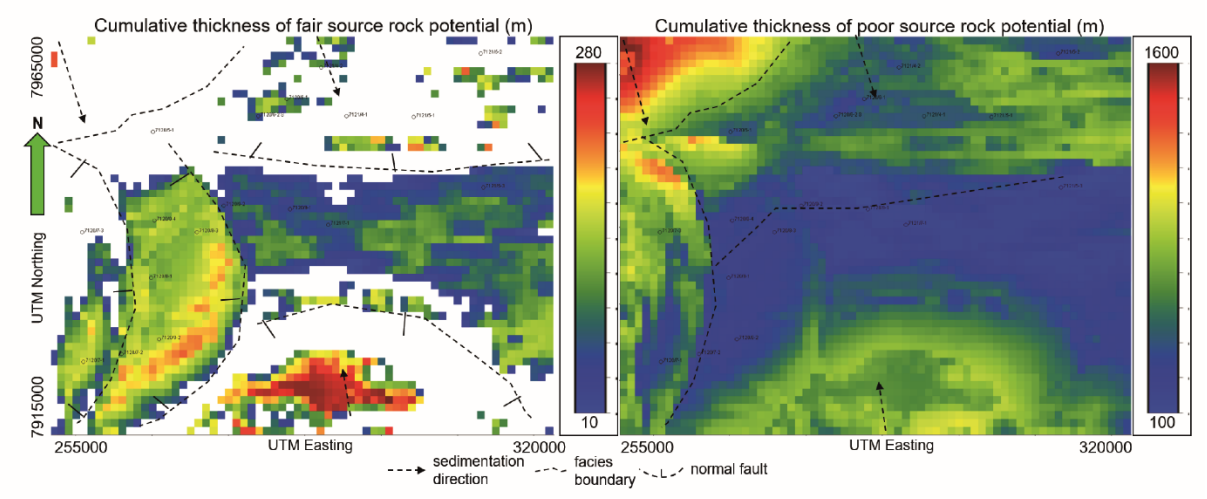

Figure 54. Cumulative thickness of the source rock potential distribution of the Early Cretaceous Interval.

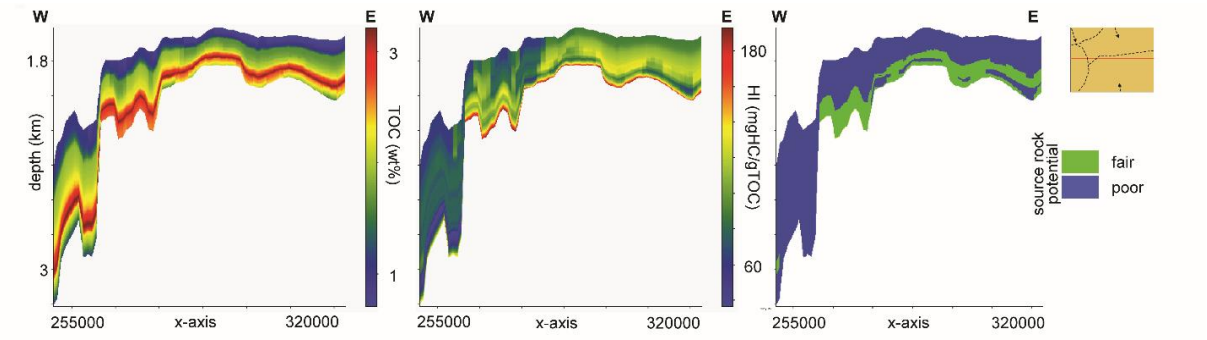

Figure 55. An east-west cross section of the TOC-HI accumulations and the source rock potential for the Early Cretaceous Interval. Vertically, the best source rock potential accumulates in the lower interval, including the Klippfisk Fm and part of the Kolje Fm. Generally, it is dominated by poor-fair source rock potential.

Chapter 5
Discussion

In this study, the main focus is how the paleo-bathymetry and basin-fill processes affect the source rock distribution, thus the validity of the reconstructed paleo-bathymetries and the basin-fill processes are discussed first before discussing further about the factors controlling the source rock distribution in the basin. The models are validated by the sand fraction (SF), total organic carbon (TOC) and hydrogen index (HI) data. In addition, the models and the interpretation are also compared to literature with similar study or area, as well as to the model in a broader scale, to test the validity of the models.

In this chapter, the models are analyzed to discuss further the mismatch between the models and the published data or models. The general observations from the results and interpretation chapter are also considered that may improve the understanding of the study. In addition, the limitations and the benefits of the modelling in general are further discussed as a basis for future studies regarding the topic of source rock distribution.

5.1 Paleo-bathymetry and paleo-water depth changes

The general water-depth changes of the Hammerfest Basin (HB) from the backstripping process are also further evaluated comparing the global sea-level fluctuations (Haq et al., 1987) and tectonic development. The reconstructed paleo-bathymetry models, combined with the geological history of the Barents Sea, are compared with similar studies using different methods, including clinoform heights by Glørstad-Clark et al. (2010) and syn-rift architecture of the North Sea (Ravnås et al., 2000). In addition, the results are compared with present-day analogue basins in the same tectonic setting, including Lake Tanganyika (East-African Rift System), the Red Sea, the Woodlark Basin (Papua New Guinea) and the Black Sea.

The backstripping (uncalibrated) results for each formation top are compared to see the general water depth changes in the HB (**Figure 56**). Note that the applied backstripping procedures in the study are using an Airy isostatic model, thus the isostatic subsidence of the seabed is about 40% of the sea-level change. However, since the wavelength of the water load is very large compared to the lithospheric thickness, the Airy isostatic model is still acceptable (Allen and Allen, 2013).

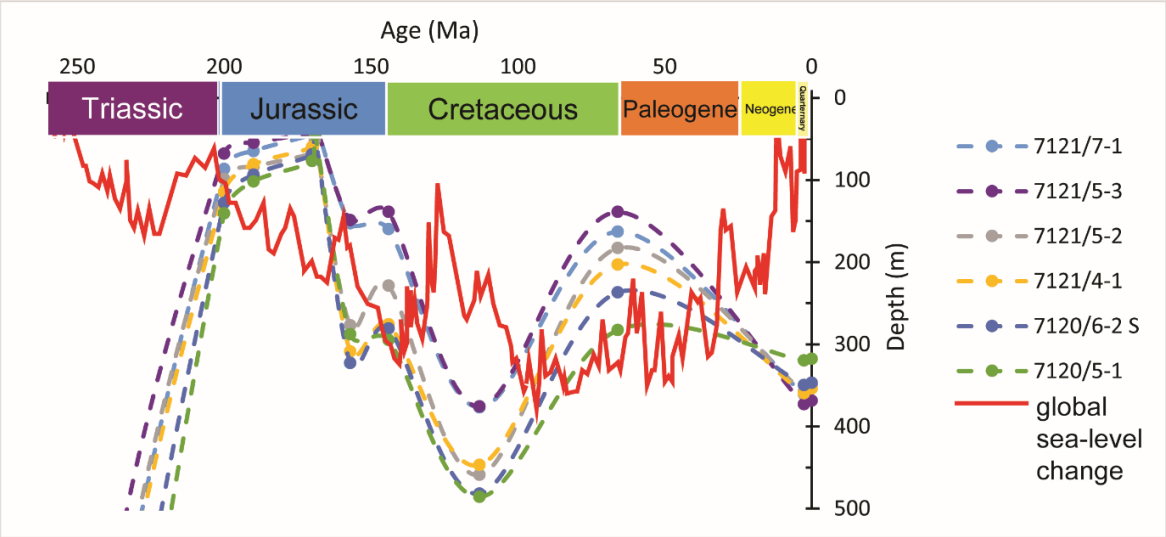

Figure 56. Water depth change from some of the well locations in the study area (the Hammerfest Basin part), based on the backstripped paleo-water depth maps (uncalibrated) from the paleo-bathymetry reconstruction. The water depth changes in the study area are then compared with the global sea-level curve from Haq et al. (1987).

The resulting water depth changes in the HB commonly contradict the global sea-level curve from Haq et al. (1987) (**Figure 56**). The HB is a part of the intracratonic Barents Sea and has been affected by several tectonic phases (Faleide et al., 2008; Gudlaugsson et al., 1998; Larsen et al., 1993; Roberts, 2003; Roberts and Gee, 1985) which will affect the water-depth change. As the backstripped PWD map has already removed the effect of sediment loading toward the total subsidence, the subsidence depicted in the backstripped PWD maps may reflect the tectonic subsidence/uplift during the deposition (Allen and Allen, 2013; Steckler et al., 1999) (**Figure 56**). In addition, eustatic or global sea-level refers to the sea surface position on a global scale relative to a fixed datum including the center of the earth, and thus it is a function of time and is independent of local factors (Zhong et al., 2004). On the other hand, relative sea level (for the study is represented by the water depth changes in the HB) reflects the position of the sea surface to the position of a moving datum and is influenced by local subsidence. The local subsidence includes tectonic subsidence, flexural response of the lithosphere to sediment and water loading, and subsidence caused by compaction of the pre-existing sediment column (Zhong et al., 2004). Consequently, the water depth changes in the HB cannot be compared straightforwardly to the eustatic sea-level. Furthermore, the change of sea-level may be insignificant, especially during the period of active tectonics including rifting and subsidence in the basin.

The Early-Mid Triassic Interval shows a bathyal bathymetry zone within a shelf depositional environment (**Figure 32**). The shallow-shelf facies water depth (400-700 m) is

correlated to the marginal marine facies with water depth up to 500 m by Glørstad-Clark et al. (2010). The shelf and the deep-shelf facies of the study area reflect the shelfal facies with further basinward shoreline trajectory, as compared to the older unit in the interval, by Glørstad-Clark et al. (2010). However, the shelf and the deep-shelf facies, including the RLFC part, show deeper water depths (700-1700 m) in the west than found by Glørstad-Clark et al. (2010). The difference is mainly because of the different methods applied in reconstructing the paleo-water depth (PWD). The study used backstripping method, whereas clinoform height is employed by Glørstad-Clark et al. (2010) to measure the PWD. In addition, the shelf and deep-shelf facies are located away from the shoreline compared to the shallow-shelf facies, and thus may affect the distribution of the clinoform height. Further, the water depth variation of the study area is typical for the rift setting in the rift to drift as the Early-Mid Triassic Interval paleo-bathymetry is a product of regional subsidence during the Permian-Triassic rifting in the Barents Sea (e.g. Doré, 1991; Faleide et al., 2008; Surlyk, 1990).

The Early-Mid Triassic model is, in accordance with the present day rifting to spreading transition basin in the Red Sea (Augustin et al., 2014), where the deepest water depth can reach ca. 2400 m, similar to the maximum water depth reached in the Early-Mid Triassic Interval (ca. 2200 m) (table ch.4) of the study area. Additionally, similar water depth of Lake Tanganyika within the East African Rift system also indicate deep water depth (ca. 1470 m) with steep sides and shelf platform depositional environment (McManus et al., 2015). Generally the Early-Mid Triassic Interval deposition took place in a wide-open marine setting with the shoreline touching the eastern margin of the HB (Bugge et al., 2002; Rasmussen et al., 1993).

The Late Jurassic (**Figure 41**) and the Early Cretaceous (**Figure 49**) Intervals show upper bathyal bathymetries with half-graben basin geometry and shelf facies depositional environment respectively. In the Late Jurassic, the half-graben geometry part has water depths ranging from 50-500 m, whereas the deep-shelf area bathymetry in the northwest reaches 500-900 m depth (**Figure 41**). The depth variation of the half-graben geometry is related to the syn-rift block faulting and rotation in the Barents Sea (Clark et al., 2013; Faleide et al., 2008; Faleide et al., 1993) and the architecture can be compared with the syn-rift architecture in the North Sea (Ravnås et al., 2000). During the syn-rotational phase in the half-graben geometry (Ravnås et al., 2000), the uplifted part of the block can reach a very shallow depth and even emergence, whereas the subsided part of the block can reach a deeper water depth. The reconstructed paleo-bathymetry also indicates deep marine restricted depositional environment in a half-graben geometry as a result of block faulting that form local tectonics barrier in the HB (Brekke et al.,

2001; Clark et al., 2013; Worsley, 2008). This is in accordance with described deep marine restricted depositional environment of the Late Jurassic by Dalland et al. (1988), Georgiev et al. (2017), Henriksen et al. (2011), and Worsley (2008).

Alternatively, the reconstructed paleo-bathymetry for the Early Cretaceous shows a shelf facies depositional environment in an open-marine setting, different from the Late Jurassic Interval. In the HB part, the water depth varies from ca. 280 m in the southeast to ca. 600 m in the northwest gradually, whereas in the RLFC part the water depth has a depth range of 420-770 m (**Figure 49**). The deeper water depth of the RLFC part is a product of the subsidence during the Early Cretaceous (Gabrielsen et al., 1990). The open marine environment in the HB part is in agreement to an open marine environment as described by Dalland et al. (1988), Dallmann (1999), and Brekke et al. (2001).

The Late Jurassic and the Early Cretaceous paleo-bathymetry models are analogues to present day rift basins, including the Red Sea (Augustin et al., 2014; Bonatti, 1985) and the Woodlark Basin, Papua New Guinea (Benes et al., 1994). In both of the present day analogues rift basins, water depths can reach more than ca. 2500 m as the deepest, especially in the spreading zone. On the other hand, the shallowest water depths, which are away from the spreading zone, have a water depth range from 100-1000 m, in a shelf marine environment.

5.2 Rift basin tectonic development and the associated basin-fill processes

The reconstructed paleo-bathymetry models with interpreted faults illustration, combined with the basin-fill models and interpretation as well as the geological history of the Barents Sea are compared to the conceptual rift models by Gawthorpe et al. (2000) to get a better understanding on tectonic development of the HB. The conceptual rift models by Gawthorpe et al. (2000) also depict the associated basin-fill processes, especially the sedimentation pattern, that is a good reference to compare the models of the study area. However, since faults are not included in the modelling during the study, faults array evolution is not taken into account in comparing the models. Instead, more concerns are given to tectonic development, basin geometry and basin-fill processes from the rift conceptual model by Gawthorpe et al. (2000).

The inorganic and organic facies distribution of the Early-Mid Triassic, the Late Jurassic, and the Early Cretaceous Intervals reflect the pattern of the basin-fill processes in a rift basin as a part of rift to drift development in the Barents Sea (Clark et al., 2013; Faleide et al., 2008; Lundin and Dore, 1997). Tectonics, eustasy, and the variation in sedimentation determine the lateral and vertical distribution of the basin-fill. Subsidence, whether induced by tectonics, isostasy, or compaction, is a prerequisite for the preservation of basin-fill (Helland-Hansen et

al., 2016). In a rift basin, the fault array evolution controls the basin-fill (Gawthorpe et al., 2000). The common evolution from initiation stage (the Early-Mid Triassic Interval) to hydrologically isolated basins (the Late Jurassic Interval), evolving into open rifts connected to the ocean (the Early Cretaceous Interval) with shallow to deep-marine sediments (Allen and Allen, 2013; Gawthorpe et al., 2000). The whole tectonic development may not be evident directly in the study area since it is part of the greater intracratonic Barents Sea. Furthermore, faults are not included in the models and are not part of the study focus. However, features of development of each stage (initiation, interaction and linkage, and through-going fault zone), from Gawthorpe et al. (2000) the conceptual rift models may be represented in the study area and captured by the paleo-bathymetries and the basin-fill processes from the three source rock intervals.

The Early-Mid Triassic Interval has a deep water depth with bathyal bathymetry, especially during the beginning of deposition. The deep PWD is formed due to regional subsidence related to the Permian-Early Triassic rifting in the Barents Sea (Doré, 1991; Faleide et al., 2008; Surlyk, 1990). This is correlated with the initiation stage from the rift conceptual models (Gawthorpe et al., 2000). It then develops into the interaction and linkage stage (**Figure 57**) throughout the Triassic extensional faulting (Anell et al., 2013; Doré, 1991; Johansen et al., 1994). The interaction and linkage stage is characterized by higher displacement rates from the major faults with basin depth depending upon the subsidence rate relative to the sediment input. The variation between accommodation space and sediment supply generates contrasting stacking patterns of the sediments (Gawthorpe et al., 2000) (**Figure 57**). These are reflected in the basin-fill processes of the Early-Mid Triassic Intervals by the lower bathyal water depth during the deposition of the Havert-Klappmyss Fms and the Steinkobbe Fm with the RLFC part as the deepest shelf in the study area, followed by shale and sandy-shale deposition with a coarsening upward trend from under-filled phase to the filled phase. The HB part has proximal distance to the source area with shallower water depth and more coarse sediment infill, whereas

the RLFC part is away from the source area, separated by normal faults, and undergoes high subsidence with low sediment input, causing a deep water depth area (**Figure 57**).

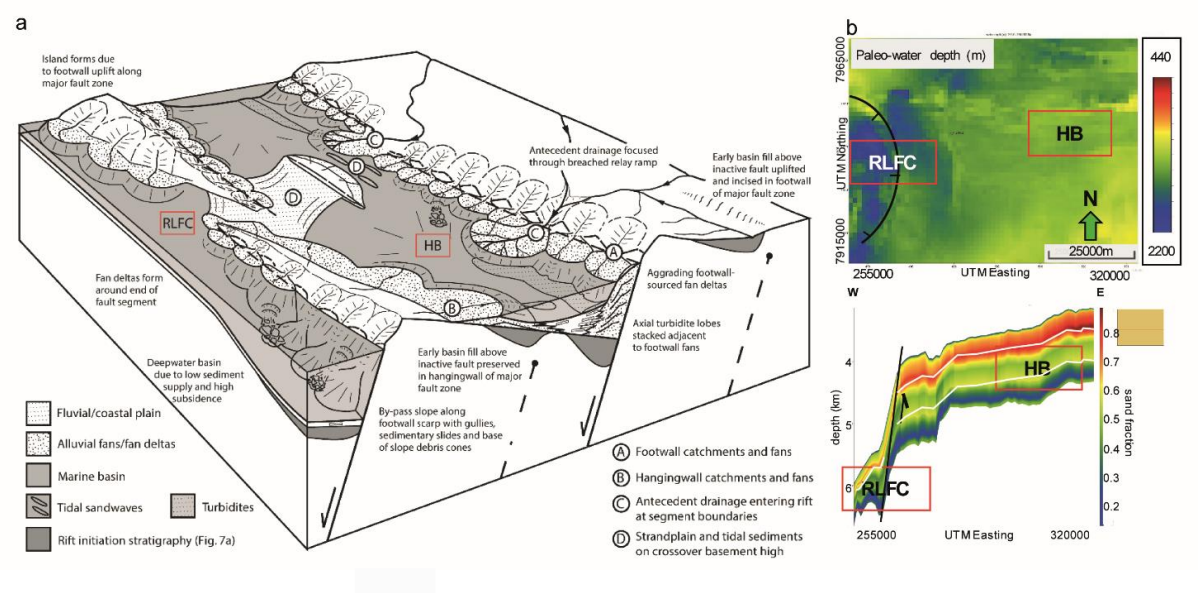

Figure 57. (a) Conceptual rift model by Gawthorpe et al. (2000): interaction and linkage stage during sea level highstand in the normal fault array evolution of marine environments. Red boxes place the study area into the model. Such a scenario might explain the (b) paleo-bathymetry and basin-fill processes models for the Early-Mid Triassic Interval (the Havert-Klappmyss and Steinkobbe Fms). HB: Hammerfest Basin; RLFC: Ringvassøy-Loppa Fault Complex.

During the interaction and linkage stage, progradation may take place, favoured by high sediment supply, low accommodation space at the basin margin, and sea-level lowstand. During the sea level lowstand, basinward shoreline trajectory shifting may also be spatially available (Gawthorpe et al., 2000) (**Figure 58**). This are in accordance with the basin-fill model of the Early-Mid Triassic Interval during the deposition of the Steinkobbe Fm and Kobbe Fm. The development from the filled phase to the over-filled phase is favoured by the maximum progradation period with the development of shallow-shelf facies basinward and the turbidites that deliver basin-fill to the deep-shelf area in the RLFC part. The HB part has more sediment infill with the development of the shallow-shelf facies closer to the basinward shoreline, while the RLFC part remains under-filled with additional input of sediment from turbidite flows (**Figure 58**).

The later stage which is the through-going fault zone stage (**Figure 59**) is well delineated in the Late Jurassic-Early Cretaceous Intervals. The main sedimentation takes place in high accommodation space with low sediment supply in the fault segments, dominated by fine clastic and biogenic hemipelagic sediment with sediment bypass in the fault scarp (Gawthorpe et al., 2000) (**Figure 59**). This characterizes sediment starved marine rift basins at the through-going fault stage (Gawthorpe et al., 2000) during the Late Jurassic-Hauterivian in the HB. Other

examples of these similar characteristics are the Late Jurassic of the North Sea (Rattey and Hayward, 1993) and the Middle Miocene of the Gulf of Suez (Patton et al., 1994).

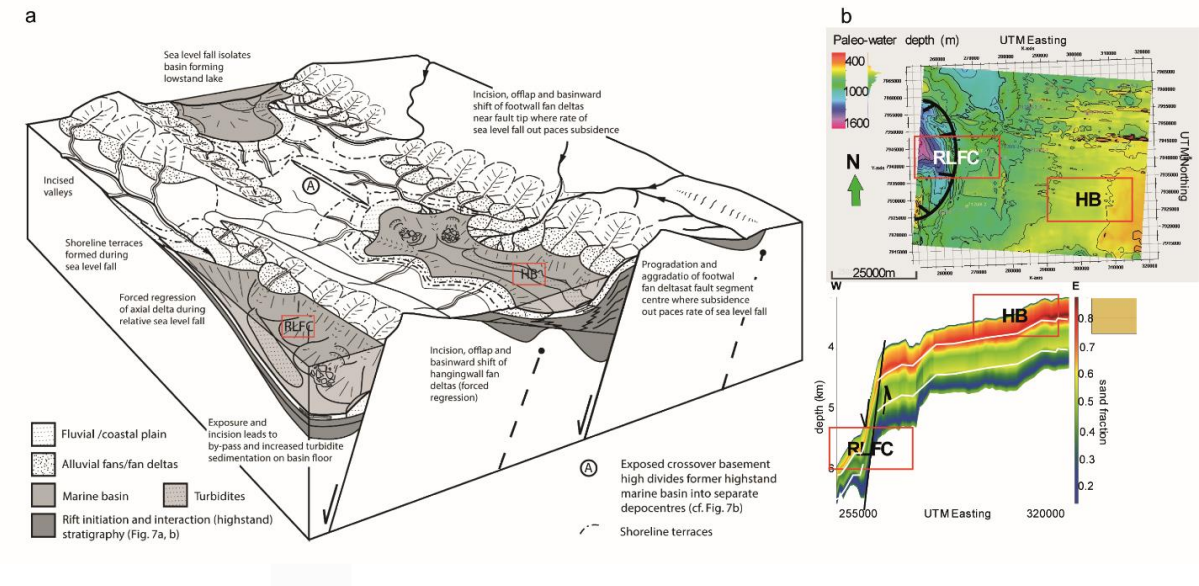

Figure 58. (a) Conceptual rift model by Gawthorpe et al. (2000): interaction and linkage stage during sea level lowstand in the normal fault array evolution of marine environments. Red boxes place the study area into the model. Such a scenario might explain the (b) paleo-bathymetry and basin-fill processes for the Early-Mid Triassic Interval (the Steinkobbe and Kobbe Fms). HB: Hammerfest Basin; RLFC: Ringvassøy-Loppa Fault Complex.

These fault array evolution stages terminate as open rifts connected to the ocean with shallow to deep-marine sediments dominant (Allen and Allen, 2013; Gawthorpe et al., 2000) due to fault inactivity during the post-rift stage. This is in accordance with the deposition of the post-rift sequence during the Barremian-Aptian in the HB. The tectonic development of the three source rock intervals of the study area, from the initiation stage to the open-rifts with the post-rift deposition, indicate depict a development of a rift basin in an active extensional basin setting, from rifting to drifting (Gawthorpe et al., 2000).

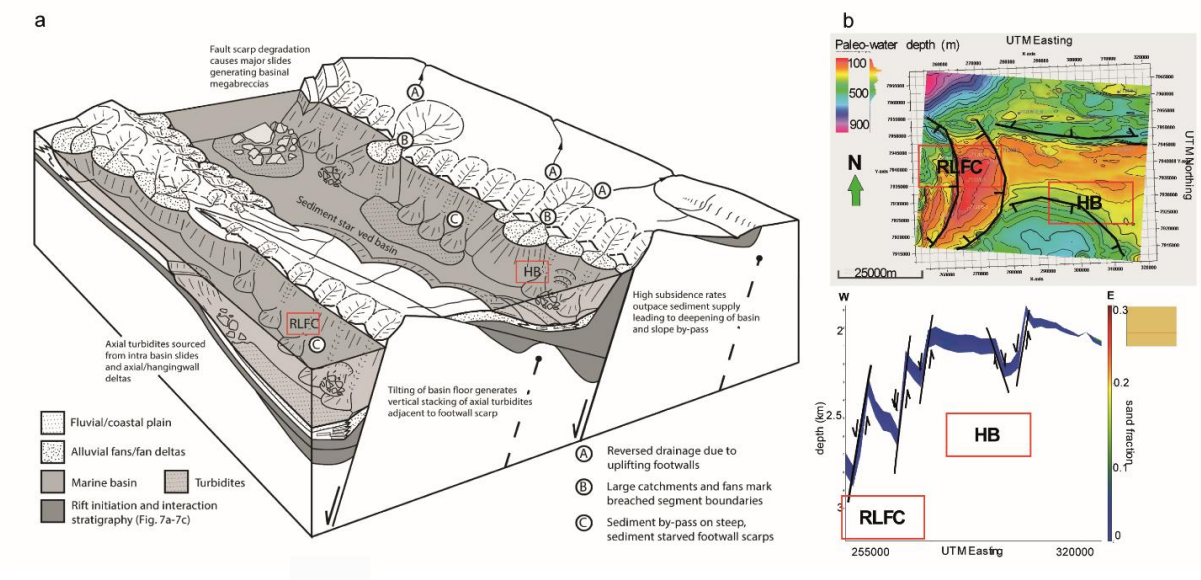

Figure 59. (a) Conceptual rift model by Gawthorpe et al. (2000): through-going fault zone stage in the normal fault array evolution of marine environments. Red boxes place the study area into the model. Such a scenario might explain the (b) paleo-bathymetry and basin-fill processes for the Late Jurassic-Early Cretaceous Intervals. HB: Hammerfest Basin; RLFC: Ringvassøy-Loppa Fault Complex.

Active extensional basins are important because the basin fill processes and the bounding tectonic structures provide high preservation potential of the basin-fill material in the basin and vast economic reserves of hydrocarbons (Gawthorpe et al., 2000). The tectonic development of a typical rift basin in a basin scale of rift to drift setting has an increase of basin-fill preservation potential trend, following the increase of distal subsidence toward the hanging-wall/fault blocks area (Helland-Hansen et al., 2016; Watts, 2012). Further, long-lived tectonically controlled depressions and zones of weaknesses such as fault complexes potentially serve as pathways for sediment to be routed by sediment transport from the source to sink (Helland-Hansen et al., 2016; Sømme et al., 2013; Somme et al., 2009). Thus, in the three source rock interval models, the main accumulation of the basin-fill, including the organic matter, is often in the Ringvassøy-Loppa Fault Complex part of the study area.

In general, the models show good correlation with the rift conceptual model by Gawthorpe et al. (2000). This indicates that the paleo-bathymetry and the basin-fill models could depict the tectonic development of the basin as paleo-bathymetry, basin-fill processes and tectonic development are linked processes and cannot be separated from each other. However, the models may also be further improved by involving faults in the modelling process so that basin-fill processes related to the tectonic/faults and sedimentation can be distinguished to enhance the analysis.

5.3 Factors controlling the source rock distribution

In this sub-chapter, the source rock models, combined with geological history and tectonic development, are compared with the other models published in the literature and the present day analogue models to discuss some factors that control the distribution of source rocks in a basin, specifically in a marine rift basin. In addition, possibility of other preservation conditions is also discussed, comparing with the Late Jurassic model, and linked to the published models and present day analogue models. In the last section, limitations and benefits of the modelling are also elaborated, including other factors which are not incorporated in the modeling but might significantly affect the source rock distribution.

5.3.1 Lessons learned from the OF-Mod modelling

This section mainly discusses the factors controlling the source rock distribution in a marine basin. The discussion is based on the modelling results and interpretations as well as the observations and comparisons with the other models and the present day analogue models. The geological history and the tectonic development of different source rock intervals are also taken into account.

Source rock distribution in basins depends to a large extent on the paleo-bathymetry and the basin-fill processes of the basin during the deposition of the source rock intervals (Katz, 1995; Williams et al., 1985). In marine rift basins, the paleo-bathymetry is controlled largely by the tectonic development of the basin during the deposition as well as sea-level change. In general, when the sedimentation rate is outpaced by the subsidence rate, the deposition of organic-rich source rocks is more favourable (e.g. the Late Jurassic Interval of the study area) as compared to the slowly subsiding platform, outpaced by higher sedimentation rate (e.g. the Early-Mid Triassic Interval of the study area) and post-rift basin (e.g. the Early Cretaceous Interval of the study area) (Katz, 1995; Ulmishek and Klemme, 1983; Watson et al., 1987). Besides, the tectonic development has an important role in shaping the basin accommodation space and architecture that may enhance preservation of the organic matter. For example, the Late Jurassic Interval model has half-graben geometry, developed during block faulting and rotation, and thus increases the preservation potential in the fault blocks area by developing locally restricted depositional environments in the fault blocks, similar to the half-graben rift model of Lake Tanganyika (Rosendahl et al., 1986). In the Lake Tanganyika model, the organic-rich source rock accumulates closer to the border fault and away from the hinge zone (Rosendahl et al., 1986). In the Late Jurassic model, the source rock potential is higher in the fault block areas, where in each of the fault blocks, the accumulation increases toward the faults

(**Figure 47**). Further, rift basins are prone to have water stratification as they typically display low width : depth ratios and are bordered by elevated rift shoulders, thus reducing the mixing especially wind-driven mixing (Katz, 1995).

A narrow-enclosed basin is more favourable for source rock deposition than a wide-open basin. As the narrow-enclosed basin is bounded by a nearby shoreline (e.g. north and south of the basin shoreline in the Late Jurassic model), it has higher potential to receive more nutrient supply from the source areas through sedimentation that may enhance the development of marine organisms in the basin. Further, in a wide-open basin (e.g the Early-Mid Triassic model and the Early Cretaceous model during the Barremian-Aptian) the degradation of the organic matter is more intense due to sediment transport as well as large distance from the shoreline. As a result, source rocks will consist of more degraded organic matter and thus lower the source rock quality as indicated by their higher inertinite than vitrinite organic matter in the TOC and lower HI especially in the areas away from the source (e.g. the Early-Mid Triassic model and the Early Cretaceous model). The present day analogue model for the narrow-enclosed basin enriched with organic-rich source rock, similar to the Late Jurassic model, is the Black Sea (Demaison and Moore, 1980).

Paleo-water depth also plays an important role in the distribution of the organic matter. Deeper water depth reduces the carbon flux in the settling process through the water column (Betzer et al., 1984) and degrades the transported organic matter during the far-distance sediment transport (e.g. the Early-Mid Triassic model). Locations with shallower water depth are prone to have water circulation and winnowing in the uppermost water column that may reduce the quantity of organic matter (e.g. the uppermost Krill Member of the Late Jurassic model). However, the lower parts of the water column in a shallow water part of an enclosed basin (e.g. the Late Jurassic model) or any other restricted depositional environment is prone to have water stratification with anoxic conditions that enhance the preservation of the organic matter due to lower scavenging and bacterial activity during the settling (Allen and Allen, 2013). Settling through the water column or exposure time of the organic matter can also affect the quantity and quality of the organic matter preserved in the source rock (Demaison, 1984; Katz, 1995). Further, marine sourced organic matter shows a slower settling in a water column (Waples, 1983), therefore a shallower water depth is more favourable for the marine sourced organic matter dominated source rock including the Late Jurassic model.

Basin-fill processes contribute significantly toward the distribution of the organic matter in the basin, as reflected by the sedimentation processes as well as the sedimentation rate and

the SF distribution. Commonly, fine grain sediments including shale are more favourable for the organic matter deposition and preservation (e. g. shale of the Kobbe Fm in the Early-Mid Triassic model, the Late Jurassic model, and the Early Cretaceous model) as the low permeability of shale limits the diffusion of oxidants from the water column into the sediments (Allen and Allen, 2013; Scheidegger and Krissek, 1983). In slower sedimentation rate deposition, organic matter is better preserved in the sediments since the dilution of the organic matter is limited (e.g. the Late Jurassic model) (Allen and Allen, 2013). However, higher sedimentation rate may also favour source rock deposition as it reduces the organisms and bacterial activities including bioturbation (Allen and Allen, 2013; Betts and Holland, 1991; Erlenkeuser, 1980), even though the deposited source rock might have lower quantity and quality of organic matter (e.g. the Early-Mid Triassic model) (Allen and Allen, 2013). The sedimentation may also deliver sufficient amount of terrestrially-sourced organic matter that may contribute to the higher quantity of the source rock but with lower quality (e.g. the Kobbe Fm of the Early-Mid Triassic model and the Early Cretaceous model). In addition, the distribution of source rock in the basin is largely dependent on the organic-matter source type as different organic matter-source types have distinct preservation conditions.

Allochthonous

In a terrestrially-sourced organic matter dominated source rocks (e.g. the Early-Mid Triassic and the Early Creatceous Intervals), the main factor controlling the distribution is the sedimentation. The sedimentation mainly delivers land-plant derived organic matter from the continent in the areas that may have contributed toward the type III kerogen dominated source rocks and has lower HI. In the OF-Mod, higher C_{terr} will accumulate in the higher SF sediments, while sediments with lower SF will be dominated by C_{res}, reproducing the degradation process due to sediment transport. As a result, the distribution of the source rock follows the sedimentation patterns, more C_{terr} landward or close to the source of sedimentation area and lower sedimentation rate and more C_{res} basinward. An exception to the progradation sediment, for instance in turbidites, which may deliver C_{terr} further basinward (e.g. the Kobbe Fm in the Early-Mid Triassic model). This is due to the shifting of the shoreline trajectory toward the basin. As a result, more C_{terr} can be transported to the basin with less degradation since sediment is transported faster from source-to-sink.

The vertical stacking pattern in the basin may also affect the distribution of the organic matter with the main principle that shale and finer grained sediments have a better preservation potential. In a rift-sequence stratigraphy (e.g. the Early-Mid Triassic Interval), the best

candidate of source rock will be developed in the shale deposit of the maximum flooding surface top boundary during the retogradation period. In the coarsening upward trend of the maximum progradation sediments, both organic matter quantity and quality are increasing upward due to more basinward shoreline trajectory. However, this point of view might be invalid, due to lack of the geochemical validation data during the modelling the lower interval of the Early-Mid Triassic model.

In general, the allochthonous organic matter source rocks, especially in a wide-open marine rift basin, tend to have poor-fair source rock potential. The lower quantity and quality of the source rocks are mainly caused by the dilution effects due to high sedimentation rate in the basin. Further, high sedimentation rates can oxygenate the basin as it contains more coarser grain sediments that are most likely well oxygenated. As a result, the source rock consists of poorer organic matter quantity and quality. An example of this model is Lake Baikal (Katz, 1995).

Autochthonous

In a marine-sourced organic matter dominated source rocks (e.g. the Late Jurassic Interval), the important factors controlling the distribution are the depositional environment, the PWD, and the basin-fill and preservation conditions. In a marine environment, one of the depositional environments that favours marine source rock deposition is an enclosed basin. Other examples of this depositional environment are the Late Jurassic Kimmeridge Clay and Draupne Formations of the North Sea (Nottvedt et al., 1995) and the Spekk Formation of the Mid-Norway area (Dalland et al., 1988) and the Jurassic Kingak and Aptian-Albian HRZ Formations of the North Slope, Alaska (Allen and Allen 2003). The enclosed basin can be tectonically bordered as a result of tectonic activity including rifting (e.g. the Late Jurassic Interval). The basin geometry causes relatively closer distance to the coastline and thereby potentially supply high nutrient input. This favours the development of marine organisms that may contribute to primary productivity in the water column. An enclosed basin depositional environment, coupled with a narrow basin width (proximal distance to the nutrient supply from the shoreline), shallow water depth, and the sea-level rise boost the primary productivity as the main source of the MOM in the source rocks.

Paleo-water depth is one of the controls on the preservation conditions and thus determines to a large extent the distribution of the autochthonous source rocks in a marine enclosed basin. Shallow water favours the deposition of the organic matter, as deeper water reduces the carbon flux during the settling process from the surface primary productivity to the

sediments. The water column in an enclosed basin is also prone to be stratified and thus potentially develops anoxic conditions, especially in the deeper parts since the water movements takes place in the surface waters. As a result, the TOC will be higher in the lower deposits than near the surface. This is well depicted in the Late Jurassic model vertical TOC and HI variations of the study area and also in anoxic silled marine basin such as the Black Sea (Demaison and Moore 1980).

Another important control is the sedimentation rate. As marine organic matter is prone to be degraded, slower sedimentation rates may favour the preservation of the organic matter, reducing the organic dilution in the sediments. In addition, fine grain sediments including shale are the best candidate for the marine-sourced rock since bacterial activity is limited due to constrained oxygenation. The accumulation of higher TOC and HI follows the main lateral accumulation of the sedimentation in the basin where preservation is good but higher dilution. In a marine rift basin, commonly the main accumulation is in the fault blocks and the hanging wall area with the preservation controlled by the PWD.

5.3.2 Late Jurassic model in association with anoxia possibility

By default, the source rock distribution modelling in OF-Mod applies an oxic environment for the three source rock intervals. Anoxic preservation conditions are not taken into account in the modelling of the source rock. Instead, the main concern of the study is modelling the source rock distribution by linking the paleo-bathymetry and basin-fill processes in the basin and see how these affect the three different source rock intervals in the study area. However, some authors described anoxic conditions during the deposition of the organic rich Late Jurassic source rocks in the Barents Sea (Bugge et al., 2002; Georgiev et al., 2017; Langrock et al., 2003; Leith et al., 1992; Lipinski et al., 2003). Although the richness of the Late Jurassic Interval has been explained by elevated primary productivity and low sedimentation rate in a shale dominated and shallow enclosed basin of the study area models, anoxic preservation conditions may also favour the development of the organic-rich Late Jurassic source rock in the Barents Sea. Nevertheless, marine dominated source-rock formation can more easily be explained as a result of three primary factors which are primary productivity, sedimentation rate and anoxia (Katz, 2005). For instance, elevated primary productivity tends to promote anoxic preservation conditions, whereas anoxic conditions and slow sedimentation rates may develop the regeneration of nutrients and elevated productivity (Katz, 2005). In this sub-chapter, the Late Jurassic model is further discussed, combined with the possibility of having anoxic preservation conditions to get another point of view about the elevated organic

quantity and quality, as well as the possible difference in preservation conditions between the Alge and Krill Members of the Late Jurassic Interval.

The anoxic conditions during the Late Jurassic are more likely developed as a result of limited water circulation (especially in the older sequences) in the study area. This is due to the nature of the narrow-enclosed basin environment, which is bounded by tectonic barriers and formed by block faulting and rifting. In these environments, most of the water movement takes place in the surface layers, while the deeper water columns are prone to stratification (Allen and Allen, 2013). In relevance to the Late Jurassic model, poor source rock potential in the uppermost part of the interval with increasing source rock potential deeper, reaching TOC ca. 13 wt% as the highest, may also be explained through water stratification instead of only due to the decrease of PP and increase of sedimentation rate (**Figure 48**). An analogue present day enclosed basin with water stratification is well recorded in the Black Sea (Allen and Allen, 2013; Demaison and Moore, 1980). In the Black Sea, the shallow water part has lower organic carbon in comparison to the deeper water part. The anoxia is developed below 150 to 250 m with TOC up to 15 wt% (Allen and Allen, 2013; Demaison and Moore, 1980).

The different organic richness between the lower Alge Member and upper Krill Member may also have resulted due to varied preservation conditions. The fact that the TOC is still relatively high even after dilution, indicates extended anoxic bottom water conditions from the Alge Member with weakening trend upward. The weakening upward of anoxia may develop as a result of oxygenation from the increase of sedimentation rate as well as water circulation in the shallower part. These resulted in a decreasing source rock potential trend upward with generally higher source rock potential in the Alge Member than the Krill Member. This is in accordance to the weakening anoxia trend in the Late Jurassic model by Georgiev et al. (2017), using Re-Os analysis. Another model is anoxic bottom water preservation conditions with elevated surface primary productivity (Georgiev et al., 2017; Langrock et al., 2003).

Furthermore, the organic-rich Late Jurassic model is also correlated to the large extent to the world-wide occurence of Upper Jurassic organic-rich rocks. The Upper Jurassic represents one of the largest accumulation of source rocks in Earth's history, contributing around 25% of the world's petroleum reserves (Ulmishek and Klemme, 1983). The widespread oil potential Jurassic source rocks in the world are commonly related to a global anoxic event due to environmental conditions during the Late Jurassic-Early Cretaceous (Dera et al., 2011; Georgiev et al., 2017; Jenkyns, 2010; Jones and Jenkyns, 2001; McArthur et al., 2012; Van Der Meer et al., 2014).

5.3.3 Limitations and benefits of OF-Mod modelling

In general, by linking paleo-bathymetry and basin-fill processes in the OF-Mod modelling, source rock distribution modelling results in geologically understandable source rock potential distributions. Additionally, since the basin-fill (inorganic facies) is a separate process from the organic facies in the modelling, the organic facies modelling is less time consuming. This is because testing the main input for the organic facies modelling can be done for several scenarios without resetting the basin fill model. The modelling can also be done with less well-control (e.g. the Early-Mid Triassic model), which is beneficial at the exploration stage. However, the data quality must be taken into consideration and thus comparing the models with published literature, geological history of the study area, and present day analogue basins is necessary beside the validation process with well data. The modelling also shows that, by linking the paleo-bathymetry and basin-fill processes, the measured TOC and HI data can be further employed to model the source rock distributions with their heterogeneities in the basin, including the organic matter source types and the preservation conditions. This can be employed in the exploration stage, especially as finding the main kitchen area is one of the first steps before further simulation of the basin and petroleum system modelling of a sedimentary basin.

However, simplification and the lateral resolution must also be taken into consideration. For example the modelling has been done with 1 km lateral resolution due to technical limitations with some simplifications. The simplifications are the vertical grid discretization, fuzzy logic approach in determining the facies, and Airy isostasy during the paleo-bathymetry reconstruction. The modelling also excludes the environmental condition variables, even though this might affect the preservation conditions of the organic matter. The environmental conditions, which are important in controlling the source rock distributions, including ocean currents, the paleo-topography and geologic conditions of the source area, the paleo-climate, and the biologic and geochemical conditions both in the source and sink areas.

Chapter 6
Summary and conclusions

The modelling of the three source rock intervals is validated by SF data calculated from the measured gamma-ray log data and measured total organic carbon and hydrogen index data and shows a relatively good match between the modelled and measured data. The Early-Mid Triassic Interval has paleo-bathymetry that varies from upper bathyal to lower bathyal with shelf facies depositional environment in a wide-open marine setting as a result of regional subsidence during the Permian-Triassic rifting in the Barents Sea. Fast-very fast sedimentation rates dominate the basin-fill process and shallowing the paleo-bathymetry through time, outpacing both subsidence and sea-level rise in the HB. The sedimentation fills the basin toward the northwest, and is sourced from the southeast of the basin. The deposition occurred during a progradation period, producing a coarsening upward sequence from shale to sand, developed from under-filled phase to over-filled phase in a rift sequence stratigraphic pattern. The sediments transported terrigenous organic carbon and forms an allochthonous organic matter dominated source rock in the Early-Mid Triassic Interval. The organic matter is distributed following the sedimentation direction and type and basinward shallowing water depth. Due to the poor preservation, the Early-Mid Triassic Interval has a poor source rock potential in general.

The Late Jurassic Interval has neritic-middle bathyal paleo-bathymetry with half-graben geometry and a shallowing trend that resulted from rifting during the Mid Jurassic-Early Cretaceous in the Barents Sea. The sedimentation has very slow to slow rates and thin shaly sediments are deposited. Sedimentation is outpaced by subsidence and forming a sediment-starved basin. During the Late Jurassic, the HB was a narrow-enclosed basin, bordered by shorelines in the north and south. During the deposition, there is an elevated primary productivity, producing a source rock rich in marine organic matter. The source rock is deposited in a favourable basin-fill process with a locally restricted marine environment that enhances the preservation conditions and produces good-very good source rock potential in the basin. There is indication of anoxic preservation conditions that elevate the source rock quantity and quality, due to the nature of the narrow-enclosed basin of the HB, as well as environmental conditions related to the Late Jurassic global anoxic event.

The Early Cretaceous Interval has neritic-bathyal paleo-bathymetry, developing from half-graben geometry to shelf facies depositional environment in an open marine setting. The

paleo-bathymetries are formed during the late syn-rift of the Mid Jurassic-Early Cretaceous rifting and passive infill of the post-rift phase in the Barents Sea respectively. Two different trends for water-depth are found; a deepening trend as a result of subsidence and sea-level rise in the areas with lower sedimentation rates and a shallowing trend in the main sedimentation area. The sediments filled the basin from both south and north with slow-intermediate sedimentation rates. The deposited source rock is dominated by allochthonous organic matter with a distribution that mainly following the sedimentation and SF distribution. In general, the Early Cretaceous Interval has poor preservation conditions and this results in a poor-fair source rock potential in the Hammerfest Basin.

In general, linking the paleo-bathymetry with the basin-fill processes is needed to get better understanding on source rock distribution with their heterogeneity in a basin. The paleo-bathymetry reflects the tectonic development, depositional environment, eustatic sea-level change, and generated accommodation space through subsidence. The basin-fill processes include sedimentation types and rates, proximity of the basin to the shoreline during the deposition, and preservation conditions. Source rock distribution patterns also depend on the organic matter source types.

The three source rock models, combined with the geological history of the Barents Sea, are also compared to the models published from published data. The present-day analogue of the rift to drift basins and anoxic enclosed basins are also employed to discuss the modelling results. In general, despite the limitation of the modelling, the models show similarity with published data and present-day analogue basins with geologically acceptable results. These show that source rock distribution modelling applying the studied methods can be further employed for future exploration with less well control, especially in finding the main kitchen areas in a marine rift basin. The modelling methods can be developed to be more advanced to reduce the limitations. In combination with a full source-to-sink analysis, the model can provide comprehensive geological information that may be useful for the understanding of the source rock distribution.

References

Allen, P.A., Allen, J.R., 2013. Basin Analysis : Principles and Application to Petroleum Play Assessment (3rd Edition). Somerset, NJ, USA: John Wiley & Sons, Somerset.

Anell, I., Braathen, A., Olaussen, S., Osmundsen, P., 2013. Evidence of faulting contradicts a quiescent northern Barents Shelf during the Triassic. First Break 31, 67-76.

Augustin, N., Devey, C.W., van Der Zwan, F.M., Feldens, P., Tominaga, M., Bantan, R.A., Kwasnitschka, T., 2014. The rifting to spreading transition in the Red Sea. Earth and Planetary Science Letters 395, 217-230.

Baldwin, B., 1971. Ways of deciphering compacted sediments. Journal of Sedimentary Research 41.

Benes, V., Scott, S.D., Binns, R.A., 1994. Tectonics of rift propagation into a continental margin: Western Woodlark Basin, Papua New Guinea. Journal of Geophysical Research: Solid Earth 99, 4439-4455.

Berglund, L., Augustson, J., Færseth, R., Gjelberg, J., Ramberg-Moe, H., 1986. The evolution of the Hammerfest Basin. Habitat of Hhydrocarbons on the Norwegian Continental Shelf, 319-338.

Betts, J.N., Holland, H.D., 1991. The oxygen content of ocean bottom waters, the burial efficiency of organic carbon, and the regulation of atmospheric oxygen. Palaeogeography, Palaeoclimatology, Palaeoecology 97, 5-18.

Betzer, P.R., Showers, W.J., Laws, E.A., Winn, C.D., Ditullio, G.R., Kroopnick, P.M., 1984. Primary productivity and particle fluxes on a transect of the equator at 153°W in the Pacific Ocean. Deep Sea Research Part A, Oceanographic Research Papers 31, 1-11.

Bonatti, E., 1985. Punctiform initiation of seafloor spreading in the Red Sea during transition from a continental to an oceanic rift. Nature 316, 33-37.

Brekke, H., Riis, F., 1987. Tectonics and basin evolution of the Norwegian shelf between 62 degrees N and 72 degrees N. Oslo, Norway: Universitetsforlaget, Oslo, pp. 295-321.

Brekke, H., Sjulstad, H.I., Magnus, C., Williams, R.W., 2001. Sedimentary environments offshore Norway — an overview. Norwegian Petroleum Society Special Publications 10, 7-37.

Bugge, T., Elvebakk, G., Fanavoll, S., Mangerud, G., Smelror, M., Weiss, H.M., Gjelberg, J., Kristensen, S.E., Nilsen, K., 2002. Shallow stratigraphic drilling applied in hydrocarbon exploration of the Nordkapp Basin, Barents Sea. Marine and Petroleum Geology 19, 13-37.

Bugge, T., Fanavoll, S., 1995. The Svalis Dome, Barents Sea-a geological playground for shallow stratigraphic drilling. First break 13, 237-251.

Bullimore, S., Larssen, G., Laursen, I., Sollid, K., Ashton, N., Henriksen, S., 2004. Concepts in predicting lithology in prograding systems from high resolution seismic imaging: examples from the Arctic Barents Sea [Unpublished Ph. D. Thesis]. Bergen.

Catuneanu, O., 2006. Principles of Sequence Stratigraphy. Elsevier, Amsterdam ; Oxford.

Clark, S.A., Faleide, J.I., Hauser, J., Ritzmann, O., Mjelde, R., Ebbing, J., Thybo, H., Flüh, E., 2013. Stochastic velocity inversion of seismic reflection/refraction traveltime data for rift structure of the southwest Barents Sea. Tectonophysics 593, 135-150.

Clavier, C., Hoyle, W., Meunier, D., 1971. Quantitative interpretation of thermal neutron decay time logs: part I. Fundamentals and techniques. Journal of Petroleum Technology 23, 743-755.

Dalland, A., Worsley, D., Ofstad, K., 1988. A Lithostrategraphic scheme for the Mesozoic and Cenozoic succession offshore mid- and northern Norway. NPD Bulletin No. 4, Stavanger.

Dallmann, W.K., 1999. Lithostratigraphic lexicon of Svalbard: review and recommendations for nomenclature use: Upper Palaeozoic to Quaternary bedrock. Norsk Polarinstitut.

de Jager, G., Daszinnies, M.C., Emmel, B.U., Lothe, A.E., 2015. High Resolution 3D Process-based Modelling the Distribution of Organic Matter in the Late Jurassic Hekkingen Formation in the Hammerfest Basin (Barents Sea) for Basin Modelling, AAPG Annual Convention & Exhibition 2015, Denver, Colorado.

de Jager, G., Emmel, B., Lothe, A., 2016. Th D09 Fuzzy Logic Modelling of Large Scale Sediment Distribution-An Application for Source Rock Modelling, EAGE Second Conference on Forward Modelling of Sedimentary Systems, Trondheim, Norway.

Demaison, G., 1984. The generative basin concept. Petroleum Geochemistry and Basin Evaluation 35, 1-14.

Demaison, G., Moore, G.T., 1980. Anoxic environments and oil source bed genesis. Organic Geochemistry 2, 9-31.

Dera, G., Brigaud, B., Monna, F., Laffont, R., Pucéat, E., Deconinck, J.-F., Pellenard, P., Joachimski, M.M., Durlet, C., 2011. Climatic ups and downs in a disturbed Jurassic world. Geology 39, 215-218.

Dimakis, P., Braathen, B.I., Faleide, J.I., Elverhøi, A., Gudlaugsson, S.T., 1998. Cenozoic erosion and the preglacial uplift of the Svalbard–Barents Sea region. Tectonophysics 300, 311-327.

Doré, A.G., 1991. The structural foundation and evolution of Mesozoic seaways between Europe and the Arctic. Palaeogeography, Palaeoclimatology, Palaeoecology 87, 441-492.

Emmel, B., de Jager, G., Zieba, K., Kurtev, K., Grøver, A., Lothe, A., Lippard, S.J., Roli, O.A., 2015. A 3D, map based approach to reconstruct and calibrate palaeo-bathymetries – Testing the Cretaceous water depth of the Hammerfest Basin, southwestern Barents Sea. Continental Shelf Research 97, 21-31.

Erlenkeuser, H., 1980. 14C age and vertical mixing of deep-sea sediments. Earth and Planetary Science Letters 47, 319-326.

Espitalie, J., Madec, M., Tissot, B., Mennig, J., Leplat, P., 1977. Source rock characterization method for petroleum exploration, Offshore Technology Conference. Offshore Technology Conference.

Faleide, J.I., Solheim, A., Fiedler, A., Hjelstuen, B.O., Andersen, E.S., Vanneste, K., 1996. Late Cenozoic evolution of the western Barents Sea-Svalbard continental margin. Global and Planetary Change 12, 53-74.

Faleide, J.I., Tsikalas, F., Breivik, A.J., Mjelde, R., Ritzmann, O., Engen, O., Wilson, J., Eldholm, O., Gee, D.G., Ladenberger, A., 2008. Structure and evolution of the continental margin off Norway and the Barents Sea. Ottawa, ON, Canada: International Union of Geological Sciences (IUGS), Ottawa, ON, pp. 82-91.

Faleide, J.I., Vågnes, E., Gudlaugsson, S.T., 1993. Late Mesozoic-Cenozoic evolution of the south-western Barents Sea in a regional rift-shear tectonic setting. Marine and Petroleum Geology 10, 186-214.

Felix, M., 2014. A comparison of equations commonly used to calculate organic carbon content and marine palaeoproductivity from sediment data. Marine Geology 347, 1-11.

Felix, M., Majewska-Bill, M., Mann, U., Rinna, J., 2012. Facies-based sedimentological modelling for use in simulation of organic carbon deposition and burial, AAPG Hedberg Conference, Petroleum Systems: Modelling the past, planning the future, Nice.

Gabrielsen, R.H., 1984. Long-lived fault zones and their influence on the tectonic development of the southwestern Barents Sea. Journal of the Geological Society 141, 651-662.

Gabrielsen, R.H., Faerseth, R.B., 1989. The inner shelf of North Cape, Norway and its implications for the Barents shelf-Finnmark Caledonide boundary; discussion. Norsk Geologisk Tidsskrift 69, 57-62.

Gabrielsen, R.H., Færseth, R.B., Jensen, L.N., Kalheim, J.E., Riis, F., 1990. Structural elements of the Norwegian continental shelf: The Barents Sea region. NPD Bulletin.

Gac, S., Huismans, R.S., Simon, N.S.C., Faleide, J.I., Podladchikov, Y.Y., 2014. Effects of lithosphere buckling on subsidence and hydrocarbon maturation: A case-study from the ultra-deep East Barents Sea basin. Earth and Planetary Science Letters 407, 123-133.

Ganti, V., Lamb, M.P., McElroy, B., 2014. Quantitative bounds on morphodynamics and implications for reading the sedimentary record. Nature communications 5.

Gawthorpe, R.L., Leeder, M.R., Gupta, S., Cowie, P.A., 2000. Tectono-sedimentary evolution of active extensional basins. Basin Research 12, 195-218.

Georgiev, S.V., Stein, H.J., Hannah, J.L., Xu, G., Bingen, B., Weiss, H.M., 2017. Timing, duration, and causes for Late Jurassic–Early Cretaceous anoxia in the Barents Sea. Earth and Planetary Science Letters 461, 151-162.

Glørstad-Clark, E., Birkeland, E.P., Nystuen, J.P., Faleide, J.I., Midtkandal, I., 2011. Triassic platform-margin deltas in the western Barents Sea. Marine and Petroleum Geology 28, 1294-1314.

Glørstad-Clark, E., Faleide, J.I., Lundschien, B.A., Nystuen, J.P., 2010. Triassic seismic sequence stratigraphy and paleogeography of the western Barents Sea area. Marine and Petroleum Geology 27, 1448-1475.

Gradstein, F.M., Kaminski, M.A., Agterberg, F.P., 1999. Biostratigraphy and paleoceanography of the Cretaceous seaway between Norway and Greenland. Earth Science Reviews 46, 27-98.

Gudlaugsson, S.T., Faleide, J.I., Johansen, S.E., Breivik, A.J., 1998. Late Palaeozoic structural development of the South-western Barents Sea. Marine and Petroleum Geology 15, 73-102.

Hadler-Jacobsen, F., Johannessen, E., Ashton, N., Henriksen, S., Johnson, S., Kristensen, J., 2005. Submarine fan morphology and lithology distribution: a predictable function of sediment delivery, gross shelf-to-basin relief, slope gradient and basin topography, Geological Society, London, Petroleum Geology Conference series. Geological Society of London, pp. 1121-1145.

Hallam, A., 1971. Mesozoic Geology and the Opening of the North Atlantic. The Journal of Geology 79, 129-157.

Halland, E.K., Mujezinovic, J., Riis, F., 2013b. CO2 Storage Atlas Barents Sea, NPD report.

Haq, B.U., Hardenbol, J., Vail, P.R., 1987. Chronology of fluctuating sea levels since the Triassic. Science 235.

Hartnett, H.E., Devol, A.H., 2003. Role of a strong oxygen-deficient zone in the preservation and degradation of organic matter: a carbon budget for the continental margins of northwest Mexico and Washington State. Geochimica et Cosmochimica Acta 67, 247-264.

Hartnett, H.E., Keil, R.G., Hedges, J.I., Devon, A.H., 1998. Influence of oxygen exposure time on organic carbon preservation in continental margin sediments. Nature 391, 572.

Hedges, J.I., Keil, R.G., 1995. Sedimentary organic matter preservation: an assessment and speculative synthesis. Marine Chemistry 49, 81-115.

Helland-Hansen, W., Somme, T., Martinsen, O., Lunt, I., Thurmond, J., 2016. Deciphering Earth's Natura; Hourglasses: Perspectives On Source-To-Sink Analysis. J. Sediment. Res. 86, 1008-1033.

Henriksen, E., Ryseth, A., Larssen, G., Heide, T., Rønning, K., Sollid, K., Stoupakova, A., 2011. Tectonostratigraphy of the greater Barents Sea: implications for petroleum systems. Geological Society, London, Memoirs 35, 163-195.

Hjelstuen, B.O., Eldholm, O., Faleide, J.I., 2007. Recurrent Pleistocene mega-failures on the SW Barents Sea margin. Earth and Planetary Science Letters 258, 605-618.

Høy, T., Lundschien, B., 2011. Triassic deltaic sequences in the northern Barents Sea. Geological Society, London, Memoirs 35, 249-260.

Immenhauser, A., 2009. Estimating palaeo-water depth from the physical rock record. Earth Science Reviews 96, 107-139.

Jacobsen, V.W., van Veen, P., 1984. The Triassic offshore Norway north of 62 N, Petroleum Geology of the North European Margin. Springer, pp. 317-327.

Jenkyns, H.C., 2010. Geochemistry of oceanic anoxic events. Geochemistry, Geophysics, Geosystems 11.

Johansen, S., Ostisty, B., Birkeland, Ø., Fedorovsky, Y., Martirosjan, V., Christensen, O.B., Cheredeev, S., Ignatenko, E., Margulis, L., 1993. Hydrocarbon potential in the Barents Sea region: play distribution and potential. Arctic Geology and Petroleum Potential, Norwegian Petroleum Society (NPF), Special Publication 2, 273-320.

Johansen, S.E., Henningsen, T., Rundhovde, E., Sæther, B.M., Fichler, C., Rueslåtten, H.G., 1994. Continuation of the Caledonides north of Norway: seismic reflectors within the basement beneath the southern Barents Sea. Marine and Petroleum Geology 11, 190-201.

Johansen, S.E., Ostisty, B., Birkeland, Ø., Fedorovsky, Y., Martirosjan, V., Christensen, O.B., Cheredeev, S., Ignatenko, E., Margulis, L., 1993. Hydrocarbon potential in the Barents

Sea region: play distribution and potential. Arctic Geology and Petroleum Potential, Norwegian Petroleum Society (NPF), Special Publication 2, 273-320.

Jones, C.E., Jenkyns, H.C., 2001. Seawater strontium isotopes, oceanic anoxic events, and seafloor hydrothermal activity in the Jurassic and Cretaceous. American Journal of Science 301, 112-149.

Justwan, H., Dahl, B., 2005. Quantitative hydrocarbon potential mapping and organofacies study in the Greater Balder Area, Norwegian North Sea. The Geological Society, London.

Katz, B.J., 1995. A survey of rift basin source rocks. Geological Society, London, Special Publications 80, 213-240.

Katz, B.J., 2005. Controlling factors on source rock development—a review of productivity, preservation, and sedimentation rate.

Kjennerud, T., Sylta, O., 2001. Application of quantitative palaeobathymetry in basin modelling, with reference to the northern North Sea. Petroleum Geoscience 7, 331-341.

Klemme, H., Ulmishek, G.F., 1991. Effective petroleum source rocks of the world: stratigraphic distribution and controlling depositional factors (1). AAPG Bulletin 75, 1809-1851.

Laberg, J.S., Vorren, T.O., 1996. The Middle and Late Pleistocence evolution and the Bear Island Trough Mouth Fan. Global and Planetary Change 12, 309-330.

Langrock, U., Stein, R., Lipinski, M., Brumsack, H.-J., 2003. Paleoenvironment and sea-level change in the early Cretaceous Barents Sea—implications from near-shore marine sapropels. Geo-Marine Letters 23, 34-42.

Larsen, R., Fjaeran, T., Skarpnes, O., 1993. Hydrocarbon potential of the Norwegian Barents Sea based on recent well results. Arctic Geology and Petroleum Potential, Norwegian Petroleum Society (NPF), Special Publication 2, 321-331.

Larssen, G.B., Elvebakk, G., Henriksen, L.B., Kristensen, S.-E., Nilsson, I., Samuelsberg, T.J., Svånå, T.A., Stemmerik, L., Worsley, D., 2002. Upper Palaeozoic lithostratigraphy of the southern Norwegian Barents Sea. NPD Bulletin No. 9.

Leith, T., Weiss, H., Mørk, A., Århus, N., Elvebakk, G., Embry, A., Brooks, P., Stewart, K., Pchelina, T., Bro, E., 1992. Mesozoic hydrocarbon sourcerocks of the Arctic region. Arctic Geology and Petroleum Potential, Norw. Petrol. Soc. Spec. Publ 2, 1-25.

Lerch, B., Karlsen, D.A., Matapour, Z., Seland, R., Backer-Owe, K., 2016. Organic Geochemistry of Barents Sea Petroleum: Thermal maturity and alteration and mixing processes in oils and condensates. Journal of Petroleum Geology 39, 125-148.

Lipinski, M., Warning, B., Brumsack, H.-J., 2003. Trace metal signatures of Jurassic/Cretaceous black shales from the Norwegian Shelf and the Barents Sea. Palaeogeography, Palaeoclimatology, Palaeoecology 190, 459-475.

Littke, R., Baker, D., Rullkötter, J., 1997. Deposition of Petroleum Source Rocks, Petroleum and Basin Evolution. Springer, pp. 271-333.

Littke, R., Leythaeuser, D., Rullkötter, J., Baker, D., 1991. Keys to the depositional history of the Posidonia Shale (Toarcian) in the Hils Syncline, northern Germany. Geological Society, London, Special Publications 58, 311-333.

Lundin, E., Dore, A.G., 1997. A tectonic model for the Norwegian passive margin with implications for the NE Atlantic: Early Cretaceous to break-up. J. Geol. Soc. 154, 545-550.

Mann, U., Zweigel, J., 2009. Modelling Source-Rock Distribution and Quality Variations: The Organic Facies Modelling Approach, Analogue and Numerical Modelling of Sedimentary Systems: From Understanding to Prediction. Wiley-Blackwell, pp. 239-274.

Marello, L., Ebbing, J., Gernigon, L., 2013. Basement inhomogeneities and crustal setting in the Barents Sea from a combined 3D gravity and magnetic model. Geophysical Journal International 193, 557-584.

Martins-Neto, M.A., Catuneanu, O., 2010. Rift sequence stratigraphy. Marine and Petroleum Geology 27, 247-253.

McArthur, J., Howarth, R., Shields, G., 2012. Strontium isotope stratigraphy. The Geologic Time Scale 1, 127-144.

McManus, J., Severmann, S., Cohen, A.S., McKay, J.L., Montanye, B.R., Hartwell, A.M., Brucker, R.L.P., Wheatcroft, R., 2015. The sedimentary response to a rapid change in lake level in Lake Tanganyika. Palaeogeography, Palaeoclimatology, Palaeoecology 440, 647-658.

Miller, K., Kominz, M.A., Browning, J., Wright, J.D., Mountain, G., Katz, M.E., Sugarman, P., Cramer, B.S., Christie-Blick, N., Pekar, S., 2005. The Phanerozoic record of global sea-level change, Science, pp. 1293-1298.

Mørk, A., Elvebakk, G., 1999. Lithological description of subcropping Lower and Middle Triasic rocks from the Svalis Dome, Barents Sea. Polar Research 18, 83-104.

Müller, P.J., Suess, E., 1979. Productivity, sedimentation rate, and sedimentary organic matter in the oceans—I. Organic carbon preservation. Deep Sea Research Part A. Oceanographic Research Papers 26, 1347-1362.

Murillo, W.A., Vieth-Hillebrand, A., Horsfield, B., Wilkes, H., 2016. Petroleum source, maturity, alteration and mixing in the southwestern Barents Sea: New insights from geochemical and isotope data. Marine and Petroleum Geology 70, 119-143.

Nagy, J., Kaminski, M.A., Kuhnt, W., Bremer, M.A., 2001. Agglutinated foraminifera from neritic to bathyal facies in the Palaeogene of Spitsbergen and the Barents Sea. Grzybowski Foundation.

Nøttvedt, A., Cecchi, M., Gjelberg, J., Kristensen, S., Lønøy, A., Rasmussen, A., Rasmussen, E., Skott, P., Van Veen, P., 1993. Svalbard-Barents Sea correlation: a short review. Arctic Geology and Petroleum Potential, Norwegian Petroleum Society (NPF), Special Publication 2, 363-375.

Nottvedt, A., Gabrielsen, R., Steel, R., 1995. Tectonostratigraphy and sedimentary architecture of rift basins, with reference to the northern North Sea. Marine and Petroleum Geology 12, 881-901.

O'leary, N., White, N., Tull, S., Bashilov, V., Kuprin, V., Natapov, L., Macdonald, D., 2004. Evolution of the Timan–Pechora and south barents sea basins. Geological Magazine 141, 141-160.

Ohm, S.E., Karlsen, D.A., Austin, T., 2008a. Geochemically driven exploration models in uplifted areas: Examples from the Norwegian Barents Sea. AAPG bulletin 92, 1191-1223.

Ohm, S.E., Karlsen, D.A., Austin, T.J.F., 2008b. Geochemically Driven Exploration Models in Uplifted Areas: Examples from the Norwegian Barents Sea, Atlanta, p. 38.

Pasley, M.A., Riley, G.W., Nummedal, D., 1993. Sequence Stratigraphic Significance of Organic Matter Variations: Example from the Upper Cretaceous Mancos Shale of the San Juan Basin, New Mexico: Chapter 14.

Passey, Q.R., Bohacs, K., Esch, W.L., Klimentidis, R., Sinha, S., 2010. From oil-prone source rock to gas-producing shale reservoir-geologic and petrophysical characterization of unconventional shale gas reservoirs, International oil and gas conference and exhibition in China. Society of Petroleum Engineers.

Paton, D.A., van der Spuy, D., di Primio, R., Horsfield, B., 2008. Tectonically induced adjustment of passive-margin accommodation space; influence on the hydrocarbon potential of the Orange Basin, South Africa. AAPG bulletin 92, 589-609.

Patton, T., Moustafa, A., Nelson, R., Abdine, S., 1994. Tectonic Evolution and Structural Setting of the Suez Rift: Chapter 1: Part I. Type Basin: Gulf of Suez.

Paul, M.A., Barras, B.F., 1998. A geotechnical correction for post-depositional sediment compression: examples from the Forth valley, Scotland. Journal of Quaternary Science 13, 171-176.

Pepper, A.S., Corvi, P.J., 1995. Simple kinetic models of petroleum formation. Part I: oil and gas generation from kerogen. Marine and Petroleum Geology 12, 291-319.

Rasmussen, A., Kristensen, S., Van Veen, P., Stolan, T., Vail, P., Vorren, T., 1993. Use of sequence stratigraphy to define a semi-stratigraphic play in Anisian sequences, southwestern Barents Sea. Arctic Geology and Petroleum Potential, Norwegian Petroleum Society (NPF), Special Publication 2, 439-455.

Rattey, R., Hayward, A., 1993. Sequence stratigraphy of a failed rift system: the Middle Jurassic to Early Cretaceous basin evolution of the Central and Northern North Sea, Geological Society, London, Petroleum Geology Conference series. Geological Society of London, pp. 215-249.

Ravnås, R., Nøttvedt, A., Steel, R., Windelstad, J., 2000. Syn-rift sedimentary architectures in the Northern North Sea. Geological Society, London, Special Publications 167, 133-177.

Reemst, P., Cloetingh, S., Fanavoll, S., 1994. Tectonostratigraphic modelling of Cenozoic uplift and erosion in the south-western Barents Sea. Marine and Petroleum Geology 11, 478-490.

Reynolds, D.J., Steckler, M.S., Coakley, B.J., 1991. The role of the sediment load in sequence stratigraphy: The influence of flexural isostasy and compaction. Journal of Geophysical Research: Solid Earth 96, 6931-6949.

Riis, F., Lundschien, B.A., Høy, T., Mørk, A., Mørk, M.B.E., 2008. Evolution of the Triassic shelf in the northern Barents Sea region. Polar Research 27, 318-338.

Rise, L., Ottesen, D., Berg, K., Lundin, E., 2005. Large-scale development of the mid-Norwegian margin during the last 3 million years. Marine and Petroleum Geology 22, 33-44.

Roberts, D., 2003. The late Riphean Porsangerhalvoyan tectonometamorphic event in the north Norwegian Caledonides; a comment on nomenclature. Norsk Geologisk Tidsskrift 83, 275-277.

Roberts, D., Gee, D.G., 1985. An introduction to the structure of the Scandinavian Caledonides. The Caledonide orogen–Scandinavia and related areas 1, 55-68.

Rodrigues Duran, E., di Primio, R., Anka, Z., Stoddart, D., Horsfield, B., 2013a. 3D-basin modelling of the Hammerfest Basin (southwestern Barents Sea): A quantitative

assessment of petroleum generation, migration and leakage. Marine and Petroleum Geology 45, 281-303.

Rodrigues Duran, E., di Primio, R., Anka, Z., Stoddart, D., Horsfield, B., 2013b. Petroleum system analysis of the Hammerfest Basin (southwestern Barents Sea): Comparison of basin modelling and geochemical data. Organic Geochemistry 63, 105-121.

Ronnevik, H., Beskow, B., Jacobsen, H.P., 1982. Structural and stratigraphic evolution of the Barents Sea.

Rosendahl, B., Reynolds, D., Lorber, P., Burgess, C., McGill, J., Scott, D., Lambiase, J., Derksen, S., 1986. Structural expressions of rifting: lessons from Lake Tanganyika, Africa. Geological Society, London, Special Publications 25, 29-43.

Sadler, P.M., 1981. Sediment Accumulation Rates and the Completeness of Stratigraphic Sections. The Journal of Geology 89, 569-584.

Scheidegger, K.F., Krissek, L.A., 1983. Zooplankton and nekton: natural barriers to the seaward transport of suspended terrigenous particles off Peru, Coastal Upwelling Its Sediment Record. Springer, pp. 303-333.

Schlager, W., 1993. Accommodation and supply—a dual control on stratigraphic sequences. Sedimentary Geology 86, 111-136.

Schlumberger, 1972. Log interpretation : 1 : Principles, V.1-2. ed. Schlumberger Limited, New York.

Schlünz, B., Schneider, R.R., 2000. Transport of terrestrial organic carbon to the oceans by rivers: re-estimating flux- and burial rates. International Journal of Earth Sciences 88, 599-606.

Sclater, J.G., Christie, P.A.F., 1980. Continental stretching: An explanation of the Post-Mid-Cretaceous subsidence of the central North Sea Basin. Journal of Geophysical Research: Solid Earth 85, 3711-3739.

Shepard, F.P., 1954. Nomenclature based on sand-silt-clay ratios. Journal of Sedimentary Petrology 24, 151-158.

Skjold, L.J., van Veen, P., Kristensen, S.-E., Rasmussen, A.R., 1998. Triassic sequence stratigraphy of the southwestern Barents Sea. SEPM Special Publication vol. 60 Mesozoic and Cenozoic Sequence Stratigraphy of European Basins 651-666.

Smelror, M., Mørk, A., Monteil, E., Rutledge, D., Leereveld, H., 1998. The Klippfisk formation - a new lithostratigraphic unit of Lower Cretaceous platform carbonates on the Western Barents Shelf. Polar Research 17, 181-202.

Sømme, T.O., Martinsen, O.J., Lunt, I., 2013. Linking offshore stratigraphy to onshore paleotopography: The Late Jurassic–Paleocene evolution of the south Norwegian margin. Geological Society of America Bulletin 125, 1164-1186.

Somme, T.O., Martinsen, O.J., Thurmond, J.B., 2009. Reconstructing morphological and depositional characteristics in subsurface sedimentary systems: An example from the Maastrichtian–Danian Ormen Lange system, More Basin, Norwegian Sea. AAPG bulletin 93, 1347-1377.

Steckler, M.S., Mountain, G.S., Miller, K.G., Christie-Blick, N., 1999. Reconstruction of Tertiary progradation and clinoform development on the New Jersey passive margin by 2-D backstripping. Marine Geology 154, 399-420.

Steel, R.R.R., 1998. Architecture of marine rift-basin successions. AAPG Bulletin 82, 110-146.

Sund, T., Skarpnes, O., Jensen, L.N., Larsen, R., 1986. Tectonic development and hydrocarbon potential offshore Troms, northern Norway.

Surlyk, F., 1990. Timing, style and sedimentary evolution of Late Palaeozoic-Mesozoic extensional basins of East Greenland. Geological Society, London, Special Publications 55, 107-125.

Szabó, N., Dobróka, M., 2013. Extending the Application of a Shale Volume Estimation Formula Derived from Factor Analysis of Wireline Logging Data. Mathematical Geosciences 45, 837-850.

Ulmishek, G.F., Klemme, H.D., 1983. Depositional controls, distribution, and effectiveness of world's petroleum source rocks. US Government Printing Office.

Van Der Meer, D.G., Zeebe, R.E., van Hinsbergen, D.J., Sluijs, A., Spakman, W., Torsvik, T.H., 2014. Plate tectonic controls on atmospheric CO2 levels since the Triassic. Proceedings of the National Academy of Sciences 111, 4380-4385.

Van Veen, P., Skjold, L., Kristensen, S., Rasmussen, A., Gjelberg, J., Stølan, T., 1993. Triassic sequence stratigraphy in the Barents Sea. Arctic Geology and Petroleum Potential, Norwegian Petroleum Society (NPF), Special Publication 2, 515-538.

Vorren, T.O., Richardsen, G., Knutsen, S.-M., Henriksen, E., 1991. Cenozoic erosion and sedimentation in the western Barents Sea. Marine and Petroleum Geology 8, 317-340.

Walling, D.E., 1983. The sediment delivery problem. Journal of Hydrology 65, 209-237.

Waples, D.W., 1983. Reappraisal of anoxia and organic richness, with emphasis on Cretaceous of North Atlantic. AAPG Bulletin 67, 963-978.

Watson, M., Hayward, A., Parkinson, D., Zhang, Z.M., 1987. Plate tectonic history, basin development and petroleum source rock deposition onshore China. Marine and Petroleum Geology 4, 205-225.

Watts, A.B., 2012. Models for the evolution of passive margins. Department of Earth Sciences, University of Oxford, Parks Road, Oxford OX1 3PR, UK.

Williams, H., Kelley, P., Janks, J., Christensen, R., 1985. The Paleogene rift basin source rocks of Central Sumatra. Indonesian Petroleum Association 14th Annual Convention Proceedings 2, 57-90.

Wood, R., Edrich, S., Hutchison, I., 1989. Influence of North Atlantic Tectonics on the Large-Scale Uplift of the Stappen High and Loppa High, Western Barents Shelf. AAPG Memoir 46, Extensional Tectonics and Stratigraphy of the North Atlantic Margins, 559-566.

Worsley, D., 2008. The post-Caledonian development of Svalbard and the western Barents Sea. Polar Research 27, 298-317.

Zhong, G., Geng, J., Wong, H.K., Ma, Z., Wu, N., 2004. A semi-quantitative method for the reconstruction of eustatic sea level history from seismic profiles and its application to the southern South China Sea. Earth and Planetary Science Letters 223, 443-459.

Ziegler, P.A., 1988. Evolution of the Arctic-North Atlantic and the Western Tethys. American Association of Petroleum Geologists, Tulsa, Okla.